EXCLUSION AREA RADIATION RELEASE DURING THE MIT REACTOR DESIGN BASIS ACCIDENT

by

ROBERT FORREST MULL

B.S., United States Military Academy
(1977)

Submitted to the Department of
Nuclear Engineering
in Partial Fulfillment of the
Requirements of the degree of

MASTER OF SCIENCE IN NUCLEAR ENGINEERING

at the

MASSACHUSETTS INSTITUTE OF TECHNOLOGY

May 1983

Signature of Author: _____
Department of Nuclear Engineering, 6 May 1983

Certified by: _____
David D. Lanning
Thesis Supervisor

Accepted by: _____
Allan F. Henry
Chairman, Nuclear Engineering Departmental Committee

EXCLUSION AREA RADIATION RELEASE DURING THE MIT REACTOR DESIGN BASIS ACCIDENT

by

ROBERT F. MULL

Submitted to the Department of Nuclear Engineering
in Partial Fulfillment of the Requirements of
the Degree of Master of Science in Nuclear Engineering

ABSTRACT

Pending changes in NRC emergency planning requirements have prompted this reevaluation of the maximum radiation dose to an individual located at the exclusion area boundary of the MIT Reactor during the first two hours of its Design Basis Accident. The DBA is postulated to be the melting of four fuel plates in one element, releasing a maximum of 1.5 % of the core fission product inventory to the coolant.

The approach used was to evaluate the major release pathways to the exclusion area boundary. First the reactor system was analyzed to determine the fission product release fractions to the containment. The dose due to leakage from the containment was evaluated using a standard Guassian diffusion model with local meteorological data. Gamma radiation reaching the boundary by simple direct penetration of the containment was determined from standard shielding manual approaches. A compton scattering model was developed and applied to photons scattering from air (skyshine) and from the steel containment roof. Finally, the largest containment penetration, a truck airlock, was checked for radiation streaming.

The resulting total maximum dose is estimated to be 0.595 rads to the whole-body and 0.118 rads to the thyroid. These are well within the regulatory limits for exclusion area releases during an accident. The steel scattering dose was the largest component of the total whole-body dose (63%) and the truck lock penetration dose was found to be negligible. In addition, the behavior of each component of the dose beyond the exclusion area boundary was estimated based on a few prominent gamma energies with the resulting conclusion that the total dose decreases beyond the boundary.

Thesis Supervisor: David D. Lanning
Professor of Nuclear Engineering

ACKNOWLEDGMENT

First and foremost, I would like to thank the United States Army for permitting me to attend MIT and for paying the exorbitant tuition it charges. Next, I would like to thank Professor David Lanning for his overall guidance and assistance in the preparation of this document and Professor Norman Rassmussen for helping to clear up some problem areas. I would also like to thank the Reactor Operations staff for patiently providing me with various plans and data of the reactor facility. Finally, I would like to thank my mother, Betty Mull, and my fellow students and friends for their support and encouragement throughout my studies at MIT.

TABLE OF CONTENTS

TABLE OF CONTENTS (Cont.)

TABLE OF CONTENTS (Cont.)

TABLE OF CONTENTS (Cont.)

LIST OF FIGURES

LIST OF FIGURES (Cont.)

LIST OF TABLES

LIST OF TABLES (Cont.)

CHAPTER I

INTRODUCTION

1.1 Purpose

The purpose of this work is to determine a conservative estimate of the maximum amount of radiation an individual located at the exclusion area boundary of the MIT research reactor (MITR-II) would receive during the first two hours of the reactor's design basis accident (DBA). The motivation for this work stems from new guidelines forthcoming from the Nuclear Regulatory Commission (NRC) requiring the establishment of comprehensive emergency plans for accident response by each research reactor facility. The classification of the emergency and the appropriate actions are related to the size of the radiation release.

The MIT reactor is of particular interest as it is located in the City of Cambridge within the limits of metropolitan Boston. The facility consists of a containment structure, cooling towers and a support building and is located in an industrial area just near the main MIT campus. The surrounding buildings are normally occupied during the work week and the street directly in front of the reactor contains a heavy flow of vehicular and pedestrian traffic. The exclusion area consists of the reactor parking lot, cooling tower area and a portion of the adjacent building NW-12 as shown in Fig. 1.1[1].

1.2 Description of the MITR-II

The present MIT reactor (MITR-II) is a heavy-water reflected, light-

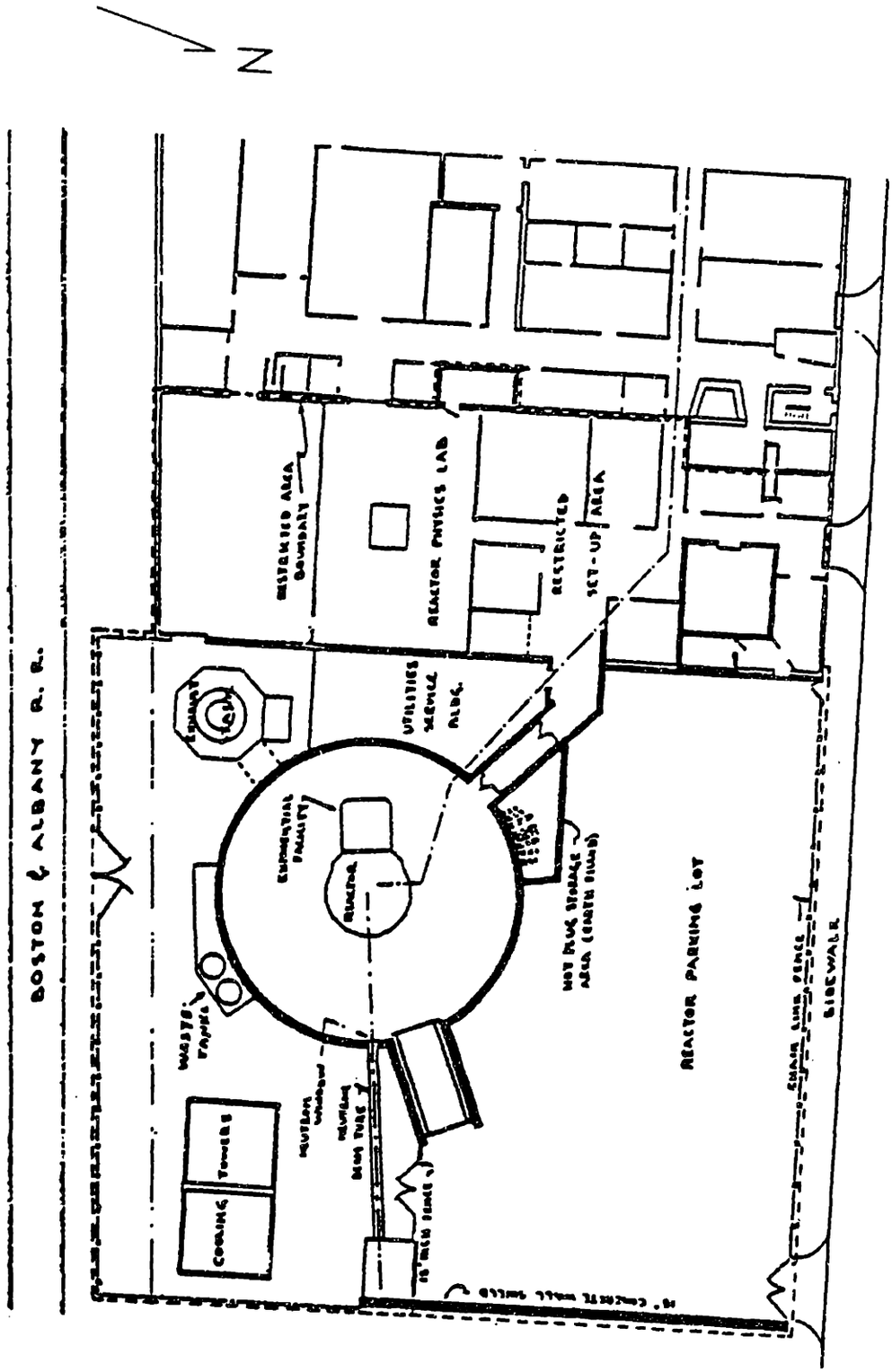

Figure 1.1 Exclusion Area Boundaries [1]

water cooled and moderated 5 megawatt research reactor. It is fueled by 93% enriched U-Al_x flat-plate fuel elements arranged in a compact hexagonal core. This core design maximizes the neutron flux in the D_2O reflector region where numerous experimental beam ports are located. The core is contained within a light- water filled aluminum tank which is in turn contained within the D_2O reflector tank. The H_2O coolant is directed so as to flow down along the tank walls and then upwards through the fuel elements. Heat from the primary systems is transferred by heat exchangers to the secondary system which dissipates it to the atmosphere through the cooling towers.

The reactor is located at the center of a gastight cylindrical steel building equipped with a controlled pressure relief system. Access to the reactor building is through either of two personnel or one truck air-locks. All building penetrations are either sealed permanently or can be sealed rapidly by manual or automatic operation. The building is designed to withstand a maximum overpressure of 2 psi and normally operates at a slight negative pressure. The shell has 0.95 cm (3/8 in) thick steel plates on the sides (5/8 in on the dome) with an outside diameter of 22.6 m (74 ft) and a height of 14.9 m (49 ft). Contained within the circumference of the steel shell is a cylindrical concrete shadow shield 0.61 m (2 ft) thick and 9.6 m (31.5 ft) high. For a more complete description of the reactor and facility the reader is referred to the Reactor Systems Manual [1].

1.3 The MITR-II Design Basis Accident

The design basis accident is the maximum credible accident which could result in the release of radiation from the reactor. For the MITR-II, this is postulated to be a coolant flow blockage in the hottest channel of the center fuel element. This could occur as the result of some foreign material falling into the reactor during refueling. After the pumps are started, the material would be swept from the bottom of the tank up to the fuel element flow entrance. Due to the size of the openings in the adapters at the end of each fuel element any piece of material which could pass through the adapters would not be large enough to restrict the flow in more than five coolant channels of one element, leading to overheating in a maximum of four fuel plates. It is conservatively assumed that the entire active portions of all four plates melt completely, releasing their inventory of fission products to the coolant water.

1.4 Organization of this Thesis

Since the MITR-II is not a closed system, it is possible for fission products in the coolant to emerge directly into the containment atmosphere. The quantity of fission products in the melted fuel and the fraction which is released to, and remains airborne in, the containment will be determined in Chapter 2. The airborne fission products are subject to release from the containment by leakage

through small cracks and gaps and by venting through the pressure relief system. The dose expected from these releases is investigated in Chapter 3. Those fission products which do not escape the containment can still add to the dose at the exclusion area boundary as a source of gamma radiation. This can reach the boundary as simple unattenuated direct radiation through the containment sides or as scattered radiation which reaches the ground through interactions with the air or the steel containment roof. The direct dose is treated in Chapter 4 and the scattered dose in Chapter 5. Finally, the effect of gamma release through containment penetrations is investigated in Chapter 6 by examination of the truck lock.

1.5 Previous Work

The first estimate of an exclusion area radiation release was made in the Final Hazards Summary Report [2] for the original MIT reactor, MITR-I. This was a five megawatt heavy-water moderated and cooled reactor located in the same building and site as the present MITR-II. Although the DBA and fission product release for the MITR-I were different, the report estimated the exposure due to leakage, direct and scattered radiation and formed the basis for all subsequent analyses.

Prior to the reactor being converted to light-water coolant (along with other changes) in 1974 a Safety Analysis Report (SAR) [3]

was published which proposed the present DBA and updated the estimate of exclusion area release. The fission product inventory and release estimates were based heavily on TID-14844 [4] while the dose calculations were very similar to the Final Hazards Report. The SAR introduced an added dose due to the pressure relief system and modified the leakage and steel scattering calculations.

The latest work is a thesis by McCauley [5]. In it, he makes a convincing argument that the present DBA is in fact the maximum credible accident. In addition, he revises the release fractions, particularly those of iodine, based on more recent studies and experience (such as the Three Mile Island accident).

Although the purpose of this thesis is to calculate the same doses via the same release paths, the approach will differ significantly. The fission product source term used in the SAR includes only three elements; Xenon, Krypton, and Iodine. In Chapter 2, the entire spectrum of possible fission products will be considered. The calculations of the leakage dose is revised in accordance with recently published NRC atmospheric diffusion model requirements. The direct dose component more accurately takes into account the shape and size of the volumetric source. By far, the weakest portion of the SAR is that concerning air scattering. Due to its grossly conservative approach, the SAR predicts air scattering to be the dominant component of the total dose. In Chapter 5 a more exact scattering model is developed, which, while still conservative, is

much closer to the actual scattering process. Steel scattering is also updated using the new scattering model. Finally, examination of radiation penetration through the truck lock is a release pathway not previously considered.

CHAPTER 2

DEVELOPMENT OF THE CONTAINMENT SOURCE TERM

2.1 Fission Product Build-up in the Fuel

The fission product inventory in the fuel at the time of the accident is assumed to be equal to the maximum value of equilibrium fission products after an essentially indefinite period of irradiation at 5 MW. This is consistent with the present SAR[3]and NRC guidelines for exclusion area calculations as presented in TID-14844[4].This is a conservative assumption in that the present five days per week operating schedule does not result in saturation of most important fission products, including I^{131}[5]. However, if the operating schedule were to be expanded at some future time, the assumption of equilibrium fission product inventories could become more realistic.

The fission product isotopes of interest have been distilled from a suggested list in Thompson and Beckerley[6]and from those used in the Reactor Safety Study, WASH-1400[7]. The selection has been based on volatility, quantity produced, half-life and degree of biological effectiveness.

Highly volatile isotopes are of primary concern as they can readily escape to the containment atmosphere. Low volatility isotopes (the "solids") are of less importance but still have some finite escape probability. Isotopes which are not produced in sufficient quantity to have a measurable release can be neglected. Isotopes with half-lives of less than ten minutes have been neglected since they would be effectively gone within the first half of the period of the accident. Conversely, some isotopes which were not considered in WASH-1400 due to their short half-lives (with respect to the time scale of that study)

have been included in this study. Finally, only isotopes which contribute significantly to either whole-body or thyroid doses have been considered. The criteria for inclusion was a biological effectiveness within three orders of magnitude of the most effective. The resulting isotopes are listed in Table 2.1.

The saturation activities of the fission products have been determined using two methods, analytical and computational. Each method is discussed in the following sections.

2.1.1 Analytical Calculation

In general, the rate of change in the number of fission product nuclei present in the reactor can be expressed as:

$$\frac{dN_i}{dt} = V_f \overline{\Sigma_f \phi_T} Y_i - \lambda_i N_i \qquad (2.1)$$

Where N_i = Number of nuclei of fission product i.

t = Time (sec)

V_f = Volume of the fuel (cm^3)

Σ_f = Macroscopic fission cross section (cm^{-1})

ϕ_T = Thermal neutron flux (neutrons/cm^2 - sec)

$\overline{\Sigma_f \phi_T}$ = Core-averaged value

Y_i = Fission product yield for isotope i (atoms/fission)

λ_i = Decay constant for isotope i (sec^{-1})

At equilibrium or saturation the change in the number of nuclei is zero and thus

$$0 = V_f \overline{\Sigma_f \phi_T} Y_i - \lambda_i N_i$$

so that,

$$N_s^i = \frac{V_f \overline{\Sigma_f \phi_T} Y_i}{\lambda_i}$$

where N_s^i = Saturation number of nuclei of isotope i.

This can be expressed as a function of reactor power using the fact that one megawatt is produced by 3.2×10^{16} fissions/sec, therefore

$$V_f \overline{\Sigma_f \phi_T} = P(3.2 \times 10^{16}) \text{ fissions/sec.}$$

where, P = Reactor power (MW),

and consequently $N_s^i = \frac{P(3.2 \times 10^{16})\ Y_i}{\lambda_i}$ (2.2)

By definition, the activity (in disintegrations/sec) of N_i is $N_i \lambda_i$. Since one curie equals 3.7×10^{10} dis/sec, the saturation activity, Q_s^i, due to the presence of N_s^i, is

$$Q_s^i = \frac{N_s^i \lambda_i}{3.7 \times 10^{10}} \quad \text{curies}$$

or $$Q_s^i = \frac{P(3.2 \times 10^{16})\ Y_i}{3.7 \times 10^{10}} \quad \text{curies}$$

resulting in $$Q_s^i = 8.65 \times 10^5\ P Y_i \quad \text{curies} \qquad (2.3)$$

Note that the above expression implicitly assumes a constant rate of production of isotope i (i.e. no fuel depletion). It also does not take into account the loss or addition of fission products due to neutron capture. Since most fission products are formed by decay of radioactive parents as well as direct production by fission, the yield value used must be the total yield due to both effects. Values of Y_i and Q_s^i for each isotope are listed in Table 2.1.

TABLE 2.1

Total Core Fission Product Inventory
(in order of decreasing volality) [6,7,8]

Isotope	Half-life $t_{1/2}$	Decay Constant λ_i (sec^{-1})	Total Yield Y_i (%)	Saturation Activity Q_s^i † (Ci)
Kr 85m	4.36h	4.41×10^{-5}	1.5	6.49×10^{4}
87	78m	1.48×10^{-4}	2.7	1.17×10^{5}
88	2.77h	6.95×10^{-5}	3.7	1.60×10^{5}
Xe 131m	12.0d	6.68×10^{-7}	0.03	1.30×10^{3}
133m	2.3d	3.49×10^{-6}	0.16	6.92×10^{3}
133	5.27d	1.52×10^{-6}	6.5	2.81×10^{5}
135m	15.6m	7.40×10^{-4}	1.8	7.78×10^{4}
135	9.13h	2.11×10^{-5}	6.2	4.13×10^{4} ‡
138	17m	6.79×10^{-4}	5.5	2.38×10^{5}
I 131	8.05d	9.96×10^{-7}	2.9	1.25×10^{5}
132	2.4h	8.02×10^{-5}	4.4	1.90×10^{5}
133	20.8h	9.25×10^{-6}	6.5	2.81×10^{5}
134	52.5m	2.20×10^{-5}	7.6	3.29×10^{5}
135	6.68h	2.89×10^{-5}	5.9	2.55×10^{5}
Br 83	2.4h	8.02×10^{-5}	0.48	2.08×10^{4}
84	30m	3.85×10^{-4}	1.1	4.76×10^{4}
Cs 134	2.0y	1.10×10^{-8}	0.0*	2.86×10^{5} ‡
136	13d	6.17×10^{-7}	0.006*	4.14×10^{4} ‡
137	26.6y	8.27×10^{-10}	5.9	2.31×10^{5} ‡
Rb 86	19.5d	4.11×10^{-7}	2.8×10^{-5}*	6.12×10^{4} ‡

† - Analytical value unless otherwise noted

‡ - Computational value

* - Direct yield

TABLE 2.1 (Cont.)

Isotope	Half-life	Decay Constant	Total Yield	Saturation Activity
Te 127m	90d	8.82×10^{-8}	0.056	2.42×10^{3}
127	9.3h	2.07×10^{-5}	0.25	1.08×10^{4}
129m	33d	2.43×10^{-7}	0.34	1.47×10^{4}
129	72m	1.60×10^{-4}	1.0	4.32×10^{4}
131m	30h	6.42×10^{-5}	0.44	1.90×10^{4}
131	24.8m	4.66×10^{-4}	2.9	1.25×10^{5}
132	77h	2.50×10^{-6}	4.4	1.90×10^{5}
133m	63m	1.83×10^{-4}	4.6	1.99×10^{5}
134	44m	2.63×10^{-4}	6.7	2.90×10^{5}
Sr 91	97h	1.99×10^{-5}	5.9	2.55×10^{5}
Ba 140	12.8d	6.27×10^{-7}	6.3	2.72×10^{5}
Ru 103	41d	1.96×10^{-7}	2.9	1.25×10^{5}
105	4.5h	4.28×10^{-5}	0.9	3.89×10^{4}
106	1.0y	2.20×10^{-8}	0.38	1.64×10^{4}
Rh 105	36.5h	5.27×10^{-6}	0.9	3.89×10^{4}
Tc 99m	6.04h	3.19×10^{-5}	~0.6	2.59×10^{4}
Mo 99	67h	2.88×10^{-6}	6.1	2.64×10^{5}
Sb 127	93h	2.07×10^{-6}	0.25	1.08×10^{4}
129	4.6h	4.32×10^{-5}	1.0	4.32×10^{5}
Nd 147	11.3d	7.10×10^{-7}	2.6	1.12×10^{5}
La 140	40.2h	4.79×10^{-6}	6.3	2.72×10^{5}
Ce 141	32d	2.51×10^{-7}	6.0	2.59×10^{5}
143	32h	6.01×10^{-6}	6.2	2.68×10^{5}
144	290d	2.76×10^{-8}	6.1	2.64×10^{5}
Zr 95	63d	1.27×10^{-7}	6.4	2.77×10^{5}
97	17h	1.13×10^{-5}	6.2	2.68×10^{5}
Nb 95	35d	2.29×10^{-7}	6.4	2.77×10^{5}

2.1.2 Computational Calculation

The analytical method cannot be used to determine the Q_s^i values of all isotopes since some isotopes have significant amounts of production and reduction due to neutron capture. Values of Q_s^i for these isotopes (Xe 135, Cs 134, 136,137, and Rb 86) can be estimated using computational results.

A computer code to calculate fission product production has been developed by Blomeke and Todd[8]which solves eleven simultaneous equations of fission product build-up and decay. This model also assumes no depletion of the fuel but includes neutron capture reactions. Values of N_i for various combinations of thermal flux, irradiation time and decay time have been calculated and are available in graphic form. For this study only the saturation values are required. These are expressed as the saturated number of fission product atoms produced per initial atom of U^{235} (N_s^i / N_{25}°) as a function of thermal flux. The core averaged thermal flux value of $\sim 4 \times 10^{13}$ neutrons/cm^2 - sec has been used to enter the graphs. The resulting values of N_s^i/N_{25}° for the neutron-capture influenced isotopes are displayed in Appendix A, Table A.1.

The resulting activity of each isotope can be determined without actual knowledge of N_{25}°. As before, the saturation activity is

$$Q_s^i = \frac{\lambda_i N_s^i}{3.7 \times 10^{10}} \quad \text{curies}$$

or

$$Q_s^i = \frac{(\lambda_i)(N_{25}^\circ)\ (N_s^i/N_{25}^\circ)}{3.7 \times 10^{10}} \quad \text{curies}$$

and given $P(3.2 \times 10^{16}) = V_f\overline{\Sigma_f\phi_T} = N^{\circ}_{25}\sigma^{25}_f\phi_T$

N°_{25} can be expressed as $N^{\circ}_{25} = \dfrac{P(3.2 \times 10^{16})}{\sigma^{25}_f \phi_T}$ atoms (2.5)

where σ^{25}_f = Microscopic fission cross-section for $U^{235} = 580 \times 10^{-24}$ cm^2

Substituting for N°_{25} the saturation activity becomes

$$Q^i_s = \frac{1.49 \times 10^{27}\ \lambda_i P(N^i_s/N^{\circ}_{25})}{\phi_T} \quad \text{curies} \qquad (2.6)$$

(Note: The 2200 m/s value $\sigma^{25}_f = 580 \times 10^{-24}$ cm^2 without temperature adjustment must be used to be consistent with the Blomeke and Todd derivation).

Values of Q^i_s for the above named istotopes obtained using Eq. 2.6 are listed in Table 2.1.

As a check of the analytical method, values of Q^i_s have been calculated using Eq. 2.6 for all the non-neutron-capture influenced isotopes. In all cases the analytical and computational values agree within slight variances due to graphical interpolation. Because of this need to interpolate in the Blomeke and Todd method, the analytical values are considered more accurate and have been used in all subsequent calculations for the non-neutron-capture influenced isotopes.

2.1.3. Fission Product Inventory in the Melted Fuel

In the previous sections the saturated core inventory of fission product activities has been determined. Only a small portion of this

core inventory will be contained in the four fuel plates which are assumed to melt. If the core contains 25 fuel elements and the radial peaking factor is 1.45[3] then the fraction of the total saturated core inventory which is contained in the four center fuel plates, F_s, can be determined to be

$$F_s = \frac{(4 \text{ plates}) \quad (1.45)}{(15 \text{ plates/element}) \ (25 \text{ elements})} = 0.015$$

Therefore, a maximum of 1.5% of each Q_s^i is available for release from the melted fuel.

2.2 Release Fractions

2.2.1 Overview of Release Fractions

While the estimation of fission product accumulation can be done with reasonable accuracy, that of release fractions cannot. Although numerous experiemnts and calculations have been performed for many combinations of temperature, atmosphere, fuel types and the like, there is no universal agreement as to what the exact release fraction for any particular accident will be. At best, only an estimate of the range of possible release fractions can be made. For estimates of potential releases of radioactivity to the public a conservative bias is desired. Although not strictly binding, 10 CFR 100, "Reactor Site Criteria"[9] suggests use of the release fractions in TID-14844, which are: 100% of the noble gases, 50% of the halogens and 1% of the solids released to the containment; and of the iodine released to the containment, 50% remains available for release from the containment [4].

NRC Regulatory Guides 1.3 and 1.4 require the TID source term to be used in evaluating the consequences of BWR and PWR LOCAs, with the exception that the release of solids is neglected [10,11].

Tha above are general estiamtes not particularly suited to the MIT reactor. In the following sections a conservative estimate more applicable to the MITR will be made.

2.2.2 Release from the Fuel

Studies conducted on the melting of uranium metal and uranium-aluminum show that the quantity of fission products released increases with increasing burn-up, percentage of melting, temperature of melting and the total time of melting [6,12,13,14]. The use of the data is limited by the fact that it is given for atmospheres of air, steam-air and helium only. Assuming that the melting of the fuel is accompanied by film boiling, data for steam-air mixtures can be used. Assuming also that the fuel plates have 40% burn-up and are completely melted at a temperature of 1100°C (2012°F) over a period of 60 minutes, the percentage of fission products contained in the four melted plates which are released from the fuel, F_f, can be conservatively estimated as:

100% of the noble gases (Kr,Xe)
100% of the halogens (I, Br)
70% of the Tellurium
30% of the alkali metals (Cs, Rb)
1% of the remaining fission products

These values are comparable to the meldown release component values used in WASH-1400 [15].The differences can be attributed to the difference in fuel (UO_2 clad with zirconium vs. U-Al) and the type of accident

(core meltdown with loss of coolant vs. fuel plate melting with primary envelope intact).

2.2.3 Release From the Primary System

The two methods of fission product depletion in the primary system are deposition on core surfaces (plateout) and absorption in the coolant. Deposition is the dominant mechanism for loss-of-coolant accidents, and retention in the coolant applies to accidents in which the core remains covered. Most research has involved the first case, since these accidents contribute the greatest amount of public risk. The limited work in the second area, as reported in WASH-1400[15]. indicates a 100% release of the noble gases through the coolant, and a range of 100% to 0.1% for the remaining isotopes.

The retention of iodine has received considerable attention in the last two years. Recent studies indicate that iodine may be more likely to be released from the fuel in the form of CsI rather than elemental iodine[6]. The importance of this is that CsI is extremely soluble in water and can be expected to be retained to a high degree. A computer simulation[16]has shown that the release fraction for I_2 through water is 33% while that of CsI is 1%. The formation of CsI is enhanced by a reducing atmosphere, while in the presence of oxygen (including steam, but particularly air) CsI rapidly breaks down resulting in the formation of I_2 or I^-. Although one can argue over which form of iodine will be produced by UO_2, it appears clear that low-oxygen U-Al fuel will produce CsI. McCauley[5]shows that sufficient Cs will exist to combine with all available iodine and that all the CsI will be dissolved in the coolant. In addition, actual measurements of the

activity due to I^{131} in the coolant and that released to the exhaust filters during normal operation indicates a release fraction of 0.01%[5]. Retention of the remaining fission products in water has not been investigated in the literature but can be expected to be low. Retention of all fission products will be primarily a function of their solubility and vapor pressure, which will change depending on the thermodynamic conditions in the reactor vessel. The above dicussion notwithstanding, conservative estimates of the fraction of fission products released from the fuel which escape the primary system, F_p, will be assumed to be:

100% of the noble gases

10% of all other isotopes.

2.2.4 Natural Depletion in Containment

As the MITR has no containment sprays or other engineered safety features to reduce the quantity of fission products in the containment atmosphere, depletion of the radioactive isotopes released to the containment can occur only through natural processes. These include diffusion to and deposition on the walls and equipment, agglomeration and gravitational deposition on the floor, and condensation in the steam. The fraction of fission products released to the containment which remain airborne in the containment atmosphere will be designated as F_c.

The noble gases are not expected to be depleted by any of the above methods resulting in a release fraction of 100%.

Iodine will be assumed to be present in elemental form. Even if released as CsI, the highly oxidizing atmosphere in the containment will cause it to rapidly dissociate. For iodine the primary method of depletion is deposition on the walls through natural convection. For a well-mixed atmosphere the removal rate, λ_R, is determined by

$$\lambda_R = \frac{v_d A_s}{V} \tag{2.7}$$

where, λ_R = Removal rate (sec^{-1})

v_d = Deposition velocity (cm/sec)

A_s = Containment surface area (cm^2)

V = Containment volume (cm^3)

The deposition velocity, v_d, can be analytically determined using Stoke's law[15].In addition, numerous experiments have been conducted to determine v_d (and λ_R) for various atmospheres, concentrations, and surfaces[6,17].These experiments have confirmed that the depletion of iodine follows the exponential relation

$$C(t) = C_o e^{-\lambda_R t} \tag{2.8}$$

where $C(t)$ = Concentration at time t (Ci/cm^3)

C_o = Initial concentration (Ci/cm^3)

λ_R = Removal rate (sec^{-1})

t = Time (sec)

Depletion continues until the equilibrium value of 1% of the original concentration is reached.

The same concept can be extended to particulate fission products. These deplete primarily through agglomeration into 0.05 to 15 micron

diameter particles and subsequent deposition due to gravitational settlement. Particulates can also be entrained with and condensed in the steam, however this is expected to have only a slight effect in the MITR, since the amount of vapor formed will be small.

Assuming that the halogens are present in containment as a gas and all other fission products as solids, the effectiveness of these removal methods for the MITR can be estimated as follows. Although the deposition velocity for iodine is dependent on concentration, temperature and surface type, experiments show that the v_d for painted surfaces range from 1.8×10^{-1} to 3.1×10^{-3} cm/sec[6,17]. From Appendix B, the surface area to volume ratio for the MITR containment is ~ 0.1. Using Eq. 2.7, this sets the limits on the removal rate from 2.13 to 0.037 hr^{-1}, respectively. From Eq. 2.8, this predicts two-hour concentrations of 1.4% and 92.9% of the initial concentration. WASH-1400[15]suggests the use of $\lambda_R = 1.38\ hr^{-1}$ for iodine which results in a two-hour level of 6.3%. Otner data in the literature[6,17] is reported in terms of half-lives, ranging from 10 to 30 minutes. These result in two-hour levels of 1% (reaches equilibrium) and 6.25%. Accepting WASH-1400's value and levelizing over the two-hour period yields an average release fraction of 33.9% McCauley[5] suggests the use of 25%. A value of 30% will be used here. This is expected to be conservative since the natural circulation in the MITR is expected to be greater than that from which the WASH-1400 values were developed, leading to increased deposition.

The release fraction for solids can be obtained in a similar manner using the WASH-1400 particulate value of $\lambda_R = 0.13\ hr^{-1}$ [15]. This predicts a two-hour concentration of 77.1% and a levelized value of 88.0%. Since gravitational deposition is a slow process and the MITR containment is relatively small, there will be less opportunity for particles to agglomerate and settle before reaching the walls and possible leakage points. Therefore a conservative value of 90% will be used.

2.2.5 Summary of Release Fractions

Multiplication of the individual release fractions F_s, F_f, F_p and F_c yields the overall fraction of the total core fission product inventory released to and remaining available in the containment atmosphere. Individual and resulting total release fractions, F_R^i, for the various categories of isotopes are summarized in Table 2.2.

It should be noted that the resulting release fractions are not in keeping with current regulations[9,10,11]. However, the NRC has recognized[16,18]that the TID source term is overly conservative, especially with regards to the release of iodine, and several studies are currently underway which should result in substantiating lower release fractions more in line with this study and the observed releases from historical accidents. Until such results are available, Stone and Webster Engineering Corporation (SWEC)[19]has suggested a conservative interim source term based on preliminary results. Table 2.2 presents this release alongside the present and past MITR release

TABLE 2.2

Release Fractions

	Fraction of the Total Core Fission Product Inventory in the Melted Fuel F_s (%)	Fraction Released from the Melted Fuel F_f (%)	Fraction Released from the Primary System F_p (%)	Fraction which Remains Airborne in the Containment Atmosphere F_c (%)	Overall Release from the Melted Fuel (%)	Overall Fraction of the Total Core Inventory Remaining Airborne in the Containment Atmosphere F_R (%)
			Noble Gases			
This Study	1.5	100	100	100	100	1.5×10^{0}
TID-14884	-	100	100	100	100	-
SAR	1.5	100	50	100	50	7.5×10^{-1}
McCauley	1.5	100	50	100	50	7.5×10^{-1}
SWEC	-	100	100	100	100	-
			Iodine			
This Study †	1.5	100	10	30	3.0	4.5×10^{-2}
TID-14884	-	100	50	50	25	-
SAR	1.5	100	10	50	5.0	7.5×10^{-2}
McCauley	1.5	100	2.0	25	0.5	7.5×10^{-3}
SWEC	-	-	-	-	1.0	-

† - Release fractions for iodine also apply to bromine

TABLE 2.2 (Cont.)

	Fraction of the Total Core Fission Product Inventory in the Melted Fuel F_s (%)	Fraction Released from the Melted Fuel F_f (%)	Fraction Released from the Primary System F_p (%)	Fraction which Remains Airborne in the Containment Atmosphere F_c (%)	Overall Release from the Melted Fuel (%)	Overall Fraction of the Total Core Inventory Remaining Airborne in the Containment Atmosphere F_R (%)
			Tellurium			
This Study	1.5	70	10	90	6.3	9.5×10^{-2}
SWEC	-	-	-	-	1.0	-
			Cesium-Rubidium			
This Study	1.5	30	10	90	2.7	4.1×10^{-2}
SWEC	-	-	-	-	1.0	-
			All Others			
This Study	1.5	1.0	10	90	0.09	1.4×10^{-3}
SWEC	-	-	-	-	1.0	-

fractions. As can be seen, the release fractions proposed in this study are more conservative than the SWEC release, except for the less important "solids". Since the true source term is expected to be smaller than the SWEC value, the release obtained in this thesis is expected to be a definite overestimate of the actual release.

2.2.6 Comparison with Historical Accidents

Four accidents involving melting of U-Al fuel plates in light water due to flow blockage have occurred. The Westinghouse Test Reactor partial melting of one element on 3 April 1960 released 5000 curies of fission products from the fuel, 260 curies of Xe and Kr immediately to the containment, and 800 curies of activity in all [6,20]. The Engineering Test Reactor had 18 plates in 6 elements partially melt on 12 December 1961. This released 42 curies to the coolant, 6 curies of gas and 0.4 of particulate to the stack[6,20,21]. Releases also occurred in the Materials Test Reactor, 13 November 1962, and the Oak Ridge Research Reactor, 1 July 1963, which were not as well instrumented but which in neither case resulted in a hazardous radiological release [6,20].

The other accidents of interest are the SL-1 and TMI-2 accidents. The Stationary Low Power Reactor No. 1 underwent a reactivity excursion on 3 January 1961, which resulted in 20% core melt with up to 10% of the core fission product inventory being ejected outside of the vessel. However, only 0.01% of the fission products escaped the reactor building and only 0.5% of the I^{131} [18,20]. The Three Mile Island Unit 2

experienced a well-documented accident on 28 March 1979 which resulted in extensive core damage. The releases of fission products from the fuel are estimated to be 50-70% of the noble gases, 40% of the iodine and 2-3% of the solids, with releases to the atmosphere of 10% for noble gases, 0.00002% for iodine and a negligible amount of solids. The amount of iodine retained in the primary loop was 500,000 times the amount released to the atmosphere [18].

From the historical data it is believed that the release fractions in Table 2.2 are indeed conservative.

2.3 Comparison With the SAR

Besides the inclusion of additional fission products, this study differs from the SAR in that the release fraction for the noble gases has been doubled and that of iodine decreased slightly. The net effect is an SAR total fission product release strength of 1.70×10^{14} Mev/sec vs. a release strength of 2.60×10^{14} Mev/sec in this study.

CHAPTER 3

ATMOSPHERIC RELEASE

3.1 Release Types and General Assumptions

Atmospheric releases from reactor containments fall into two categories; elevated releases, typically from a stack, and non-elevated releases, usually due to leakage through small cracks or other penetrations in the containment building itself. During normal operation of the MITR-II, the off-gas treatment system results in small releases through the exhaust ventilation and out the stack. During an accident the exhaust plenum to the stack will be automatically closed and sealed. With the containment sealed, a rise in containment pressure is possible depending on the nature of the accident. The design limit of the containment is 2 psi above atmospheric pressure. If the containment pressure should approach this, the pressure can be reduced through use of the pressure relief system. This system consists of a set of valves and filters which will allow controlled venting of containment atmosphere through the stack. If utilized, the filters can be expected to retain about 99% of the iodines and particulate matter but virtually none of the noble gases (annual tests show a retention of 99.8 %) [1].

As the building pressure rises, leakage through small cracks in the joints and seals can occur. The leakage rate is proportional to the amount of over-pressure with the maximum leakage rate set in the technical specifications as 1% of the containment volume per

pound overpressure per day [1].

It is not anticipated that the design basis accident or any other credible accident could produce a rise in containment pressure of 2 psi. For the DBA as postulated, and including a slight decrease in atmospheric pressure, a best guess estimate of the pressure rise is on the order of 0.5 psi. Therefore use of the pressure relief system is not expected for the duration of the accident and no atmospheric releases from the stack will be considered. It is assumed that some release will occur due to building outleakage, and it is this release which will be considered in the following sections.

3.2 Leakage Rate

The estimated leakage rate from containment is dependent on three conservative assumptions. First, the containment pressure is assumed to undergo an instantaneous increase to the design limit of 2 psi over atmospheric. As stated previously, this is not believed likely to occur. Second, the maximum leakage rate of 1% of the building volume per psi over pressure per day will be assumed. Leakage tests of the containment have shown actual leakage rates to be lower [3]. Third, the leakage rate will be assumed to remain constant for the duration of the accident when in actuality it would decrease slightly. With the above conservative assumption, the leakage rate, λ_L, is

$$\lambda_L = .02V/day = 2.3 \times 10^{-7} V/sec$$

where V = Volume of containment.

3.3 Leakage Diffusion Models

The concentration of radioactivity downwind from the containment due to atmospheric dispersion can be estimated from [22]:

$$X/Q = \frac{1}{u\pi\sigma_y\sigma_z + cA_{xs}u} \quad sec/m^3 \tag{3.1}$$

where

X/Q = Relative concentration (sec/m^3)

χ = Concentration of radioactivity (Ci/m^3)

Q = Release rate of fission products (Ci/sec)

u = Wind speed (m/sec)

σ_y = Lateral plume dispersion coefficient (m)

σ_z = Vertical plume dispersion coefficient (m)

c = Shape factor

A_{xs} = Containment cross-sectional area (m^2)

As seen in Eq. 3.1, the initial concentration is reduced by two contributions, atmospheric diffusion and the building wake effect. The diffusion term ($u\pi\sigma_y\sigma_z$) reflects the decrease in concentration due to plume spread horizontally and vertically. This is a function of the wind speed, distance downwind and atmospheric stability conditions. Stability conditions are usually expressed using the Pasquill stability

categories: A(very unstable) through G (very stable). Values of σ_y and σ_z as a function of distance downwind and stability category are available in the literature [7, 10, 11, 22, 23]. The wake effect reflects the tendency for the released particles to quickly expand to fill a volume of air on the order of the containment volume. This effect is a function of windspeed, building cross-sectional area and a shape factor c. The shape factor depends on the particular situation but generally varies from ½ to 2 [22]. As a conservative measure the NRC requires power plant calculations to use the minimum cross-sectional area and a shape factor of ½.

While Eq. 3.1 provides the "exact" value of χ/Q, the NRC states that the reduction of χ/Q due to the wake effect can be no more than a factor of 3, so that the result obtained using Eq. 3.1 must be compared with that from

$$\chi/Q = \frac{1}{3u\pi\sigma_y\sigma_z} \tag{3.2}$$

and the greater value used in consequence evaluations [10,11].

In addition, the NRC recently concluded that the above equations result in concentration estimates that are too high during light wind and stable or neutral atmospheric conditions [23]. For these conditions lateral plume meander is important and can be considered using

$$\chi/Q = \frac{1}{uM\pi\sigma_y\sigma_z} \tag{3.3}$$

where M = Meander correction factor

The correction factor M is a function of windspeed and stability category and is shown in Fig. 3.1.

For the conditions above the greater value of X/Q obtained using Equations 3.1 and 3.2 is compared to that obtained using Eq. 3.3 and the lesser value selected [23].

3.4 Meteorological Data

In order to use the concentration equations the site windspeed and stability category must be known. The best windpspeed data presently available is from the National Weather Service office at Boston's General Logan Airport. The number of recorded instances of windspeeds and their directions for the year 1981 are listed in Appendix A, Table A.2. The frequency of stability conditions can be obtained from historical data in the MITR Final Hazards Report [2]. This information has been summarized in Table A.3.

The appropriate windspeed to use in the calculations was determined for each direction by selecting the lowest windspeed in that direction which was reached or exceeded 99.5% of the total time (for all directions). Resulting directional windspeeds are listed in Table 3.1.

The stability condition determines which graphs will be used to obtain values for σ_y, σ_z and M. The value of X/Q increases as stability increases. Therefore the stability condition which was equal

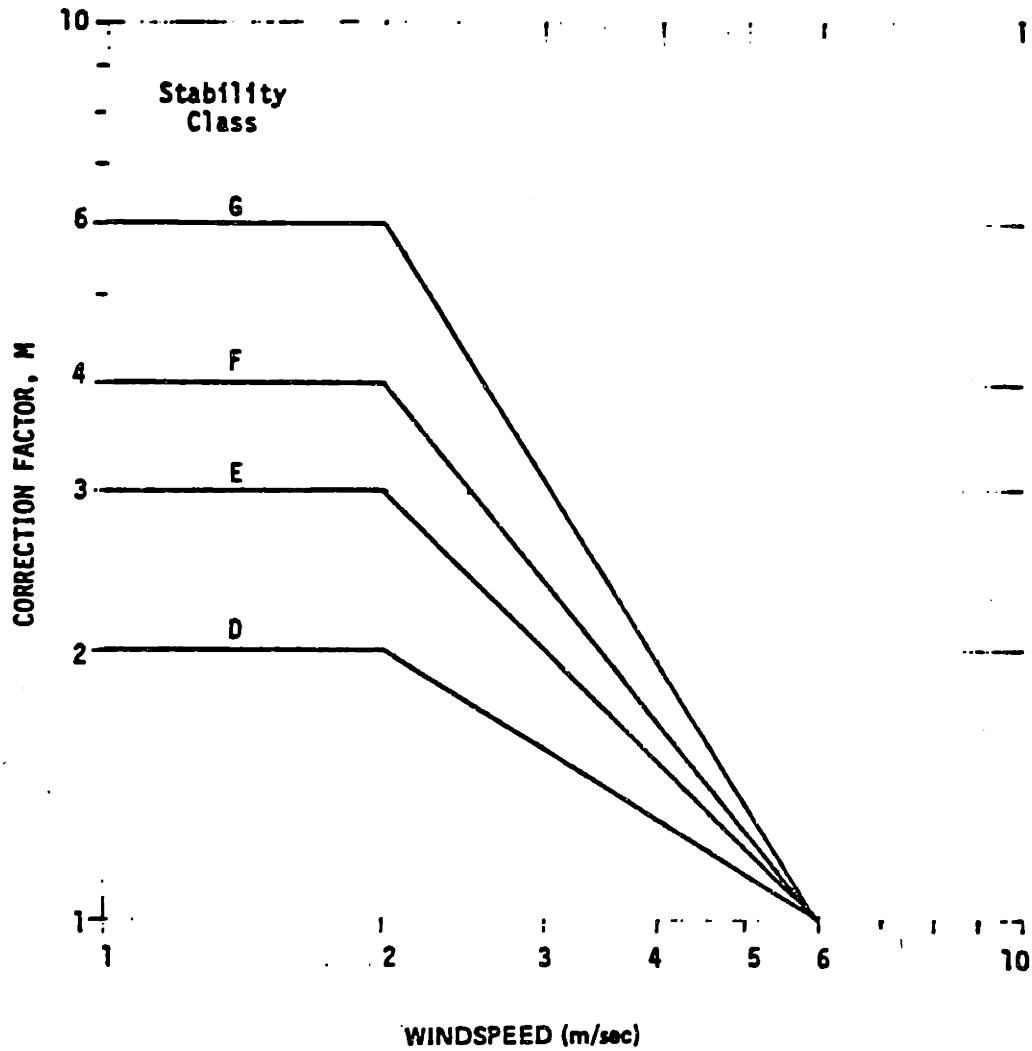

Figure 3.1

Correction Factors for Pasquill-Gifford
σ_y Values by Atmospheric Stability Class [23]

TABLE 3.1

Exclusion Area Parameters

Sector Direction	Sector Windspeed u (m/s)	Minimum Exclusion Area Distance X (m)	Dispersion Coefficients σ_y (m)	σ_z (m)	Relative Concentration χ/Q (sec/m^3) Eq. 3.1	Eq. 3.2
N	1.11	20.6	0.823	0.328	0.00571	0.266
NNE	1.67	22.1	0.883	0.351	0.00379	0.154
NE	1.67	18.7	0.747	0.296	0.00380	0.214
ENE	1.67	18.7	0.747	0.296	0.00380	0.214
E	1.39	17.1	0.683	0.272	0.00457	0.308
ESE	1.39	10.3	0.412	0.164	0.00458	0.846
SE	1.67	8.00	0.320	0.128	0.00381	1.17
SSE	1.67	8.00	0.320	0.128	0.00381	1.17
S	1.11	8.00	0.320	0.128	0.00573	1.76
SSW	1.39	9.53	0.381	0.152	0.00458	0.988
SW	1.39	13.0	0.520	0.207	0.00457	0.532
WSW	1.67	24.0	0.959	0.381	0.00379	0.130
W	1.39	24.0	0.959	0.381	0.00455	0.157
WNW	1.67	24.8	0.991	0.394	0.00378	0.122
NW	1.39	21.0	0.839	0.334	0.00456	0.204
NNW	1.67	20.6	0.823	0.328	0.00379	0.177

to or less stable than the most stable condition for 99% of the time has been selected. This corresponds to Pasquill Category F (moderately stable).

3.5 Exclusion Area Distances

In order to determine σ_y and σ_z the distance from the containment shell to the exclusion area boundary for each wind direction must be known. These values were taken from an MIT Physical Plant site blueprint [24] on which the area around the reactor was divided into 16 sectors of 45° each, centered on each wind direction. The shortest distance between the reactor containment shell and the exclusion area boundary within each sector has been designated the sector distance, X. These values are listed in Table 3.1.

In addition, the cross-sectional area, A_{xs}, of the containment building (from Appendix B) is 314 m^2.

3.6 Dispersion Coefficients

The dispersion coefficients σ_y and σ_z are somewhat difficult to determine as they are given in the literature as a set of curves over the range $10^2 \leq x \leq 10^5$ meters and it is impossible to accurately extrapolate them down to the range of interest, $8 \leq x \leq 25$ meters. One alternative is to use the interpolation formulas for σ_y and σ_z developed by Briggs which fit the Pasquill curves. For type F stability they are [7]:

$$\sigma_y = 0.04\ x\ (1 + 0.0001x)^{-\frac{1}{2}} \quad m \tag{3.4}$$

$$\sigma_z = 0.16\ x\ (1 + 0.0003x)^{-1} \quad m \tag{3.5}$$

where x = Distance downwind (m)

Since these functions were fitted to the Pasquill curves they also are strictly valid only in the range $10^2 \leq x \leq 10^5$ meters. The validity of the Briggs equations for shorter distances was investigated by comparison with the older Sutton diffusion parameters C_y and C_z using the conversion relationships [22]

$$\sigma_y = \frac{C_y}{\sqrt{2}}\ x^{1-\frac{n}{2}} \quad m$$

$$\sigma_z = \frac{C_z}{\sqrt{2}}\ x^{1-\frac{n}{2}} \quad m$$

The difficulty with using Sutton's equations is that there is no agreement among researchers as to the correct values of C_y and C_z for a given atmospheric condition. One representative set of values for type F conditions are [25]:

$C_y = 0.10$

$C_z = 0.06$

$n = 0.5$

Values of σ_y and σ_z calculated with the Briggs equations and the Sutton equations within the range of interest are very close. Therefore the Briggs equations have been used under the assumption

that they yield the most accurate values within the available research in this area and that the error involved is on the same order as that of using airport wind data. Values of σ_y and σ_z evaluated using Eqs. 3.4 and 3.5 are listed in Table 3.1.

3.7 Application of the Diffusion Models

Substitution into Eq. 3.1 shows that the wake effect is dominant over the diffusion term, so much so as to make the dispersion due to diffusion almost negligible. Consequently, Eq. 3.1 will always predict a lower X/Q value than Eqs. 3.2 and 3.3 which are diffusion oriented. Fig. 3.1 gives the value of M in Eq. 3.3 as 4 for all directions. Therefore, for a given set of values for u, σ_y and σ_z Eq. 3.3 will yield a lower value of X/Q than Eq. 3.2 and should be selected to evaluate X/Q for each sector as specified in Sec. 3.3.

While selection of Eq. 3.2 is in line with the NRC guidelines it is possible that this will yield a X/Q (and a subsequent dose) that is too conservative. For example, for the south sector, Eq. 3.2 predicts a X/Q of 1.76 while Eq. 3.1 with the full wake effect yields a X/Q of 0.00573, a factor of $\sim$300 difference. Due to the channeling effect of the adjacent buildings it is expected that the turbulent mixing of the wake effect for the MITR will be more pronounced than that of a containment located in open countryside. Therefore X/Q will be calculated using both the "exact" Eq. 3.1 and the "conservative" Eq. 3.2, with the actual value of X/Q for the MITR expected

to be closer to the "exact" value. Resulting χ/Q values for each sector are shown in Table 3.1.

The largest value of χ/Q is the controlling value for evaluation of the leakage dose received at the boundary. As seen in Table 3.1 this occurs at a distance of 8 meters in the direction south, which is the rear fence of the reactor site. This fence faces a little-used railroad siding which is seldom occupied by the public. The boundary which is most frequently occupied by the public is the fence bordering the Albany Street sidewalk. This sidewalk has an almost constant flow of pedestrians. The largest χ/Q value along this boundary corresponds to the direction north with a distance of 21 meters. Although strictly speaking, the rear fence is the controlling boundary, the front fence dose is of more practical value. Therefore, the dose received at both 8 and 21 meters will be evaluated in this and the following chapters.

3.8 Total Activity Release

The quantity of any fission product initially available for release from containment is equal to the saturated core fission product inventory, Q_s^i, times the overall release fraction for that isotope, F_R^i.

If the fission product inventory is assumed to be distributed uniformly, then the concentration of fission products is equal to

$$\frac{F_R^i Q_s^i}{V}$$

and the rate of release from containment is:

$$\lambda_L F_R^i Q_s^i \quad \text{Ci/sec}$$

where λ_L as given in Sec. 3.2 is the rate of release of the building's contents. The amount of fission products available for release will decrease over the two hour period due to decay and leakage. The resulting time-dependent release rate for fission product i is:

$$Q^i(t) = F_R^i Q_s^i \lambda_L e^{-(\lambda_L + \lambda_i)t} \quad \text{Ci/sec} \tag{3.6}$$

The total quantity released can be determined by integrating the rate equation over the two hour release period, namely:

$$Q_T^i = \int_0^{7200} F_R^i Q_s^i \lambda_L e^{-(\lambda_L + \lambda_i)t} \, dt$$

with the result that

$$Q_T^i = F_R^i Q_s^i \lambda_L \frac{1 - e^{-(\lambda_L + \lambda_i)7200}}{\lambda_L + \lambda_i} \quad \text{Ci} \tag{3.7}$$

Values of Q_T^i for each isotope are listed in Appendix A, Table A.4.

3.9 Adjustments to the Release Term Outside of Containment

As the fission products leave the containment, they begin to disperse in accordance with the χ/Q value. Further reductions are possible due to decay enroute, ground deposition, and precipitation scavenging.

3.9.1 Radiological Decay

The correction factor for decay enroute is [22]:

$$\frac{Q_T(x)}{Q_T} = \exp\left(-\lambda_i \frac{x}{u}\right)$$

However, the longest time $(\frac{x}{u})$ it takes for particles to reach any point on the exclusion area boundary is:

$$\frac{x}{u} = \frac{20.6 \text{ m}}{1.11 \text{ m/s}} = 18.5 \text{ sec}$$

This is much shorter than the shortest fission product half-life (15.6 min., Xe 135 m) so decay enroute will be neglected.

3.9.2 Ground Deposition

Gravitational deposition on the ground can be expected to occur for particles of more than 10 microns in size. The vertical movement of smaller particles is determined primarily by the bulk motion of the air [22]. Even for the larger particles, calculations for type F conditions with a windspeed of 1 m/s and a release height of 10 meters do not show any deposition until 300 meters downwind [22]. Therefore ground deposition can also be neglected.

3.9.3 Precipitation Scavenging

If the release occurs during rain or snow, precipitation scavenging would occur and wash out some particles to the ground.

Since this would lower the inhalation (thyroid) dose, it will be conservatively assumed that no precipitation occurs for the duration of the release.

3.10 Beta Dose

The dose rate in air from an infinite uniform cloud of beta radiation is determined from [22]:

$$\beta^{D'} = \frac{(1.6 \times 10^{-6} \text{ergs/Mev})(3.7 \times 10^{10} \text{dis/Ci-s})\bar{E}_\beta \chi}{(1293 \text{ g/m}^3)(100 \text{ erg/g-rad})}$$

which reduces to:

$$\beta^{D'} = 0.457 \, \bar{E}_\beta \chi \quad \text{rads/sec} \tag{3.8}$$

where,

$\beta^{D'}$ = Beta dose rate (rads/sec)

$\bar{E}_\beta$ = Average beta energy per disintegration (Mev/dis)

χ = Concentration of beta-emitting isotope (Ci/m^3)

1293 = Density of air at S.T.P. (g/m^3)

The surface body dose rate is about one-half of this [22] or

$$\beta^{D'} = 0.23\bar{E}_\beta \chi \quad \text{rads/sec} \tag{3.9}$$

Since the concentration is time-dependent the total beta dose is:

$$\beta^{D} = 0.23\bar{E}_\beta \int_0^{7200} \chi(t)dt \quad \text{rads} \tag{3.10}$$

The concentration integral can be related to the previously determined X/Q values by the relationship

$$X(t) = (X/Q)Q(t) \qquad Ci/m^3$$

which when integrated yields

$$\int_0^{7200} X(t)dt = (X/Q)\int_0^{7200} Q(t)dt$$

Since, by definition $Q_T = \int_0^{7200} Q(t)dt$, the above can be expressed as

$$\int_0^{7200} X(t)dt = (X/Q)Q_T \qquad \frac{Ci\text{-}sec}{m^3}$$

The total beta dose received due to isotope i is therefore

$$_{\beta}D_i = 0.23\ \bar{E}_{\beta}^{i} Q_T^i\ (X/Q)\ \text{rads} \tag{3.11}$$

The value of $\bar{E}_{\beta}^{i}$ is equal to one-third the value of the maximum beta energy for isotope i [22]. Values of $\bar{E}_{\beta}^{i}$ for each isotope are listed in Table A.4.

These conservative calculations indicate an estimated total beta exposure due to all isotopes of 3.42 rads at 8 meters and 0.517 rads at 21 meters using the "conservative" X/Q values and 1.11×10^{-2} rads at both boundaries using the "exact" X/Q.

3.11 Gamma Doses

Developed in the same manner as the beta equation, the dose rate due to gamma radiation in air is [22]:

$$ {}_{\gamma}D' = 0.507\ \bar{E}\ \chi \quad \text{rads/sec} \tag{3.12} $$

Unlike the short-range beta radiation, the gamma radiation received is reduced by one-half due to the presence of the ground [22], resulting in

$$ {}_{\gamma}D' = 0.25\ \bar{E}_{\gamma}\chi \quad \text{rads/sec} \tag{3.13} $$

The total gamma dose due to isotope i is

$$ {}_{\gamma}D_i = 0.25\ \bar{E}^i_{\gamma}\ Q^i_T\ (\chi/Q) \quad \text{rads} \tag{3.14} $$

The value of $\bar{E}^i_{\gamma}$ in the above equation is determined by weighting the gamma energy spectrum for each isotope i.

A second, more accurate, method to determine the gamma dose is to use WASH-1400 [7] computer generated dose conversion factors, C^i_{γ}, in the equation

$$ {}_{\gamma}D_i = C^i_{\gamma}Q^i_T(\chi/Q) \quad \text{rads} \tag{3.15} $$

where C^i_{γ} = Photon dose-conversion factor for immersion in air contaminated with isotope i (rads per $\frac{\text{Ci-sec}}{\text{m}^3}$)

Values of C^i_{γ} are not listed for all isotopes of interest. Where unavailable, values of $\bar{E}^i_{\gamma}$ were determined and ${}_{\gamma}D_i$ calculated using Eq. 3.14. Values of $\bar{E}^i_{\gamma}$ and C^i_{γ} are listed in Table A.4. These conservative calculations indicate an estimated total gamma dose due to all isotopes of 4.70 rads at 8 meters and 0.710 rads at 21 meters using the "conservative" χ/Q values and 1.55×10^{-2} rads at both distances using the "exact" χ/Q.

3.12 Thyroid Dose

In general, the radiation dose received by the thyroid is dependent on the amount of isotope inhaled, the fraction which is transported to the thyroid, the energy absorbed by the thyroid per disintegration, and the rate at which the isotope is removed by decay and biological elimination.

WASH-1400 [7] also provides inhalation dose coversion factors for various parts of the body, including the thyroid, which can be used in:

$$ {}_{T}D_{i} = B_{r} C_{T}^{i} Q_{T}^{i} \ (X/Q) \quad \text{rads} \tag{3.16} $$

where ${}_{T}D_{i}$ = Dose to thyroid from isotope i (rads)

B_{r} = Breathing rate (m^3/sec)

C_{T}^{i} = Thyroid inhalation conversion factor for isotope i (rads per Ci inhaled)

Isotopes of interest which are not inlcuded in WASH-1400 were checked against ICRP Report #2 [26] and found to have no contribution to the thyroid dose.

The standard breathing rate for calculations of internal dose is 3.47×10^{-4} m^3/sec [23].

Values of C_{T}^{i} for each isotope are listed in Table A.4. The resulting "conservative" estimate of the total thyroid dose due to all isotopes is 36.3 rads at 8 meters and 5.49 rads at 21 meters and the "exact" estimate is 1.18×10^{-1} rads at either boundary.

3.13 Summary and Comparison with the SAR

As shown in Table 3.2, the conservative NRC atmospheric release calculations performed in this chapter indicate that the estimated maximum total potential for personnel exposure due to containment leakage over a two hour period following the accident is 8.12 rads whole-body and 36.3 rads to the thyroid at the back fence (a distance of 8 meters) and 1.23 rads whole-body and 5.49 rads thyroid at the Albany St. fence (a distance of 21 meters). The more realistic estimate based on the full wake effect predicts a maximum dose of 2.66×10^{-2} rads whole-body and 1.18×10^{-1} rads to the thyroid at either boundary. A comparison of the "conservative" and "exact" whole-body and thyroid doses over the entire range of exclusion area distances is shown in Figs. 3.2 and 3.3. Note that the wake effect is so large as to make the difference in "exact" doses due to distance negligible.

The SAR gives the two-hour leakage dose to the thyroid (whole-body was not evaluated) as 2.8×10^{-1} rads [3]. This was determined using

$$\chi/Q = \frac{1}{cA_{xs}u} \qquad \text{sec/m}^3$$

in which full credit is taken for the wake effect and diffusion is neglected. In addition, the SAR assumed simultaneous full operation of the pressure relief system and a windspeed of 1 m/s.

TABLE 3.2

Leakage Dose Summary

Component of Dose	Dose (Rads) "Exact" Eq. 3.1	"Conservative" Eq. 3.2 8m	"Conservative" Eq. 3.2 21m
Whole-body:			
Beta	0.0111	3.42	0.517
Gamma	0.0155	4.70	0.710
Total	0.0266	8.12	1.23
Thyroid:	0.118	36.3	5.49

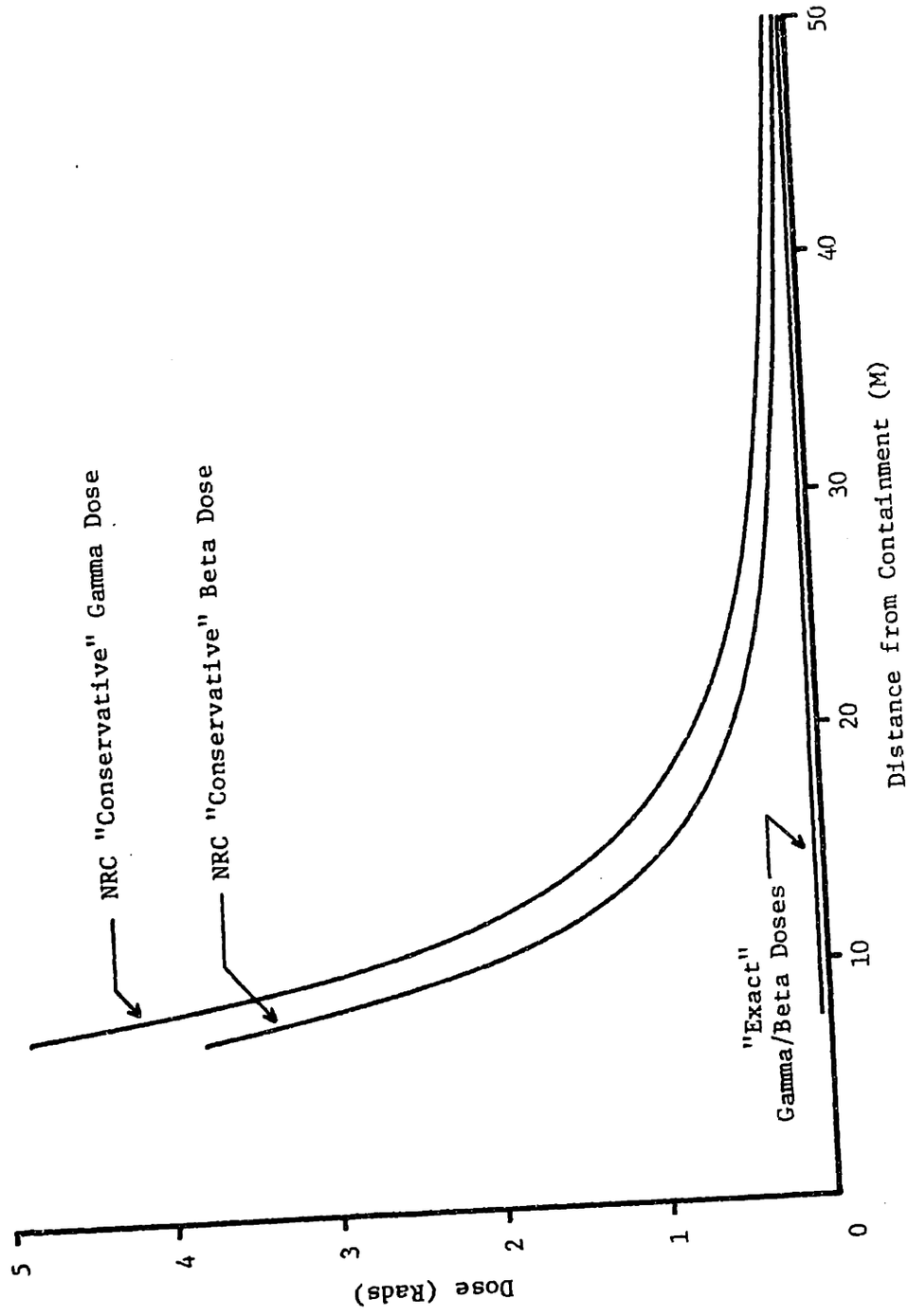

Figure 3.2 Leakage Whole-body Doses

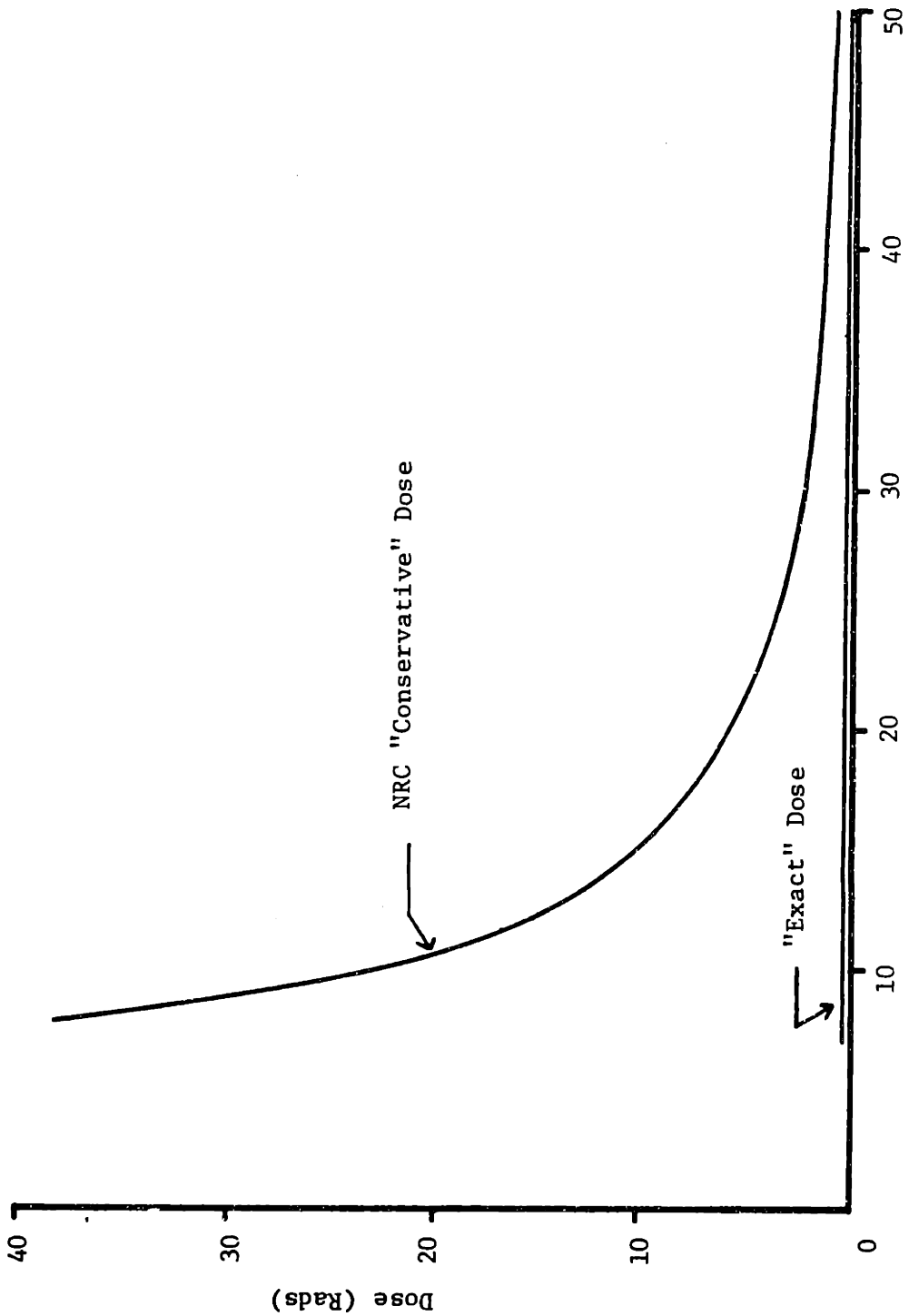

Figure 3.3 Leakage Thyroid Doses

CHAPTER 4

DIRECT GAMMA DOSE

4.1 General

Those isotopes which do not leak from the containment will constitute a source of gamma radiation. The concrete shadow shield is designed to attenuate this radiation and reduce the hazard to individuals near the containment. Due to the short exclusion area distances involved, the gamma dose from radiation penetrating the shadow shield will be non-neglible. In addition, the fission products located in that portion of the containment volume above the shadow shield are only shielded by the steel shell. In the following sections the dose resulting from these two penetrations will be determined.

4.2 Gamma Source Term

The gamma source within the containment will consist of those fission products which deposit or plateout and those airborne fission products which do not leak out. As stated in Sec. 3.8 the initial quantity of fission product i airborne in the containment is equal to $F_R^i Q_s^i$. This will be reduced over time due to leakage and decay. The quantity which deposits inside the containment is equal to

$$F_s^i F_f^i F_p^i (1-F_c^i) Q_s^i$$

which can also be expressed as

$$\frac{(1-F_c^i)}{F_c^i} \; F_R^i Q_s^i$$

The quantity of deposited fission products will decrease over time only by radioactive decay.

The time-dependent containment inventory of fission product i is therefore

$$Q_c^i(t) = F_R^i Q_s^i e^{-(\lambda_L + \lambda_i)t} + \left(\frac{1}{F_c^i} - 1\right) F_R^i Q_s^i e^{-\lambda_i t} \text{ Ci}$$

or

$$Q_c^i(t) = F_R^i Q_s^i \left[e^{-(\lambda_L + \lambda_i)t} + \left(\frac{1}{F_c^i} - 1\right) e^{-\lambda_i t} \right] \text{ Ci} \qquad (4.1)$$

The total number of decay emissions from isotope i over the two hour period is given by

$$Q_{c_T}^i = (3.7 \times 10^{10} \text{ dis/sec-Ci}) \int_0^{7200} Q_c^i(t)dt$$

which after integration, is

$$Q_{c_T}^i = 3.7 \times 10^{10} \; F_R^i Q_s^i \left[\frac{1-e^{-(\lambda_L + \lambda_i)7200}}{\lambda_L + \lambda_i} + \left(\frac{1}{F_c^i} - 1\right) \frac{1 - e^{-\lambda_i 7200}}{\lambda_i} \right] \text{ dis} \qquad (4.2)$$

Resulting values of $Q_{c_T}^i$ for each isotope are listed in Appendix A, Table A.5.

The energy and abundance of each isotope's gamma decay spectrum

are also shown in Table A.5. For convenience, photons have been grouped into discrete energies following a logrithmic scale, with individual photons being allocated to the closest energy.

The total number of emissions for each energy is then equal to the product of the number of emissions, $Q^i_{c_T}$, for each isotope and the photon abundance for that isotope at that energy, summed over all isotopes. The resulting total number of gammas for each energy is divided by the containment volume and duration of release to obtain the time-averaged total containment volumetic source strength, S_{v_T}. Values of S_{v_T} for each energy E are listed in Table 4.1.

4.3 Direct Dose Modeling

From any given point on the ground the containment can be divided into two volumes, that which lies above the plane passing through the top edge of the shadow shield and the detector and that which lies below. These volumes will be designated V_1 and V_2 respectively, as shown in Fig. 4.1.

That portion of the containment volume which is contained in V_1 can be estimated by approximating V_1 as one half of an ellipsoid with dimensions a, d, and e as shown. The volume V_1 may then be obtained from

$$V_1 = 1/2 \times \frac{4}{3} \pi \text{ ade}$$

or

$$V_1 = \frac{2}{3}\pi\text{ade} \qquad (4.3)$$

TABLE 4.1

Containment Volume Source Strength

Gamma Energy E (Mev)	Total Containment Volume Source Strength S_{V_T} (Photons/cm^3-sec)
0.03	3.35×10^{2}
0.04	6.11×10^{-1}
0.05	2.16×10^{2}
0.06	1.96×10^{1}
0.08	1.25×10^{4}
0.10	9.90×10^{0}
0.15	6.72×10^{3}
0.20	7.14×10^{3}
0.30	7.22×10^{3}
0.40	7.37×10^{3}
0.50	5.29×10^{3}
0.60	4.46×10^{3}
0.80	1.08×10^{4}
1.0	2.69×10^{3}
1.5	3.70×10^{3}
2.0	1.04×10^{4}
3.0	1.18×10^{3}
4.0	1.32×10^{1}

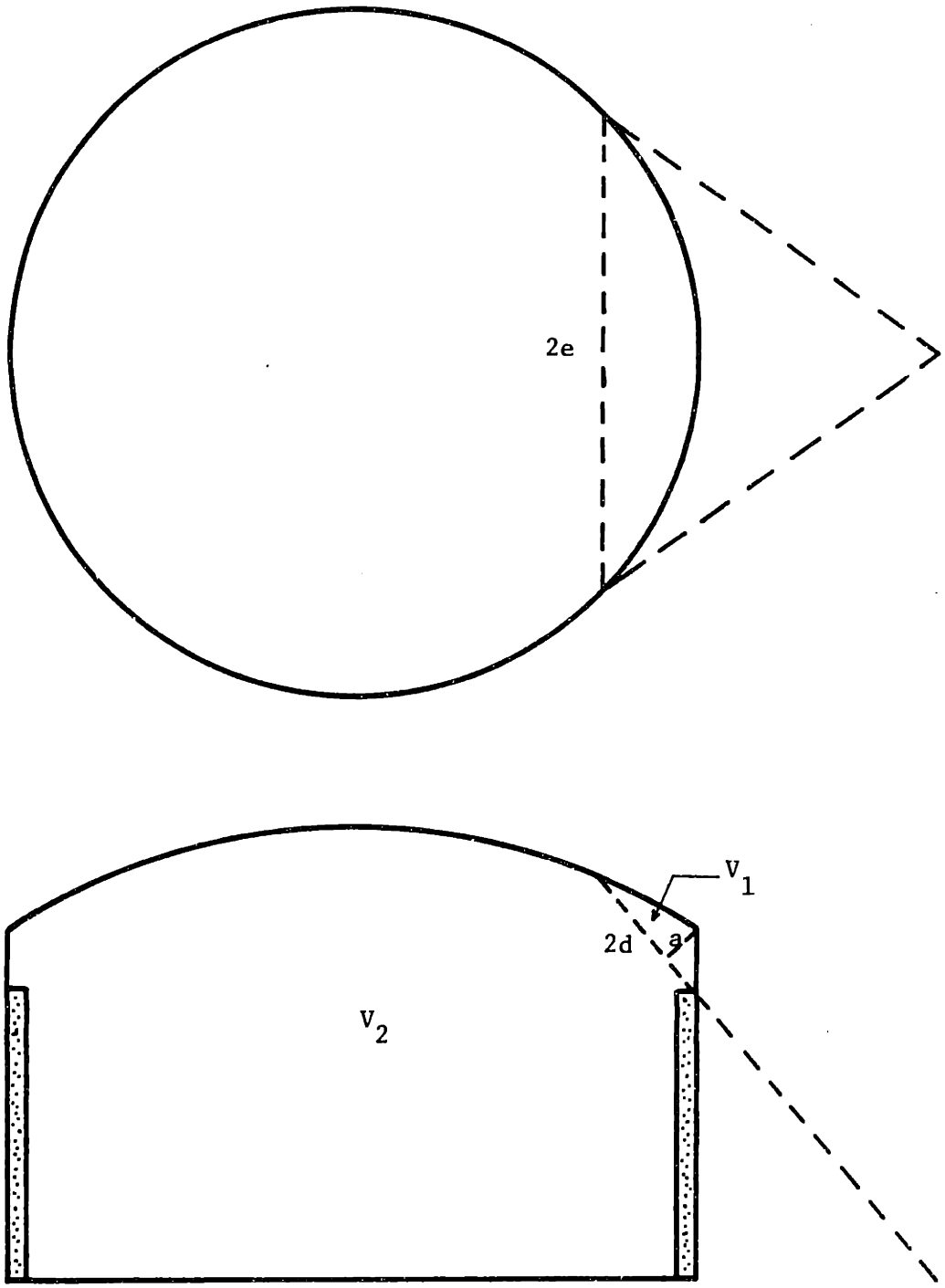

Figure 4.1

Direct Dose Containment Volume Division

The parameters of V_1 are:

for the back fence (8 m): a = 1.22 m
d = 2.44 m
e = 7.62 m

and for the front fence (21 m): a = 1.83 m
d = 6.10 m
e = 10.7 m

Substitution in Eq. 4.3 yields the result:

$$V_1(8) = 47.5\ m^3$$

$$V_1(21) = 250\ m^3$$

Since $V = 4.73 \times 10^3\ m^3$, it is seen that

$$V_1(8) \sim .01\ V \tag{4.4}$$

$$V_1(21) \sim .05V \tag{4.5}$$

Consequently, since $V_1 + V_2 = V$, V_2 can be expressed as

$$V_2(8) = \sim .99V \tag{4.6}$$

$$V_2(21) = \sim .95V \tag{4.7}$$

Volume V_1 can be considered to be a volumetric gamma source shielded by a single steel slab and V_2 a volumetric source shielded by a two layer concrete/steel slab.

The easiest method available to determine the dose from volumetric sources is the point kernel technique. Since each gamma decay and attenuation interaction is independent of any other, a volume source can be considered to be a number of point isotropic sources.

A ray is drawn from a differential source point to the detector and the detector response due to the ray path determined. This is the kernel response. The effect due to all points is obtained by integrating over the volume of the source. Point kernel integrations have been performed for a number of standard shapes and are available in any of the standard shielding manuals [27, 28, 29].

In this study the upper volume will be treated as a sphere of volume V_1 located at a point just above the shadow shield and the lower volume as a right circular cylinder of volume V_2 with a height to radius ratio of one (see Fig. 4.2). Other source geometrics such as a line source and truncated cone were also considered but found to be less conservative.

4.4 Penetration Calculations

4.4.1 Steel Shell Penetration

A spherical volume source of constant source strength S_v (photons/cm^3-sec) can be approximated by a disk of the same radius having a surface source strength

$$S_A = \frac{4}{3} RS_v \quad \text{photons/cm}^2\text{-sec} \tag{4.8}$$

located at a self-absorption distance z [29] (see Fig. 4.3a). Assuming that the containment atmosphere is primarily air, self-absorption will be small and it is conservative to assume $z = 0$. The volume then reduces to a disk of radius R_1 located a distance x_1

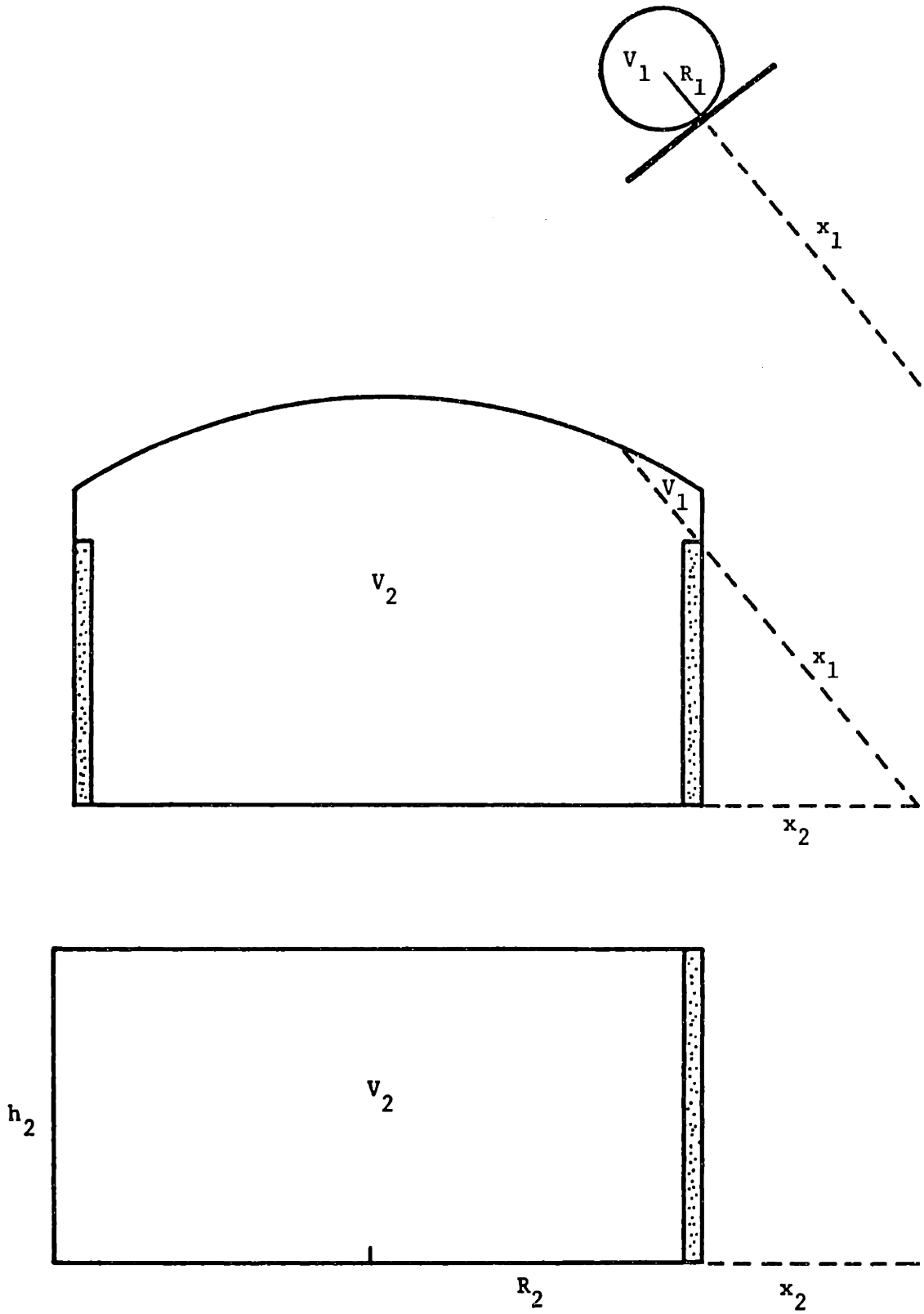

Figure 4.2

Direct Dose Containment Volume Transformations

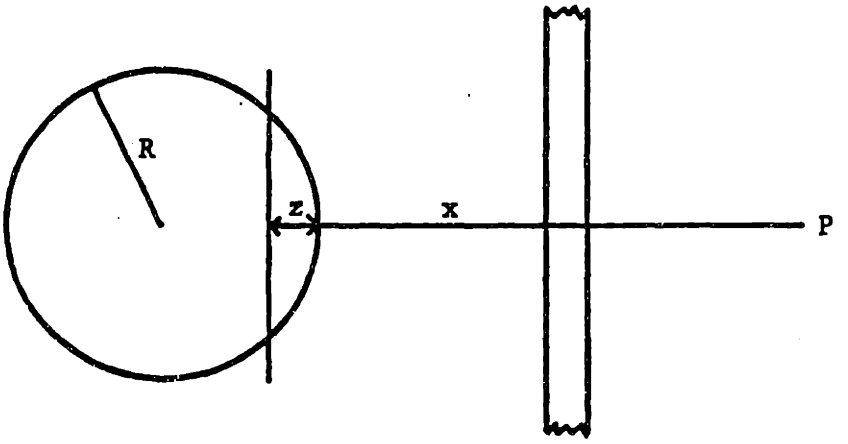

Figure 4.3a
Sphere to Disk Source Transformation

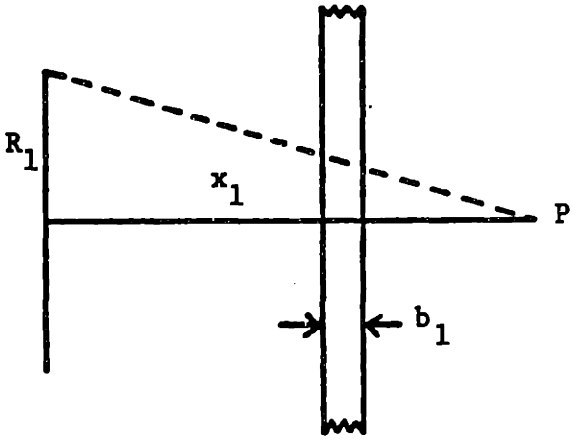

Figure 4.3b
Geometry for Disk Surface Source with Slab Shield

from the exclusion area boundary point P as shown in Fig. 4.3b.

The flux received at P due to photons of energy E from this disk source shielded by a steel slab is [29]:

$$\phi_\gamma = \frac{BS_{A1}}{2}\left[E_1(b_1) - E_1(b_1\sec\theta_1)\right] \text{ photons/cm}^2\text{-sec} \qquad (4.9)$$

where:

ϕ_γ = Photon flux (photons/cm^2-s)

B = Build up factor

S_{A1} = surface source strength for volume V_1 and energy E (photons/cm^2-sec)

$b_1 = \mu_{ST}T_{ST}$ (Number of mean free paths in the steel shield)

μ_{ST} = Linear attenuation coefficient for steel (cm^{-1})

T_{ST} = Steel thickness (cm)

$$E_1(b) = \int_b^\infty \frac{e^{-t}}{t}\,dt$$

for the derivation of Eq. 4.9 see Appendix C. Substituting for S_A from Eq. 4.8 the flux becomes

$$\phi_\gamma = \frac{2}{3} BR_1 S_{v1}\left[E(b_1) - E_1\ (b_1\sec\ \theta)\right] \text{ photons/cm}^2\text{-sec} \qquad (4.10)$$

Buildup and attenuation in the air will be neglected. Both effects are small and tend to cancel each other. Values of μ and subsequent values of b_1 are shown in Tables A.6 and A.7.

The dose at P is determined using the conversion factor C_D in

$$\text{Dose} = C_D\phi_\gamma \quad \text{rads} \qquad (4.11)$$

where

$$C_D = \frac{(E \text{ Mev/photon})\ (1.6 \times 10^{-6} \text{ergs/Mev})(\mu_a \text{ cm}^2/\text{g})(7200\text{s})}{100 \text{ ergs/g-rad}}$$

which reduces to

$$C_D = 1.15 \times 10^{-4}\ E\mu_a \quad \text{rads/photons/cm}^2\text{-s} \tag{4.12}$$

where μ_a = True energy absorption coefficient in air (cm^2/g). (See Table A.6)

(Note: for convenience, the energy dependency notation (E) has been dropped in references to S_v, C_D, dose, μ_a, etc. The reader should keep in mind that all dose equations are for a given photon energy, not the total dose).

Substituting C_D and ϕ_γ into Eq. 4.11 the dose becomes

$$\text{Dose} = 7.67 \times 10^{-5}\ E\mu_a B R_1 S_{v_1} \left[E_1(b_1) - E_1(b_1 \sec\theta_1) \right] \text{ rads} \tag{4.13}$$

The buildup factor B (a function of energy and mean free path length) is included to reflect the tendency during broad beam attenuation for gammas not originally on a direct path to the detector to scatter towards the detector while traversing the medium. It is defined as the ratio of the total detector response to the uncollided (attenuated) response. Tabulated values of exposure (dose) and energy deposition build up factors are available for point isotropic and broad beam parallel sources in an infinite medium. Point isotropic dose build up factors for steel are shown in Table A.8. The use of infinite medium factors is conservative since build up factors for

finite shield geometry are smaller [27]. Strictly speaking, the build up factor values for point sources cannot, in the case of extended sources, be used as simple multiplicative factors; they can only be combined with the point kernel in the integrand. This is because the penetration paths of the primary radiation in the shield are always longer for extended sources than the penetration paths of the normal incident radiation from point sources, with a consequent increase in the build up factor [27].

One way to combine the build up factor in the integrand is to express it as an analytic expression which is compatible with the integration. One of the most common forms is the Taylor formula [27]:

$$B = A\, e^{-\alpha_1 \mu T} + (1-A)\, e^{-\alpha_2 \mu T} \tag{4.14}$$

in which A, α_1, and α_2 are energy-dependant coefficients which are fitted to the point build up factor values. Substituting the expression for B into the equation for $E_1(b)$ and integrating the result is

$$E_1(b_1) = AE_1(b_1') + (1-A)\, E_1(b_1'')$$

where $b_1' = (1 + \alpha_1)b_1$

$b_1'' = (1 + \alpha_2)b_1$

Therefore, Eq. 4.13 can be rewritten as

$$\text{Dose} = 7.67 \times 10^{-5} E\mu_a R_1 S_{v_1} \Big[AE_1(b_1') + (1-A)E_1(b_1'') - AE_1(b_1'\sec\theta_1) - (1-A)E_1(b_1''\sec\theta_1) \Big] \text{ rads} \tag{4.15}$$

The function $E_1(b)$ cannot be evaluated analytically. Numerically

determined graphs are available in the literature but interpolation is difficult and inaccurate. Fortunately it is possible to determine the difference between two $E_1(b)$ functions using the relation [27]

$$E_1(b) - E_1\left[b(1+\delta)\right] = \delta e^{-b} \tag{4.16}$$

for $\delta \ll 1$ and $b > 0$.

For this situation, $(1+\delta) = \sec\theta$

or $\delta = \sec\theta - 1$

Substitution into Eq. 4.15 yields the final result,

$$\text{Dose} = 7.67 \times 10^{-5} E\mu_a R_1 S_{v1} \left[A(\sec\theta_1 - 1)e^{-b_1'} + (1-A)(\sec\theta_1 - 1)e^{-b_1''}\right] \text{ rads} \tag{4.17}$$

where $b_1' = (1+\alpha_1)b_1$

$b_1'' = (1+\alpha_2)b_1$

Assuming that the fission products are uniformly distributed in the containment, the volume relations in Eqs. 4.4 and 4.5 lead to the source strength relations

$$S_{v1}(8) = .01\ S_{v_T}$$

$$S_{v1}(21) = .05\ S_{v_T}$$

The scattering geometry parameters are:

8 m: $\theta_1 = 0.179$ radians

$R_1 = 2.25 \times 10^2$ cm

21 m: $\theta_1 = 0.169$ radians

$R_1 = 3.90 \times 10^2$ cm

Values of the coefficients A, α_1, and α_2 are listed in Table A.9 with the resulting doses listed in Table 4.2. Since the Taylor coefficients are not available for E < 0.5 Mev, the lower energy doses have been computed using the appropriate point build up factor data from Table A.7 in

$$\text{Dose} = 7.67 \times 10^{-5} E\mu_a R_1 S_{v_1} B(\sec\theta_1 - 1)e^{-b_1} \text{ rads} \qquad (4.18)$$

Doses for E < .10 have not been determined as build up factor data for steel in this energy range is not available and the increasing attenuation at lower energies makes the dose at these energies negligible.

As seen in Table 4.2 the total dose at 21 meters is larger than that at 8 meters. This is due to the fact that the portion of the containment volume seen above the shadow shield increases as point P moves away from the containment. An estimate of the behavior of the total dose byeond 21 meters was made by tracking the behavior of the largest dose component, that of E = 2.0 Mev. The results, shown in Fig. 4.5, indicate that the total steel penetration dose goes through a maximum of $\sim 6.5 \times 10^{-2}$ rads at a distance of $\sim$ 37 meters. Beyond this the distance effect overcomes the increase in volume and the dose decreases.

4.4.2 Shadow Shield Penetration

As stated previously, that portion of the containment volume

TABLE 4.2

Steel Dome Penetration Doses

Gamma Energy E (Mev)	Dose (Rads) 8m	21m
0.10	1.31×10^{-8}	1.05×10^{-7}
0.15	3.80×10^{-5}	2.95×10^{-4}
0.20	7.78×10^{-5}	6.05×10^{-4}
0.30	1.46×10^{-4}	1.13×10^{-3}
0.40	2.16×10^{-4}	1.68×10^{-3}
0.50	1.95×10^{-4}	1.52×10^{-3}
0.60	1.99×10^{-4}	1.55×10^{-3}
0.80	6.36×10^{-4}	4.94×10^{-3}
1.0	1.92×10^{-4}	1.49×10^{-3}
1.5	3.62×10^{-4}	2.82×10^{-3}
2.0	1.24×10^{-3}	9.63×10^{-3}
3.0	1.85×10^{-4}	1.44×10^{-3}
4.0	2.52×10^{-6}	1.96×10^{-5}
Total	3.49×10^{-3}	2.71×10^{-2}

behind the shadow shield can be treated as a right circular cylinder of radius R_2 and height h_2 shielded by a slab shield of thickness b_2 as shown in Fig. 4.4.

For this situation the flux at point P is given by [27]:

$$\phi_\gamma = \frac{BR_2S_{v2}}{2\pi} G\ (k,p,\mu_s R_2,\ b_2)\ \text{photons/cm}^2\text{-s} \qquad (4.19)$$

where: $k = \frac{h_2}{R_2}$

$p = \frac{s}{R_2}$ (must be ≥ 1.25)

μ_s = Linear attenuation coefficent in the source medium (cm^{-1})

$b_2 = \mu_c T_c + \mu_{ST} T_{ST}$ = Total shadow shield thickness in mean free paths

G = Attenuation function

The derivation of Eq. 4.19 and details of the attenuation function G are contained in Appendix D. The above equation can also be used for a source with no self-absorption by setting $\mu_s R_2 = 0$.

As before, the dose at P is found by use of the conversion factor C_D, with the result

$$\text{Dose} = \frac{1.15 \times 10^{-4}\ E\mu_a BR_2S_{v2}}{2\pi} G(k,p,\mu_s R_2,b_2)\ \text{rads} \qquad (4.20)$$

The exact build up factor for a multi layer shield can only be determined by the solution of the Boltzmann transport equation, with appropriate boundary conditions, by a numerical method, such as Monte Carlo technique. For most practical purposes simpler approximate

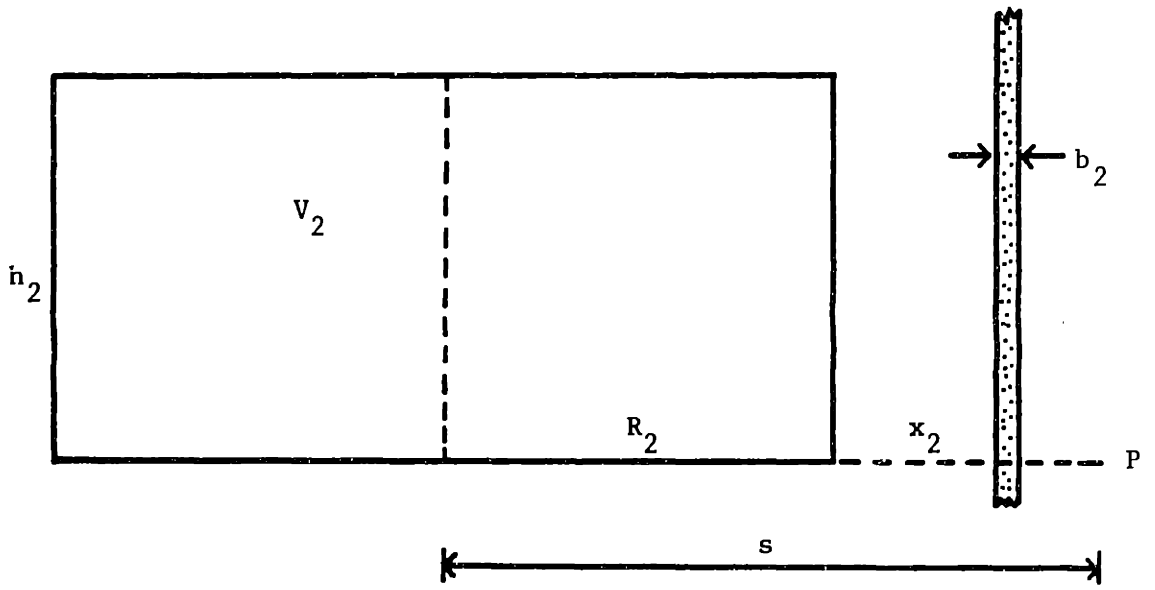

Figure 4.4

Geometry for Cylindrical Volume Source with Slab Shield

methods are adequate. One method is to use the build up factor data for the last material penetrated based on the thickness (in mean free paths) of the entire shield. This method can only be used if the last layer is at least three mean free paths thick [30]. Alternatively, if almost all of the attenuation (measured in mean free paths) occurs in a particular layer, then the build up factor is based on that material and the total thickness (in MFP's) of the shield [27].

Referring to Table A.7 one can see that build up factor data for concrete should be used for all energies equal to or greater than 0.10 Mev. and that for steel below 0.10 Mev. Note that the concrete portion of the shadow shield is treated as a layer of pure concrete when in actuality it contains numerous steel reinforcing bars. This is conservative as the attenuation in concrete is less than that in steel while the build up factor in concrete is greater than in steel.

As before, greater accuracy can be achieved by incorporating an analytic build up factor expression into the integrand, in this case the G function. Using the Taylor formula the dose now becomes

$$\text{Dose} = \frac{1.15 \times 10^{-4} E\mu_a R_2 S_{v_2}}{2\pi} \left[AG(k,p,\mu_s R_2, b_2') + (1-A)G(k,p,\mu_s R_2, b_2'') \right] \text{ rads} \qquad (4.21)$$

where

$$b_2' = (1 + \alpha_1)b_2$$

$$b_2'' = (1 + \alpha_2)b_2$$

Values of the Taylor coefficients for concrete are listed in Table A.9.

S_{v_2} is related to the total source strength S_{v_T} through Eqs. 4.6 and 4.7.

The parameters of the G function are determined as follows: From Eqs. 4.6 and 4.7 the respective volumes are

$$V_2(8) = 4.68 \times 10^3 \text{ m}^3$$

$$V_2(21) = 4.49 \times 10^3 \text{ m}^3$$

For convenience, k is set equal to one. This eliminates one set of interpolations in the G function tables and is not too far from the actual containment h/R ratio. Given that k = 1, and therefore $R_2 = h_2$, the radii can be solved for using

$$V_2 = \pi R_2^2 h_2 \text{ to yield}$$

$$R_2(3) = 11.4 \text{ m}$$

$$R_2(21) = 11.3 \text{ m}$$

Since s is the total distance from the center of V_2 to P and the thickness of the shadow shield is 0.61 m (2 ft) the variable p can be determined to be

$$p(8) = \frac{11.4 + 0.61 + 8}{11.4} \quad \text{or} \quad p(8) = 1.75$$

$$p(21) = \frac{11.3 + 0.61 + 21}{11.3} \quad \text{or} \quad p(21) = 2.90$$

Since self-absorption is neglected $\mu_s R_2 = 0$. Values of b_2' and b_2'' are listed in Table A.10 along with the corresponding G function values.

The resulting doses are included in Table 4.3. Again, doses for E <.10 Mev have not been determined for the same reasons as cited in Sec. 4.4.1. As opposed to the steel penetration dose, the shadow shield dose is a continuously decreasing function of distance, since the volume decreases with distance. An estimate of the shadow shield penetration dose behavior, based on E = 2.0 Mev, is shown in Fig. 4.5

4.5 Summary and Comparison with the SAR

The point-kernel integration techniques used in this section to evaluate the direct gamma dose reaching the exlusion area boundary indicate that the estimated two-hour dose due to both steel and shadow shield penetration is 4.68×10^{-2} rads at the back fence (8 meters from the containment) and 4.76×10^{-2} rads at the Albany St. fence (21 meters from containment). The increasing steel penetration dose is offset by the continuously decreasing shadow shield dose to produce the total dose curve shown in Fig. 4.5 with a maximum of $\sim 7.6 \times 10^{-2}$ rads at a distance of $\sim$ 35 meters.

The SAR gives the total dose at 8 meters as $\sim 3.1 \times 10^{-2}$ rads and that at 21 meters as $\sim 2.5 \times 10^{-2}$ rads. The differences are due to the slightly different penetration methodology used in the SAR as well as the different source terms.

TABLE 4.3

Shadow Shield Penetration Doses

Gamma Energy E (Mev)	Dose (Rads) 8m	21m
0.10	1.06×10^{-14}	5.96×10^{-15}
0.15	6.66×10^{-9}	4.91×10^{-9}
0.20	1.49×10^{-7}	1.09×10^{-7}
0.30	2.78×10^{-6}	1.95×10^{-6}
0.40	1.56×10^{-5}	1.08×10^{-5}
0.50	3.76×10^{-5}	2.63×10^{-5}
0.60	6.10×10^{-5}	3.55×10^{-5}
0.80	6.15×10^{-4}	4.13×10^{-4}
1.0	5.23×10^{-4}	1.98×10^{-4}
1.5	3.59×10^{-3}	1.70×10^{-3}
2.0	2.60×10^{-2}	1.27×10^{-2}
3.0	1.23×10^{-2}	5.33×10^{-3}
4.0	2.04×10^{-4}	1.11×10^{-4}
Total	4.33×10^{-2}	2.05×10^{-2}

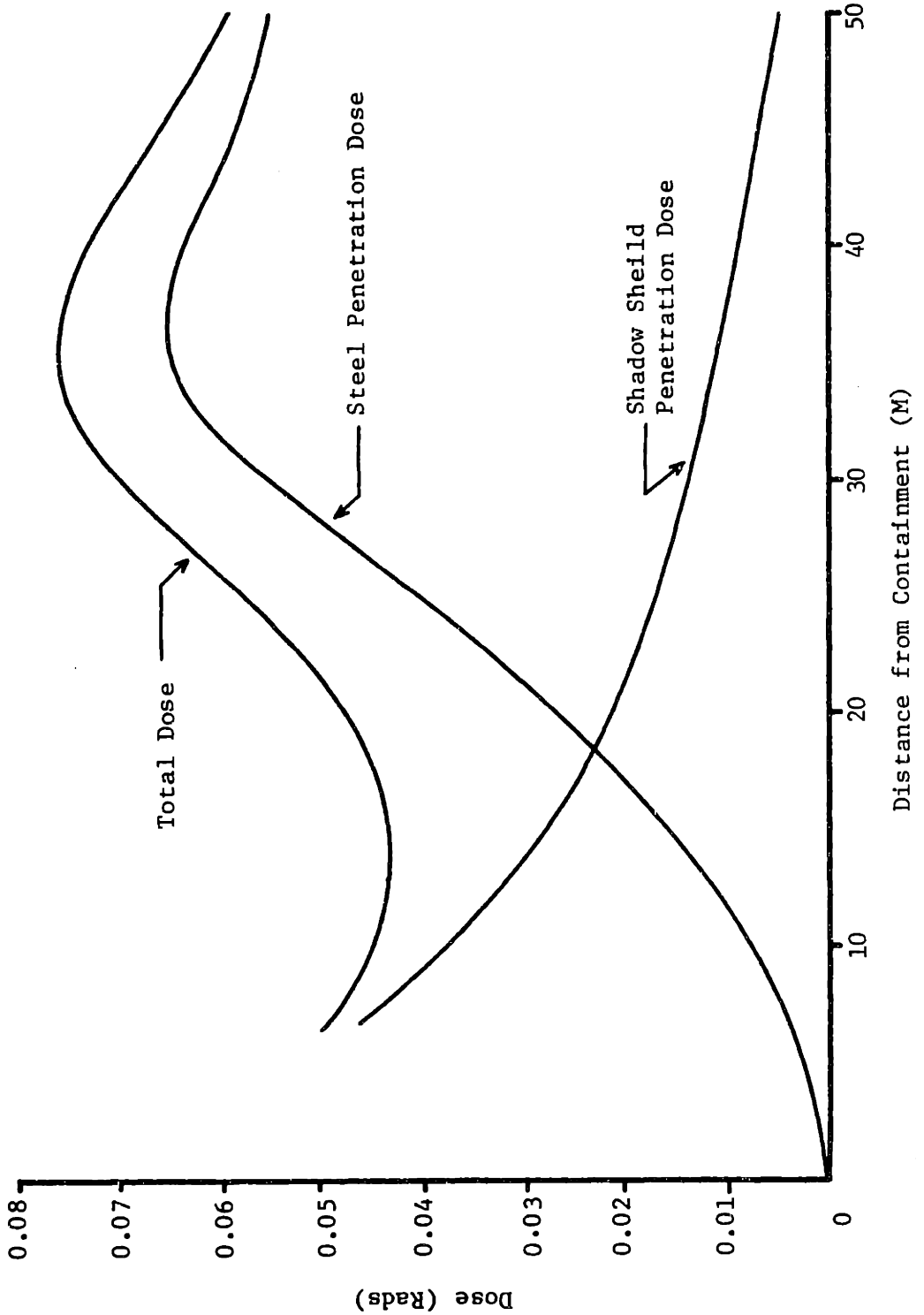

Figure 4.5 Direct Doses

CHAPTER 5

SCATTERED GAMMA DOSE

5.1 General

Although the shadow shield is quite effective in stopping direct radiation, the open top construction leads to the possibility of gamma radiation escaping upwards and being subsequently scattered back towards the ground through interaction with the air or the steel dome. This scattered radiation is commonly called skyshine. In the following sections a skyshine analytical model will be developed and applied to scattering from the air and the steel roof.

5.2 Scattering Model

Consider a point source of strength S photon/sec located a distance x from a detector at point P with a small scattering volume dV located at a distance r_1 from the source and a distance r_2 from the detector as shown in Fig. 5.1.

The scattering angle is $\theta = \psi + \phi$ and the differential dose recieved at P is

$$dD = \frac{C_D SN}{4\pi r_1^2 r_2^2} \frac{d\sigma}{d\Omega}(\theta, E)dV \qquad (5.1)$$

where N = Density of electrons in air = 3.6×10^{20} elec/cm^3 at STP

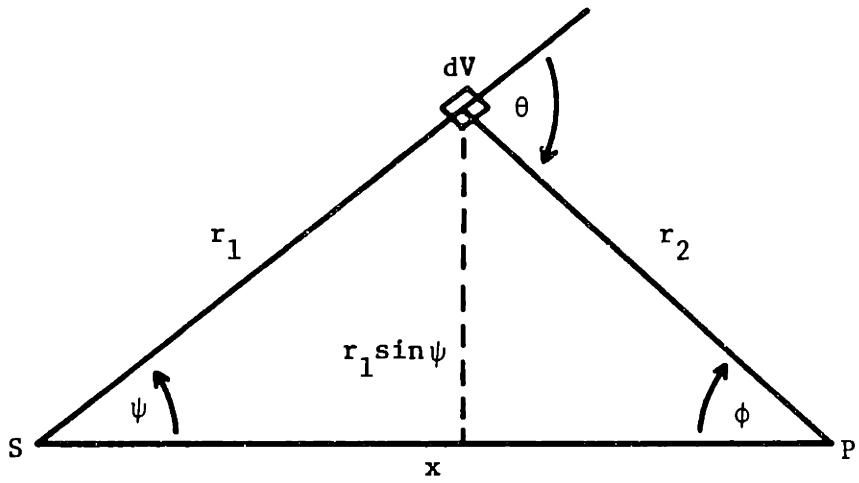

Figure 5.1

Scattering Geometry

$\frac{d\sigma}{d\Omega}(\theta,E)$ = Klein-Nishina differential collision cross-section for angle θ and photon energy E. (cm^2/steradian).

Eq. 5.1 neglects build up and attenuation in the air. There is cylindrical symmetry about x so that [31]

$$dV = (2\pi_1 \sin\psi)(r_1 d\psi)(dr_1)$$

From the law of sines it is possible to state

$$\frac{r_1}{\sin\phi} = \frac{r_2}{\sin\psi} = \frac{x}{\sin[\pi - (\psi+\phi)]} = \frac{x}{\sin(\psi + \phi)} \qquad (5.2)$$

Differentiating while holding ψ constant yields

$$\frac{dr_1}{d\phi} = \frac{x \sin(\psi + \phi)\cos\phi - x \cos(\psi + \phi) \sin\phi}{\sin^2(\psi + \phi)}$$

which simplifies to

$$\frac{dr_1}{d\phi} = \frac{x \sin\psi}{\sin^2(\psi + \phi)}$$

Substituting from Eq. 5.2, this becomes

$$dr_1 = \frac{r_2^2}{x \sin \psi} \, d\phi$$

dV can now be written as

$$dV = (2\pi r_1 \sin\psi)(r_1 d\psi)\left(\frac{r_2^2}{x \sin\psi}\, d\phi\right)$$

or

$$dV = \frac{2\pi r_1^2 r_2^2}{x}\, d\psi d\phi \tag{5.3}$$

with the result that

$$dD = \frac{C_D SN}{2x}\,\frac{d\sigma}{d\Omega}(\theta,E)\,d\psi d\phi \tag{5.4}$$

Dividing by a factor of 2 to include only the area above the S-P plane and integrating the total dose received at P is

$$\text{Dose} = \frac{C_D SN}{4x}\int_0^{\pi}\int_0^{\pi-\psi}\frac{d\sigma}{d\Omega}(\theta,E)\,d\psi d\phi \quad \text{rads} \tag{5.5}$$

The Klein-Nishina differential collision (flux) cross-section is given by [32]

$$\frac{d\sigma}{d\Omega} = \frac{r_e^2}{2}\left(\frac{E'}{E}\right)^2\left(\frac{E}{E'} + \frac{E'}{E} - \sin^2\theta\right)\text{cm}^2/\text{steradian} \tag{5.6}$$

where r_e = Classical radius of the electron = 2.818×10^{-13} cm

E = Incident photon energy (Mev)

E' = Scattered photon energy (Mev)

E and E' are related by [32]

$$\frac{E'}{E} = \frac{1}{1 + \frac{E}{.511}(1 - \cos\theta)} \tag{5.7}$$

The greatest energy loss occurs when $\theta = 180°$ and the energy loss is zero at $\theta = 0°$. The Klein-Nishina formula reflects the fact that gamma (Compton) scattering becomes peaked in the forward direction with increasing photon energy.

5.3 Air Scattering

Since the higher energy photons will tend to scatter forward with little energy loss the containment volume will be divided into two source regions. The domed portion above the shadow shield, from which photons need only scatter through small angles to reach the ground, will be designated V_u. The lower portion within the shadow shield, which requires large scattering angles to reach the ground, will be designated V_ℓ.

5.3.1 Upper Containment

Assuming the fission products in the dome are concentrated as a point source at the center the scattering geometry is as shown in Fig. 5.2.

Eq. 5.5 can be applied directly if the limits of integration are changed so that [33]

$$\text{Dose} = \frac{C_D S_u N}{4x} \int_{\psi_0}^{\pi-\phi_0} d\psi \int_{\phi_0}^{\pi-\psi_0} d\phi \, \frac{d\sigma}{d\Omega} (\theta = \psi + \phi) \qquad \text{rads} \qquad (5.8)$$

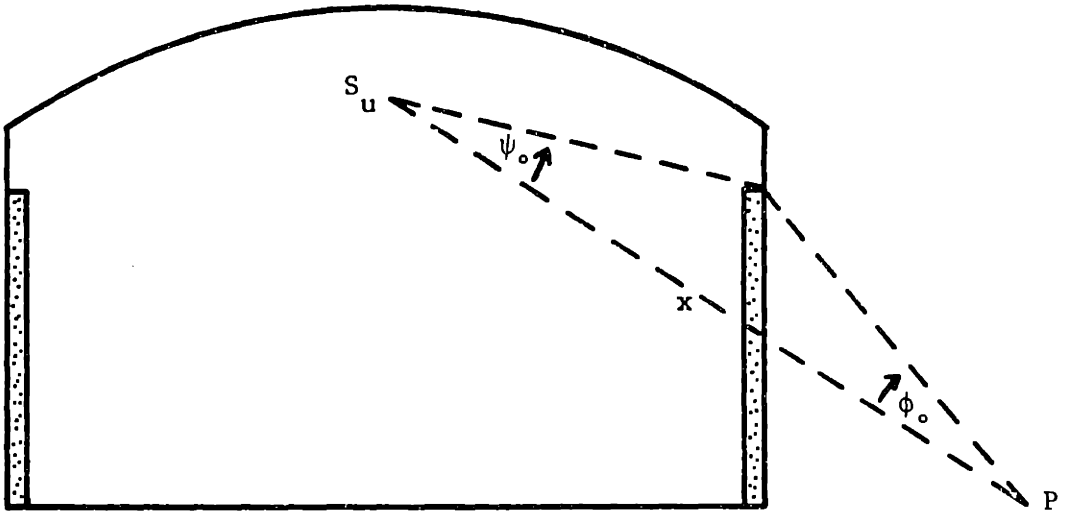

Figure 5.2

Upper Containment Gamma Source Scattering Geometry

where S_u = Source strength in the dome (photons/sec)

ψ_0 = Initial value of ψ (radians)

ϕ_0 = Initial value of ϕ (radians)

Only the area above the S-P plane is considered as the shadow shield will prevent interactions below this plane. In addition, the above limits of integration are conservative as the presence of the ground will prevent ϕ from actually reaching the value $\pi - \psi$. No adjustment is made here to reflect this since in the next section (lower containment scattering) ϕ will be able to reach $\pi - \psi$.

Eq. 5.8 can only be evaluated numerically. A simple method is to approximate the first integral by a summation so that

$$\text{Dose} = \frac{C_D S_u N}{4x} \sum_{\psi=\psi_0}^{\pi-\phi_0} \Delta\psi \int_{\phi_0}^{\pi\ \psi} \frac{d\sigma}{d\Omega}(\theta = \psi + \phi)\, d\phi \quad \text{rads} \qquad (5.9)$$

This allows the value of ψ in $\theta = \psi + \phi$ to be fixed and the second integral can be evaluated with a standard numerical technique such as Simpson's rule. The number of intervals for ψ and ϕ can be adjusted to whatever accuracy is desired.

The total containment source strength S_c (photons/sec) is calculated by multiplying the volumetric source strengths in Table 4.1 by the volume of the containment. The results are given in Table 5.1.

S_u can be related to S_c by the fact that (from Appendix B) $V_u \sim 0.3V$. If the fission products are again assumed to be distributed uniformly, then $S_u = 0.3\ S_c$.

TABLE 5.1

Containment Scattering Source Strength

Gamma Energy E (Mev)	Total Containment Source Strength S_c (Photons/sec)
0.03	1.59×10^{12}
0.04	2.89×10^{9}
0.05	1.02×10^{12}
0.06	9.27×10^{10}
0.08	5.89×10^{13}
0.10	4.68×10^{10}
0.15	3.18×10^{13}
0.20	3.38×10^{13}
0.30	3.42×10^{13}
0.40	3.48×10^{13}
0.50	2.51×10^{13}
0.60	2.11×10^{13}
0.80	5.10×10^{13}
1.0	1.27×10^{13}
1.5	1.75×10^{13}
2.0	4.90×10^{13}
3.0	5.59×10^{12}
4.0	6.25×10^{10}

The dose conversion factor C_D requires some discussion. Since the dose at P is dependent on the energy of the scattered photon, C_D in this case is

$$C_D = 1.15 \times 10^{-4} E' \mu_a (E')$$

The scattering energy E' is constantly changing since it is dependent on the angle θ. Technically then, C_D should be inside the summation and calculated each time a new θ (and E') is determined. This complication can be simply overcome by noting that

$$E' = E\left(\frac{E'}{E}\right)$$

and

$$\left(\frac{E'}{E}\right)\frac{d\sigma}{d\Omega} = \frac{d\sigma_s}{d\Omega}$$

where $\frac{d\sigma_s}{d\Omega}$ = Klein-Nishina differential scattering (energy) cross section.

which is given by

$$\frac{d\sigma_s}{d\Omega} = \frac{r_e^2}{2}\left(\frac{E'}{E}\right)^3\left(\frac{E}{E'} + \frac{E'}{E} - \sin^2\theta\right) \quad \text{cm}^2/\text{steradian} \tag{5.10}$$

The collision cross-section calculates the fraction of the flux which is scattered into θ while the scattering cross-section calculates the fraction of incident energy scattered into θ. Therefore,

in Eq. 5.9 $E'\frac{d\sigma}{d\Omega}$ can be replaced by $E\frac{d\sigma_s}{d\Omega}$.

Since E is a constant it can be removed from the integral. The absorption coefficient $\mu_a(E')$ can be conservatively treated by replacing it with $\bar{\mu}_a(E)$, which is defined as the largest value of $\mu_a(E')$ within the scattered energy range E to E'_{min} (corresponding to 180° scattering). Values of E'_{min} and $\bar{\mu}_a$ are listed in Table A.6.

Finally, since the photons must pass through the steel shell credit can be taken for attenuation in the steel. It is conservative to use the minimum (3/8 in) thickness b_1 (where $b_1 = \mu_{ST}T_{ST}$ is the steel thickness in number of mean free paths.)

The two hour dose at point P is then given by

$$\text{Dose} = \frac{1.15 \times 10^{-4} S_u N E \bar{\mu}_a e^{-b_1}}{4x} \sum_{\psi=\psi_0}^{\pi-\phi_0} \Delta\psi \int_{\phi_0}^{\pi-\psi} \frac{d\sigma_s}{d\Omega} (\theta = \psi + \phi) d\phi \quad \text{rads} \quad (5.11)$$

The above equation was evaluated for each energy E using a simple numerical program with sufficient intervals (10) to yield no change in the third significant figure. The geometry parameters used are shown in Table A.11 and the resulting total dose at each distance due to all energies is listed in Table 5.2.

5.3.2 Lower Containment

Since the scattering angle changes significantly as the source moves down into the shadow shield cylinder, the lower containment will

be treated as three equal source points located along the central axis of the cylinder at a height equal to the center of the corresponding slice of the containment. These points will be designated 1, 2, and 3 as shown in Fig. 5.3.

In this case, the lateral sweep of dV in the cross-wise direction is limited by the shadow shield to some value less than π. This azimuthal angle ω is dependent on the depth of the source within the shadow shield and the value of ψ.

Referring to Fig. 5.4a, it can be seen that

$$\omega = 2 \cos^{-1}\left(\frac{d'}{R'}\right)$$

Fig. 5.4b provides the relationship

$$\sin (\psi - \varphi) = \frac{h'}{d'}$$

Substituting, the result is

$$\omega = 2 \cos^{-1}\left[\frac{h'}{R' \sin (\psi - \varphi)}\right] \quad \text{radians} \tag{5.12}$$

For a given point along the central axis h', R', and ψ are constants. Therefore ω is only a function of ψ and can be placed within the scattering integral (in this case within the summation) in place of the original azimuthal angle π.

The strength of each point is $\frac{S_\ell}{3}$, therefore Eq. 5.11 becomes for lower containment scattering points

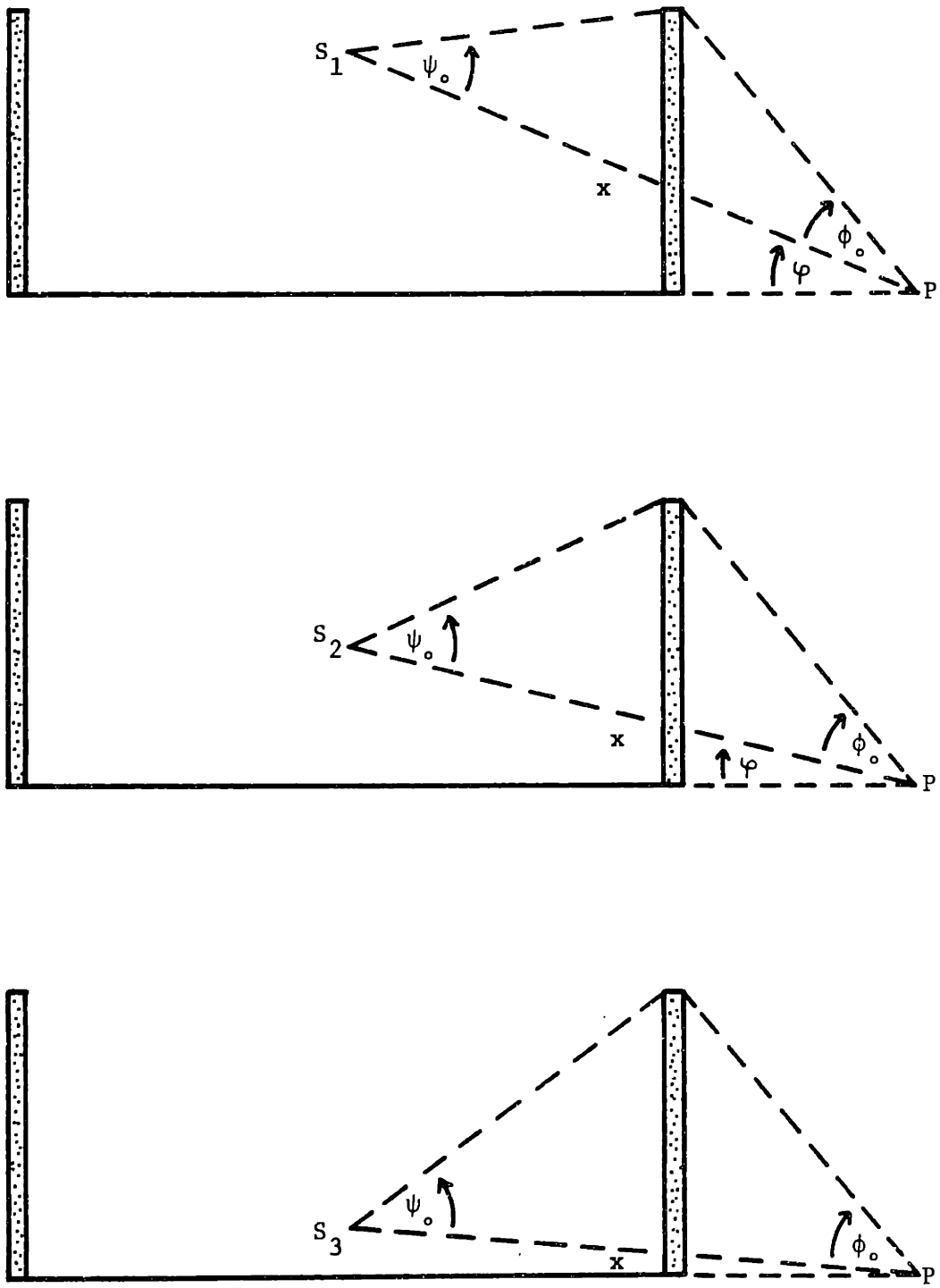

Figure 5.3

Lower Containment Gamma Source Scattering Geometry

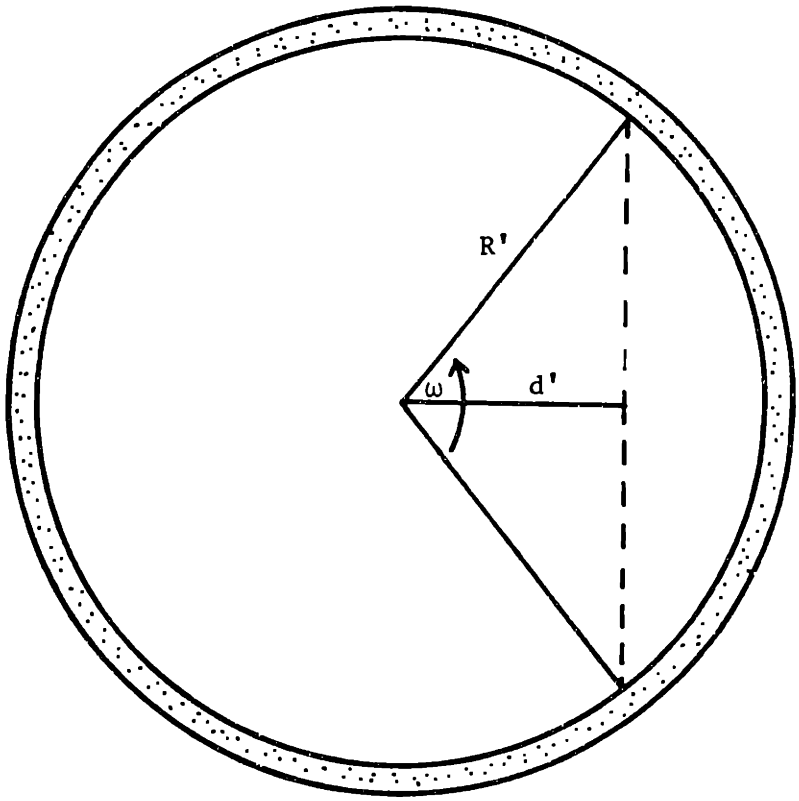

Figure 5.4a

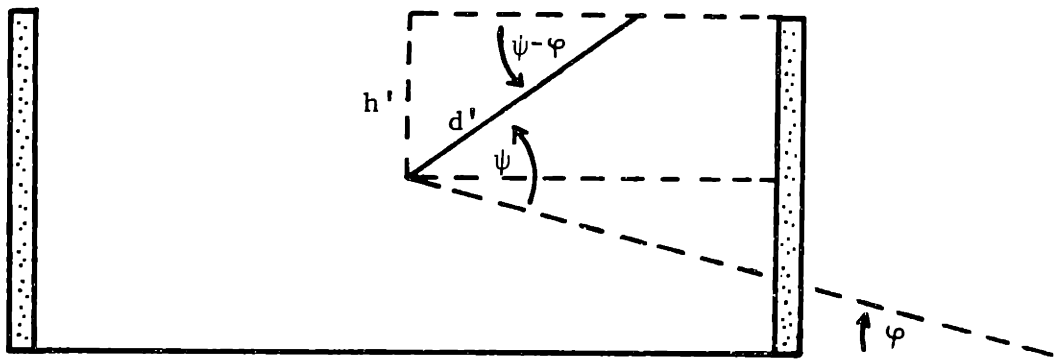

Figure 5.4b

Geometry of the Azimuthal Angle ω

$$\text{Dose} = \frac{1.15 \times 10^{-4}\, S_\ell\, NE\bar{\mu}_a\, e^{-b_1}}{12\pi x} \sum_{\psi=\psi_0}^{\pi-\phi_0} \omega(\psi)\Delta\psi \int_{\phi_0}^{\pi-\psi} \frac{d\sigma_s}{d\Omega}\,(\theta = \psi + \phi)\,d\phi \text{ rads} \tag{5.13}$$

where $S_\ell = 0.7S_c$

and the values x, ψ_0, ϕ_0, h', R' and φ are dependent on the source and detector geometry.

Eq. 5.13 was evaluated for each source point and each energy using the parameters in Table A.11 and the resulting doses are given in Table 5.2.

5.3.3 Air Scattering Results and Comparison with the SAR

The total air scattering doses by energy level are given in Table 5.3. Note that the more isotropic lower energy gammas produce a higher dose at 8 m while the forward scattering high energy gammas yield a higher dose at 21 meters. The conservative air scattering model used in this section estimates the total two hour dose as 1.14×10^{-1} rads at 8 meters and 1.47×10^{-1} rads at 21 meters.

The total 21 meter dose is larger as a result of the enhanced forward peaking due to the smaller scattering angles required to reach the 21 meter point. As distance continues to increase the dose will peak and then fall off as the x term begins to have an effect. An estimate of the peak distance and dose has been made by tracking the behavior of the two highest dose energies, E = 0.8 and 2.0 Mev, for each source point. The results, based on the ratio

TABLE 5.2

Air Scattering Doses by Source Point

Source Point	Dose (Rads) 8m	21m
S_u	6.89×10^{-2}	9.98×10^{-2}
S_1	2.30×10^{-2}	2.46×10^{-2}
S_2	1.34×10^{-2}	1.39×10^{-2}
S_3	8.32×10^{-3}	8.55×10^{-3}

TABLE 5.3

Total Air Scattering Doses by Gamma Energy

Gamma Energy E (Mev)	Dose (Rads) 8m	21m
0.03	5.56×10^{-28}	5.16×10^{-28}
0.04	4.00×10^{-17}	3.74×10^{-17}
0.05	1.97×10^{-9}	1.85×10^{-9}
0.06	2.04×10^{-8}	1.93×10^{-8}
0.08	7.42×10^{-4}	7.08×10^{-4}
0.10	2.30×10^{-6}	2.23×10^{-6}
0.15	5.63×10^{-3}	5.60×10^{-3}
0.20	9.21×10^{-3}	9.44×10^{-3}
0.30	1.27×10^{-2}	1.37×10^{-2}
0.40	1.44×10^{-2}	1.70×10^{-2}
0.50	1.07×10^{-2}	1.26×10^{-2}
0.60	9.08×10^{-3}	1.11×10^{-2}
0.80	2.15×10^{-2}	2.82×10^{-2}
1.0	5.20×10^{-3}	7.19×10^{-3}
1.5	6.48×10^{-3}	1.01×10^{-2}
2.0	1.61×10^{-2}	2.82×10^{-2}
3.0	1.52×10^{-3}	3.10×10^{-3}
4.0	1.43×10^{-5}	3.31×10^{-5}
Total	1.14×10^{-1}	1.47×10^{-1}

of these components to the total dose, are shown in Fig. 5.9 and indicate the maximum total dose is $\sim 1.5 \times 10^{-1}$ rads at a distance of $\sim$ 27 meters.

Only single scattering events have been considered. This is sufficient as it has been shown [34] that the single scattering model derived in Sec. 5.2 yields results which are in almost exact agreement with Monte Carlo air scattering results [35].

The SAR gives air scattering values of ~ 1.55 rads at 8 meters and $\sim 8.3 \times 10^{-1}$ rads at 21 meters. The difference is due to the very conservative scattering model used in the SAR, which does not take full credit for the effects of the scattering angles, energy degradation and shadow shield.

5.4 Steel Shell Scattering

5.4.1 Single Scattering Model

The air scattering model could be directly adopted to determine scattering from the steel shell if the integration could be made to follow the surface of the shell. Since this is not easily done the following approximation will be made.

If the entire scattering volume shown in Fig. 5.5 were composed of steel, then the dose at P due to a source S photons/sec would be

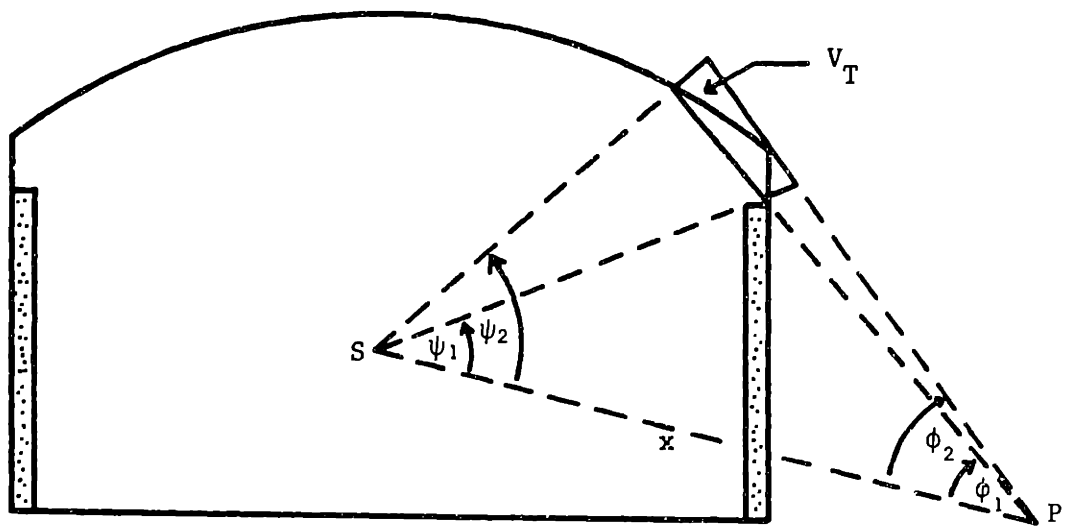

Figure 5.5
Steel Shell Scattering Geometry

$$\text{Dose} = \frac{1.15 \times 10^{-4} SN_{ST} \bar{E\mu}_a e^{-b1}}{4\pi x} \sum_{\psi=\psi_1}^{\psi_2} \omega(\psi)\Delta\psi \int_{\phi_1}^{\phi_2} \frac{d\sigma_s}{d\Omega}(\theta)d\phi \quad \text{rads} \tag{5.14}$$

where N_{ST} = Electron density in steel (electrons/cm^3)

To obtain an estimate of the dose due only to the steel shell Eq. 5.14 is multiplied by the fraction of volume which is steel, namely,

$$\frac{V_{ST}}{V_T}$$

where V_{ST} = Volume of steel shell

V_T = Total scattering volume

V_T can be integrated directly from dV. Including the azimuthal angle,

$$dV = \frac{\omega r_1^2 r_2^2}{x} d\psi d\phi$$

Integrating,

$$V_T = \frac{\omega r_1^2 r_2^2}{x} \int_{\psi_1}^{\psi_2} d\psi \int_{\phi_1}^{\phi_2} d\phi$$

and consequently,

$$V_T = \frac{\omega r_1^2 r_2^2}{x} (\psi_2 - \psi_1)(\phi_2 - \phi_1) \tag{5.15}$$

Substituting in Eq. 5.14, the dose becomes

$$\text{Dose} = \frac{1.15 \times 10^{-4}\ SN_{ST}V_{ST}E\bar{\mu}_a e^{-b}}{4\pi r_1^2 r_2^2(\psi_2 - \psi_1)(\phi_2 - \phi_1)} \sum_{\psi=\psi_1}^{\psi_2} \Delta\psi \int_{\phi_1}^{\phi_2} \frac{d\sigma_s}{d\Omega}(\theta)d\phi \quad \text{rads} \tag{5.16}$$

where the distances r_1 and r_2 are shown in Fig. 5.6.

The electron density in steel is determined from

$$N = \frac{Z\rho N_{Av}}{A_t}$$

where for steel (iron):

$$N_{ST} = \frac{(26\ \text{elec/atom})(7.83\ \text{g/cm}^3)(6.02 \times 10^{23}\ \text{atoms/g-atom})}{55.85\ \text{g/g-atom}}$$

or

$$N_{ST} = 2.19 \times 10^{24}\ \text{elec/cm}^3$$

The volume of steel in the dome is determined from Fig. 5.7 as

$$V_{ST} = T_{ST}(\theta_d LH + \theta_d R_d y)$$

but

$$\theta_d = 2\sin^{-1}\left(\frac{\ell}{2R_d}\right)$$

therefore,

$$V_{ST} = T_{ST}\left[2\sin^{-1}\left(\frac{\ell}{2R_d}\right)\right](LH + R_d y) \quad \text{cm}^3 \tag{5.17}$$

where T_{ST} = Steel thickness = 9.5×10^{-1} cm *

ℓ = Dome segment length (cm)

* - Although the dome portion of the shell is 5/8 in thick, 3/8 in was used here for the entire shell. The resulting smaller steel volume is partially offset by the decreased attenuation. The error introduced by using 3/8 in is estimsted to be less than 10%.

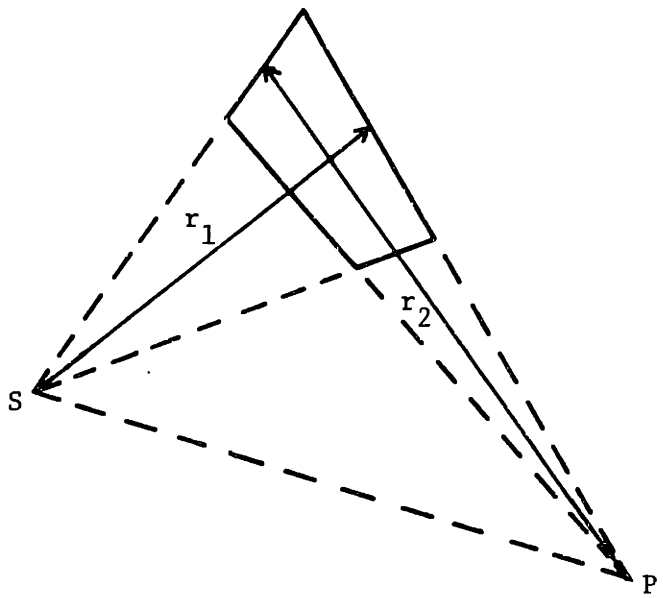

Figure 5.6
Relationship of the Distances r_1 and r_2 to the
Scattering Volume of Integration

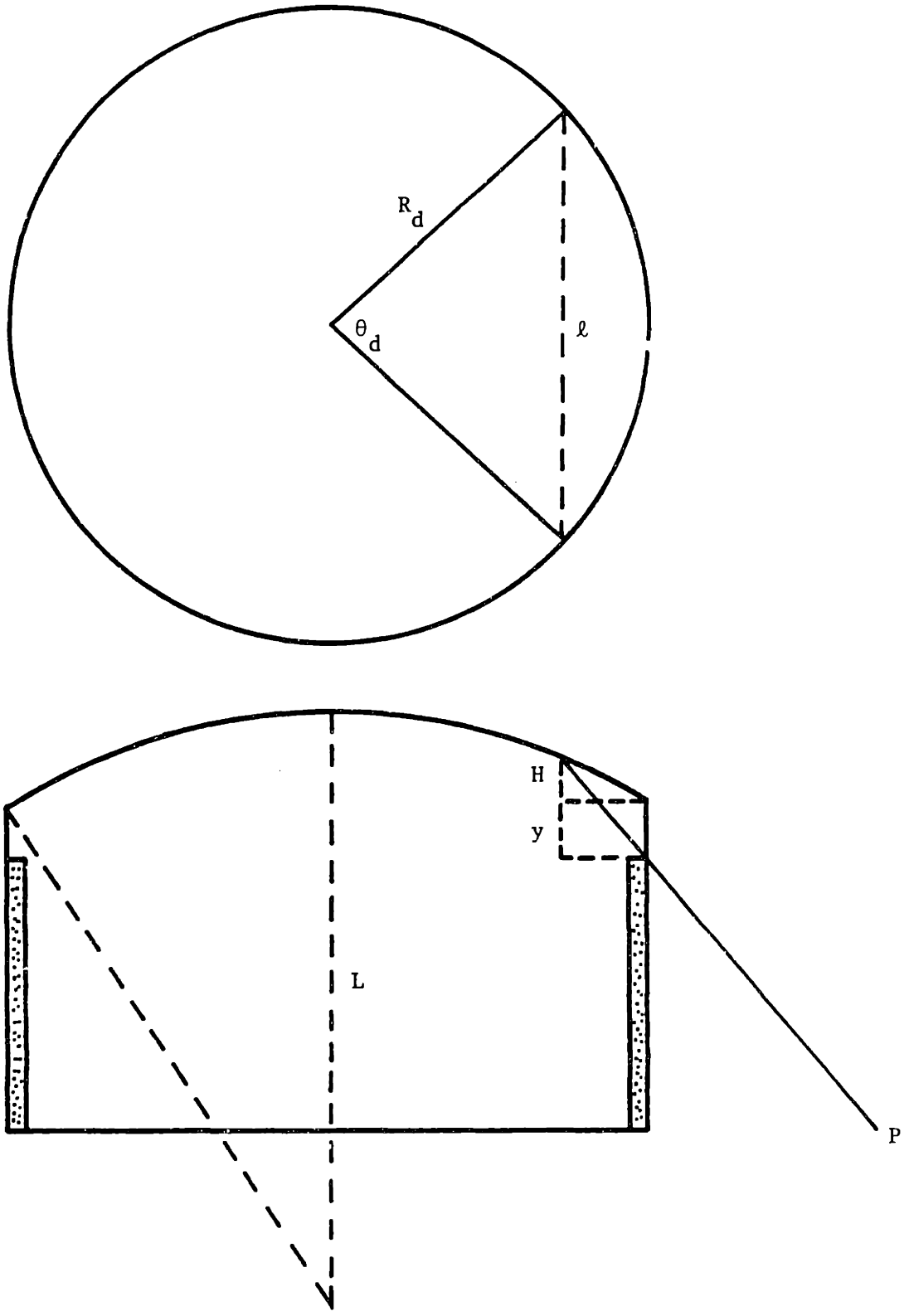

Figure 5.7

Steel Shell Volume Parameters

R_d = Dome radius = 1.13×10^3 cm

L = Dome curvature = 2.13×10^3 cm

H = Dome vertical distance (cm)

y = Side panel height = 1.68×10^2 cm

Using Eq. 5.17, the steel volumes are

$$V_{ST}(8) = 8.19 \times 10^5 \text{ cm}^3$$

$$V_{ST}(21) = 2.91 \times 10^6 \text{ cm}^3$$

5.4.2 Single Scattering Results and Comparison with the SAR

The exclusion area boundary doses were computed using Eq. 5.16 for the same four source points as used in air scattering. The geometry parameters for each point are given in Table A.12. As in air scattering, doses due to photons of E < 0.08 Mev are negligible and are not included in the total steel scattering results listed in Tables 5.4 and 5.5. The estimated total dose is 1.60×10^{-1} rads at 8 meters and 3.66×10^{-1} rads at 21 meters. The larger amount of steel visible at 21 meters causes a higher dose.

The SAR predicts much smaller steel scattering doses, namely $\sim$ 0 rads at 8 meters and $\sim 6.3 \times 10^{-2}$ rads at 21 meters.

The difference can be explained as follows. The steel scattering model used in the SAR is very similar except that the scattering from steel is assumed to be isotropic (as opposed to differential). Therefore, for a given source strength, location, and energy, the SAR method

will predict a higher dose. The difference in results lies in the source strength and location. As stated in Chapter 2, the source strength in this study is about 1.5 times that of the SAR. The difference in location is that the SAR used a single source point, located in the center the shadow shield. The effect of this is illustrated by the following dose equations for energy E = 0.8 Mev and a distance of 21 meters in which the source strength has been left as S.

From the SAR, the dose is

$$\text{Dose} = 1.81 \times 10^{-15} \text{ S rads.}$$

In this study, the doses are:

Upper Containment Dose = 3.45×10^{-15} S

Lower Containment,

Point 1 Dose = 9.15×10^{-16} S

Point 2 Dose = 3.60×10^{-16} S

Point 3 Dose = 1.92×10^{-16} S

The SAR source point corresponds to point 2 in the lower containment. As seen, the SAR method will yield a higher dose. But as the source point moves up the containment, the dose increases. This is to be expected, due to the increase in forward scattering and the decrease in scattering distance. The dose from the upper containment is almost 10 times that of point 2. This sensitivity to location combined with the higher source strength results in higher doses than the SAR.

TABLE 5.4

Steel Scattering Doses by Source Point

Source Point	Dose (Rads) 8m	21m
S_u	1.07×10^{-1}	2.81×10^{-1}
S_1	2.92×10^{-2}	5.27×10^{-2}
S_2	1.50×10^{-2}	2.09×10^{-2}
S_3	9.18×10^{-3}	1.13×10^{-2}

TABLE 5.5

Total Steel Scattering Doses by Gamma Energy

Gamma Energy E (Mev)	Dose (Rads) 8m	21m
0.08	4.13×10^{-4}	6.82×10^{-4}
0.10	1.39×10^{-6}	2.28×10^{-6}
0.15	4.01×10^{-3}	6.64×10^{-3}
0.20	7.45×10^{-3}	1.25×10^{-2}
0.30	1.25×10^{-2}	2.19×10^{-2}
0.40	1.63×10^{-2}	2.97×10^{-2}
0.50	1.35×10^{-2}	2.57×10^{-2}
0.60	1.24×10^{-2}	2.44×10^{-2}
0.80	3.35×10^{-2}	7.13×10^{-2}
1.0	8.78×10^{-3}	1.99×10^{-2}
1.5	1.27×10^{-2}	3.40×10^{-2}
2.0	3.50×10^{-2}	1.06×10^{-1}
3.0	3.69×10^{-3}	1.37×10^{-2}
4.0	3.62×10^{-5}	1.42×10^{-4}
Total	1.60×10^{-1}	3.66×10^{-1}

5.4.3 Steel Double Scattering

The importance of double scattering in steel can be evaluated as follows.

As seen in Fig. 5.8 the photons which impinge on the dome between points A and B can only arrive at P due to a second scatter between points B and C. To be conservative it is assumed that all the second scatters occur at point C as this increases the dose at P due to preferential forward scattering. The dose at point C due to scatters between A and B can be computed using the single scattering equation as before. The dose which scatters from C to P is determined by multiplying by the factor

$$\frac{N_{ST} V'_{ST}}{x_2^2} \quad \frac{d\sigma_s}{d\Omega}(\theta')$$

where V'_{ST} = Volume of steel between B and C.

θ' = Second scattering angle = $\phi_2 - \phi_n$

the resulting two scatter dose is

$$\text{Dose} = \frac{1.15\text{x}10^{-4} S N_{ST}^2 V_{ST} V'_{ST} \bar{E\mu}_a e^{-b}}{4\pi r_1^2 r_2^2 x_2^2 (\psi_2 - \psi_1)(\phi_2 - \phi_1)} \sum_{\psi=\psi_1}^{\psi_2} \Delta\psi \left[\int_{\phi_1}^{\phi_2} \frac{d\sigma_s}{d\Omega}(\theta) d\phi \frac{d\sigma_s}{d\Omega}(\theta') \right] \text{ rads} \tag{5.18}$$

The large brackets are used to indicate that during the numerical integration for each value of ϕ_n both $\frac{d\sigma_s}{d\Omega}(\theta)$

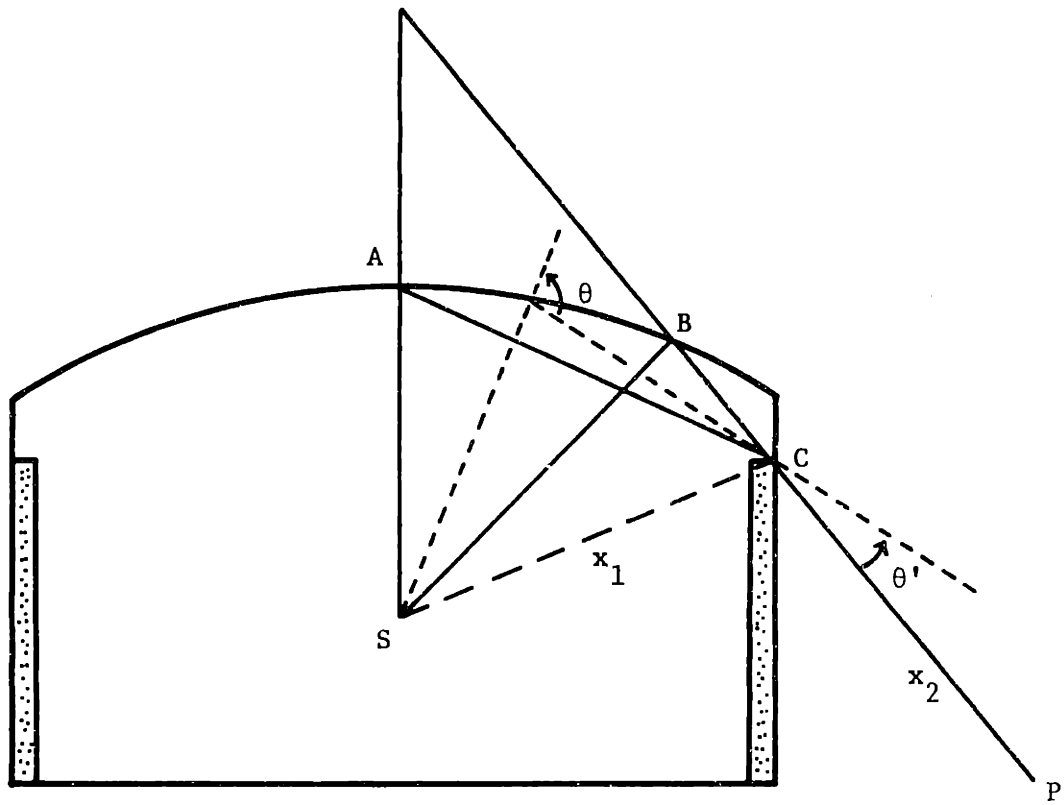

Figure 5.8
Steel Double Scattering Geometry

and $\frac{d\sigma_s}{d\Omega}(\theta')$ are evaluated and their product determined.

The effect of double scattering has been estimated by evaluating Eq. 5.18 for the three energies (E = 0.4, 0.8, and 2.0 Mev) which contribute the most to the total steel dose and the same four source points. The results indicate the total steel scattering dose results should be increased by a factor of 1.20 at 8 meters and by 1.02 at 21 meters. The adjusted doses are 1.92×10^{-1} rads at 8 meters and 3.73×10^{-1} rads at 21 meters.

The behavior of the steel scattering dose past 21 meters has been investigated by tracking the behavior of the dose due to the same three energies and assuming that the contribution of double scattering past 21 meters is negligible.

The results, shown in Fig. 5.9, indicate that the maximum steel scattering dose is $\sim 3.80 \times 10^{-1}$ rads at a distance of ~ 22 meters.

5.5 Summary

The differential scattering model developed in this section and applied to single scattering in air and single and double scattering in steel predicts an estimated 2 hour dose at the exclusion area boundaries of 3.06×10^{-1} rads at the back fence and 5.20×10^{-1} rads at the Albany St. fence. The estimated behavior of the total scattering dose is shown in Fig. 5.9.

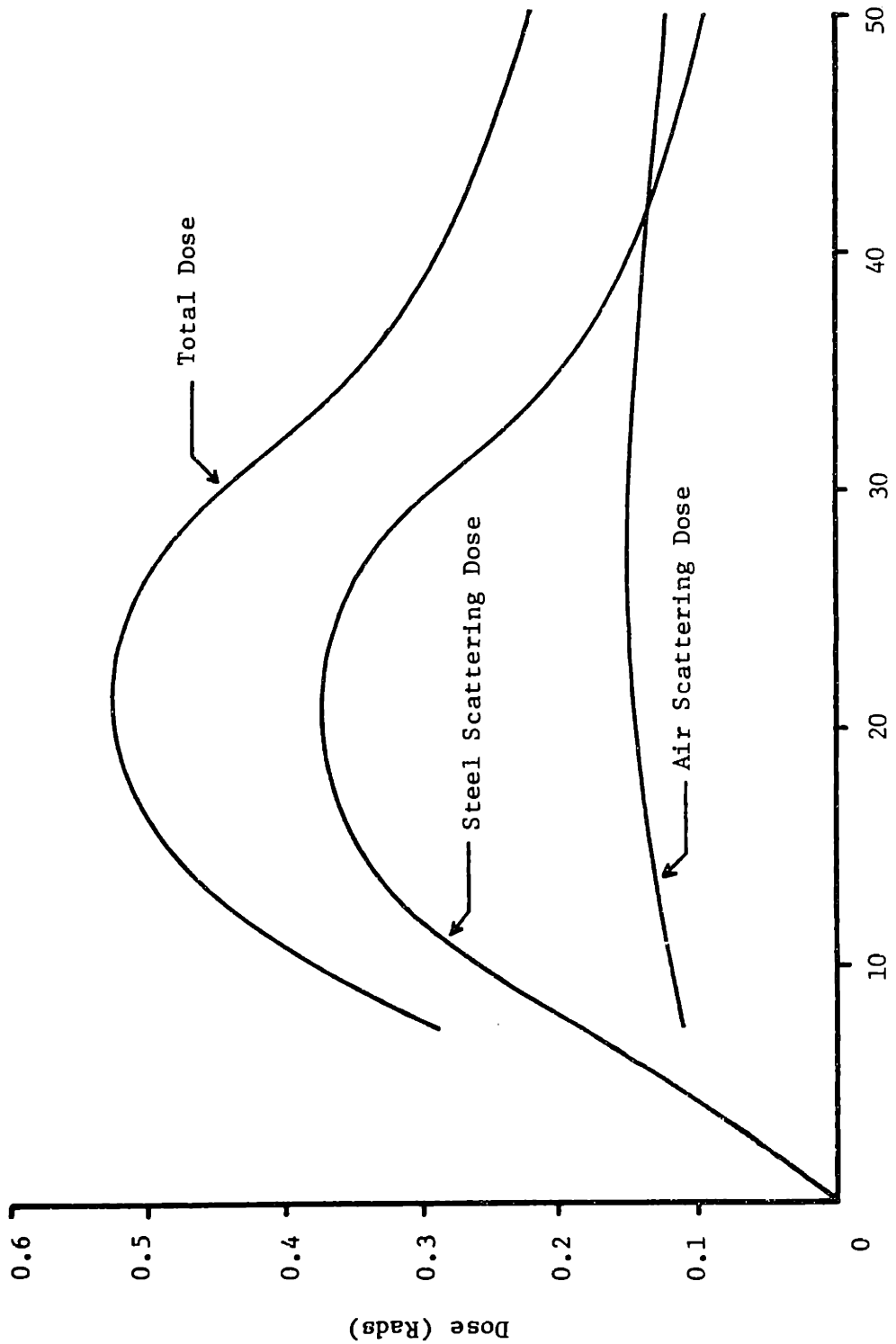

Figure 5.9 Scattering Doses

CHAPTER 6

RADIATION PENETRATION THROUGH THE TRUCK LOCK

6.1 General

The integrity of the shadow shield is broken by a number of penetrations for piping, cables and so on, the majority of which are small. The larger penetrations; the truck and personnel locks, the neutron window and the hot plug storage area; are shielded by additional concrete walls or earth [1]. The largest penetration is the truck lock, and since it is shielded by concrete only on the sides, the possibility exists that gamma radiation could stream out of the lock and reach the boundary fence by either reflection off the opposite concrete wall or scattering through the steel door (see Fig. 6.1). The exclusion area dose due to these effects will be determined in the following sections.

6.2 Truck Lock Description

As shown in Figs. 6.1 and 6.2, the truck lock is a rectangular steel tube 8 meters long closed at both ends by pneumatically sealed doors 3 meters wide and 4 meters high. Each door consists of a steel framework covered on both sides by 0.6 cm thick steel plates. The inner door is aligned just inside the containment shadow shield. The two sides of the lock are shielded by concrete walls 0.5 meters

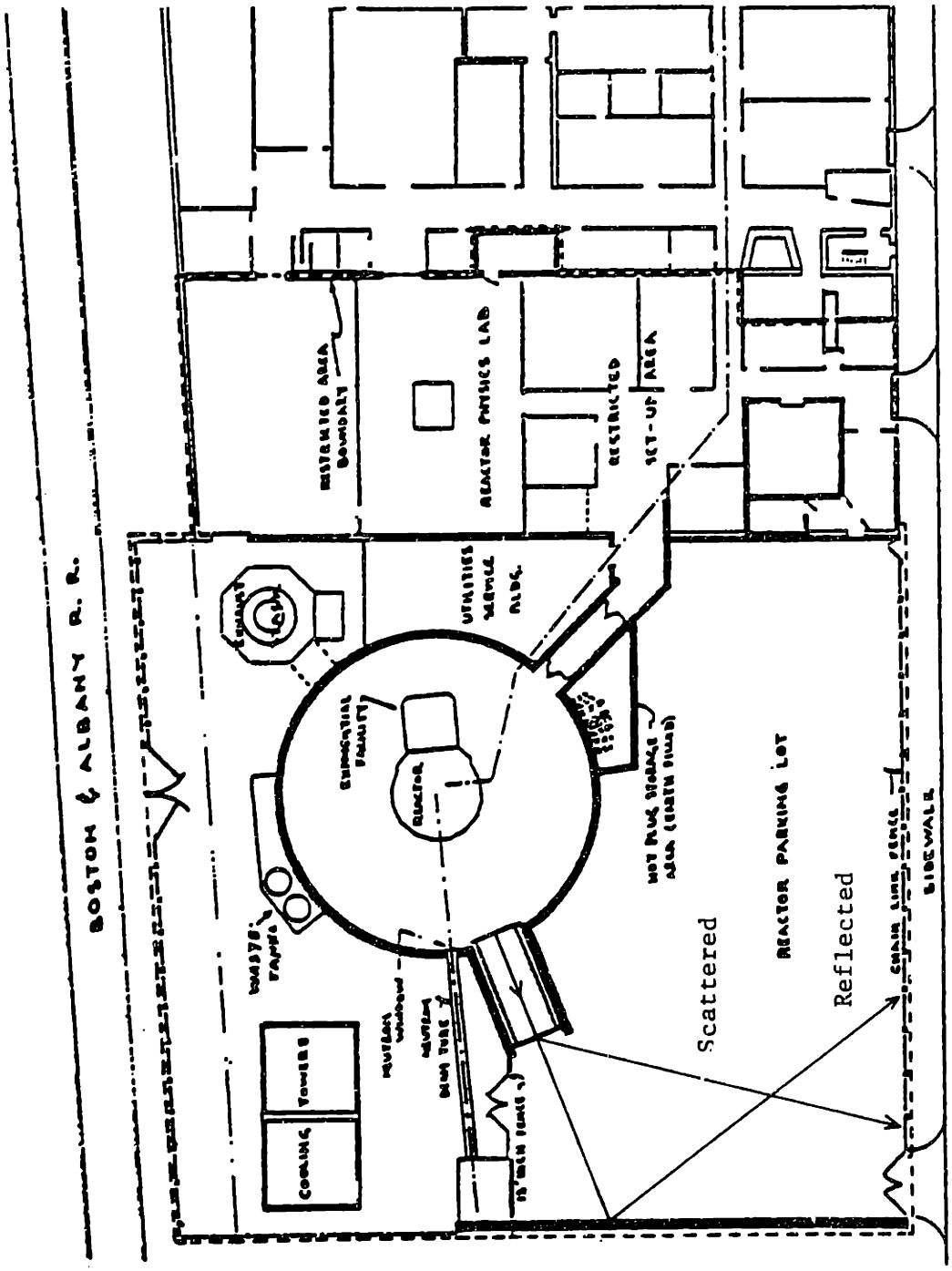

Figure 6.1 Truck Lock Radiation Release Pathways

thick while the front and top are unshielded [1].

6.3 Truck Lock Source Term

To facilitate subsequent calculations, the radiation reaching the lock will be treated as a point source located at the center of the inner surface of the inner door.

The amount of radiation reaching the door can be estimated by using the same four containment source points as in Chapter 5. If each point emits isotropically then the number of photons/sec at the door is (see Fig. 6.2)

$$S_T = \left[\frac{S_u}{4\pi r_u^2} + \frac{S_1}{4\pi r_1^2} + \frac{S_2}{4\pi r_2^2} + \frac{S_3}{4\pi r_3^2} \right] A_T \text{ photons/sec} \qquad (6.1)$$

where S_T = Truck lock source strength (photons/sec)

A_T = Area of the truck lock door (cm^2)

As before, $S_u = 0.3\ S_c$

and $$S_1 = S_2 = S_3 = \frac{S_\ell}{3} = \frac{0.7\ S_c}{3}$$

where $S_c = S_u + S_\ell$ = Total containment source strength (photons/sec)

The source distances are:

$r_u = 1.36 \times 10^3$ cm $\qquad$ $r_2 = 1.07 \times 10^3$ cm

$r_1 = 1.15 \times 10^3$ cm $\qquad$ $r_3 = 1.09 \times 10^3$ cm

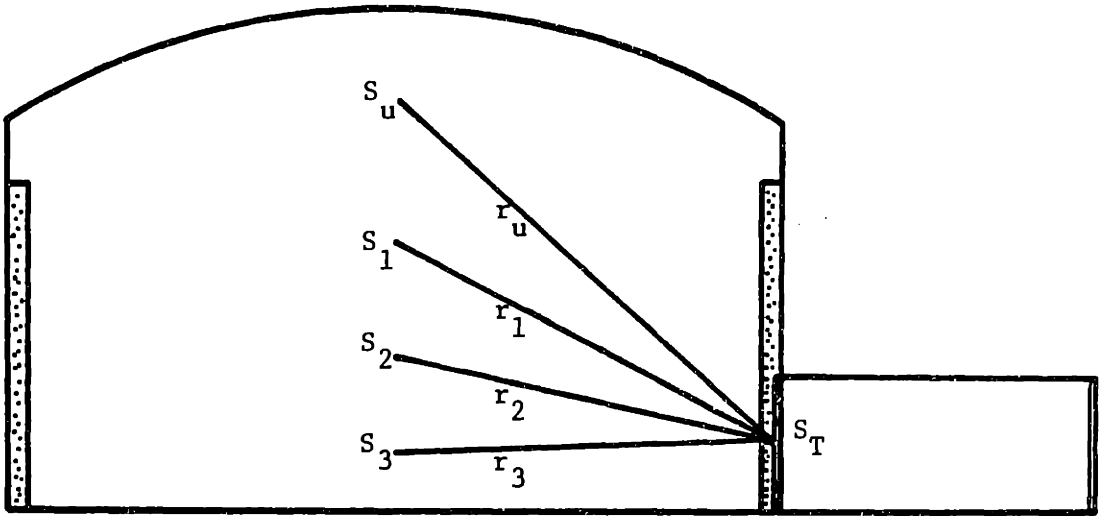

Figure 6.2

Truck Lock Source Term Geometry

The truck lock area is

$$A_T = 1.2 \times 10^5 \text{ cm}^3$$

Substituting, the final truck lock source term is

$$S_T = 7.12 \times 10^{-3} S_c \text{ photons/sec} \qquad (6.2)$$

where the values of S_c are given in Table 5.1.

Finally, it is conservatively assumed that all photons reaching the door travel through it, making the truck lock point source isotropic in the forward direction.

One could argue that the treatment of the containment source as four points along the center axis does not give full weight to those fission products suspended just inside the door. However, it is felt that this treatment is still conservative since the entire containment source term is used, while in reality a number of photons are blocked from reaching the door by the reactor vessel. In addition, no energy degredation is considered, although the majority of the gammas would have to make a change of direction in order to reach the outer truck lock door.

6.4 Concrete Scattered Dose

6.4.1 Unattenuated Flux

The flux on the concrete wall opposite the truck lock is determined from the point source relationship [30]

$$\phi_\gamma = \frac{BS_T}{2\pi x^2} \; e^{-\Sigma\mu T} \qquad \text{photons/cm}^2\text{-sec} \qquad (6.3)$$

where B = Point build up factor for steel

$\Sigma\mu T$ = Number of mean free paths through the two doors

x = Distance to the wall (cm)

The above equation neglects build up and attenuation in the air. The 2 in the denominator (instead of 4) reflects the conservative assumption that the source is isotropic in the forward direction.

The dose at the wall is then

$$\text{Dose} = \frac{1.15 \times 10^{-4} \; BS_T E\mu_a}{2\pi x^2} \; e^{-\Sigma\mu T} \qquad \text{rads} \qquad (6.4)$$

The minimum thickness of steel through both doors is 2.54 cm (1 in) and the distance to the wall is 2.21×10^3 cm. From Eq. 6.4 the estimated dose at the wall opposite the lock as shown in Table 6.1 is 1.09×10^{-1} rads. For comparison, a similar calculation for the inside of the door estimates the total two hour dose to be 44.9 rads.

6.4.2 Concrete Albedo

The differential dose received at some point A due to back scattering from a plane surface dA as shown in Fig. 6.3 is [27]

$$dD = \frac{D_0(\theta_0) \cdot \cos\theta_0 \cdot dA \cdot A_{JX}(E, \theta_0, \theta_r)}{r^2} \qquad (6.5)$$

TABLE 6.1

Direct Dose at the Concrete Wall

Gamma Energy E (Mev)	Build-up Factor B	$\Sigma\mu T$	Dose (Rads)
0.10	4.0	6.63	1.54×10^{-8}
0.15	3.9	3.58	3.44×10^{-4}
0.20	3.8	2.72	1.24×10^{-3}
0.30	3.3	2.09	3.19×10^{-3}
0.40	3.1	1.80	5.59×10^{-3}
0.50	2.67	1.62	5.22×10^{-3}
0.60	2.47	1.48	5.59×10^{-3}
0.80	2.22	1.30	1.89×10^{-2}
1.0	2.04	1.17	5.98×10^{-3}
1.5	1.78	0.947	1.23×10^{-2}
2.0	1.63	0.828	4.39×10^{-2}
3.0	1.39	0.701	6.48×10^{-3}
4.0	1.29	0.645	8.76×10^{-5}
		Total	1.09×10^{-1}

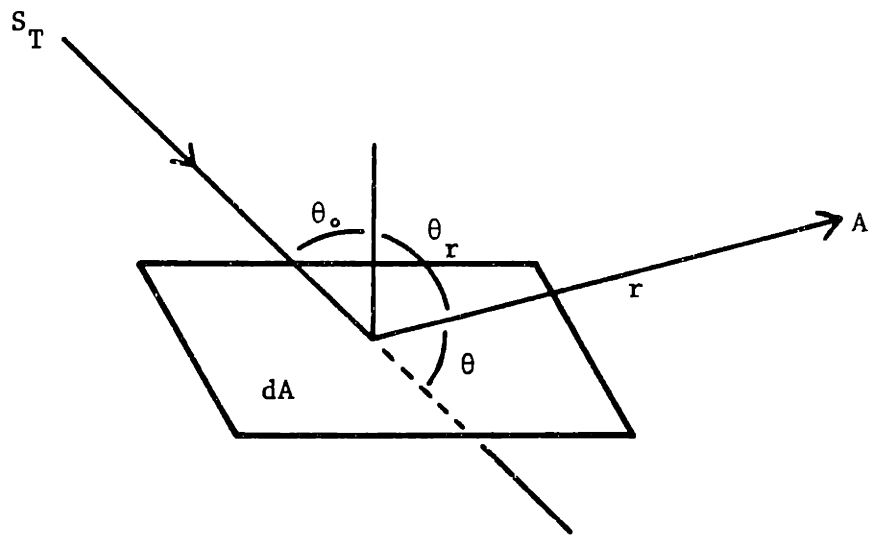

Figure 6.3
Albedo Geometry

where $D_0(\theta_0)$ = Incident dose at incoming angle θ_0 (rads)

$A_{JX}(E, \theta_0, \theta_r)$ = Differential Exposure Albedo

θ_r = Angle of reflection (radians)

r = Distance from dA to point A (cm)

The differential exposure albedo can be found from [27]

$$A_{JX} = \frac{C_1 \cdot d\sigma_s/d\Omega\ (\theta,E) \cdot 10^{26} + C_2}{1 + \cos\theta_0\ \sec\theta_r} \tag{6.6}$$

where C_1 , C_2 = Energy and material dependent constants.

The total dose is determined by integrating over the area of reflection. The area of the wall, A_W, in view of the source is limited by the truck lock side walls as shown in Fig. 6.4. Integration of Eq. 6.5 is difficult since the angles and distances are different for each point on the wall. As an approximation, the albedo at the center of the scattering area can be determined and used for the entire area. By trial and error the point along the northern boundary was found which receives the maximum dose. This is point P_1 in Fig. 6.4 and the scattering parameters are:

θ_0 = 0.384 radians

θ_r = 1.117 radians

θ = 1.641 radians

r = 2.17×10^3 cm

The area of A_W of the wall in view of the source is 4.18×10^5 cm^2. Substituting in Eq. 6.5, the dose is

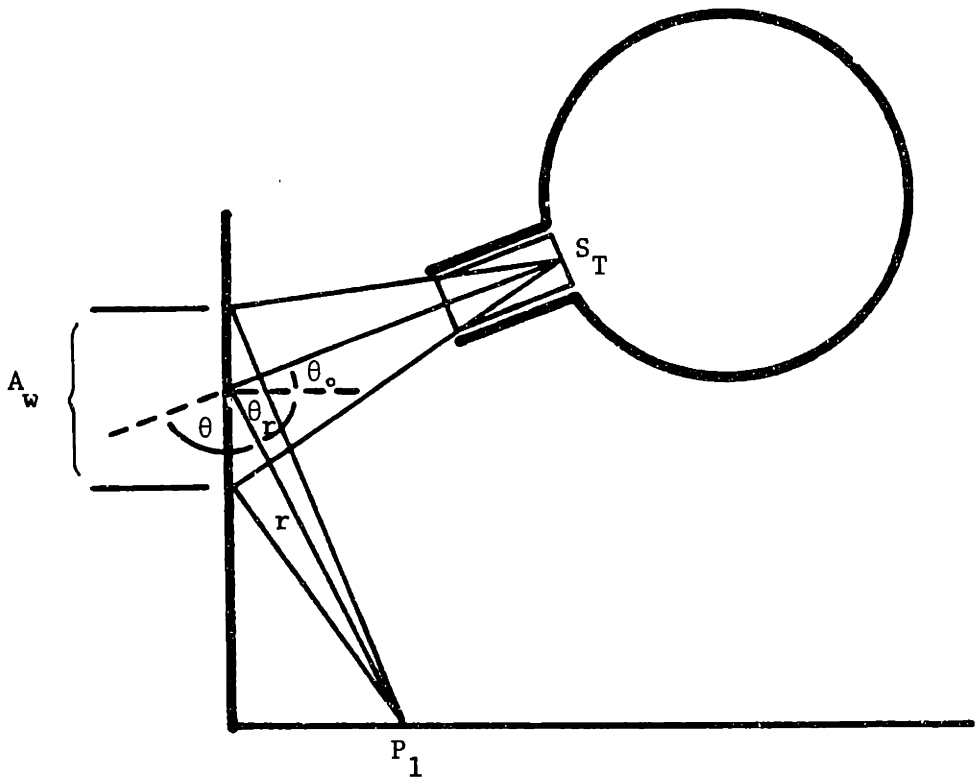

Figure 6.4

Concrete Wall Albedo Geometry

$$D = 8.23 \times 10^{-2} \, D_0 A_{JX} \quad \text{rads} \tag{6.7}$$

Using the values of C_1 and C_2 for concrete given in [27] a graph of A_{JX} vs. E was constructed. The resulting values of A_{JX} and the two-hour doses are shown in Table 6.2. The estimated maximum dose at the exclusion area boundary due to backscattering from the concrete wall is 8.25×10^{-5} rads.

6.5 Steel Door Scattered Dose

The second path along which gamma radiation can reach the exclusion area through the truck lock is by scattering in the outer steel door. The steel scattering equation developed in Chapter 5 can be applied directly to the geometry shown in Fig. 6.5. The dose at P_2 is then

$$D = \frac{1.15 \times 10^{-4} \, S_T N_{ST} V_{ST} E\bar{\mu}_a \, e^{-\Sigma\mu T}}{2\pi r_1^2 \, r_2^2 \, (\psi_2 - \psi_1)(\phi_2 - \phi_1)} \sum_{\psi = \psi_1}^{\psi_2} \Delta\psi \int_{\phi_1}^{\phi_2} \frac{d\sigma_s}{d\Omega}(\theta) \, d\phi \quad \text{rads} \tag{6.8}$$

where $S_T = 7.12 \times 10^{-3} \, S_c$ photons/sec

$N_{ST} = 2.19 \times 10^{24}$ elec/cm^3

The location along the boundary which receives the maximum dose is point P_2 with the parameters:

TABLE 6.2

Concrete Albedo Dose

Gamma Energy E (Mev)	Exposure Albedo A_{JX}	Dose (Rads)
0.10	3.9×10^{-2}	4.94×10^{-11}
0.15	3.05×10^{-2}	8.64×10^{-7}
0.20	2.55×10^{-2}	2.60×10^{-6}
0.30	2.0×10^{-2}	5.26×10^{-6}
0.40	1.65×10^{-2}	7.61×10^{-6}
0.50	1.45×10^{-2}	6.22×10^{-6}
0.60	1.30×10^{-2}	5.98×10^{-6}
0.80	1.08×10^{-2}	1.68×10^{-5}
1.0	9.4×10^{-3}	4.63×10^{-6}
1.5	7.4×10^{-3}	7.50×10^{-6}
2.0	6.2×10^{-3}	2.24×10^{-5}
3.0	4.8×10^{-3}	2.56×10^{-6}
4.0	4.1×10^{-3}	2.96×10^{-8}
	Total	8.25×10^{-5}

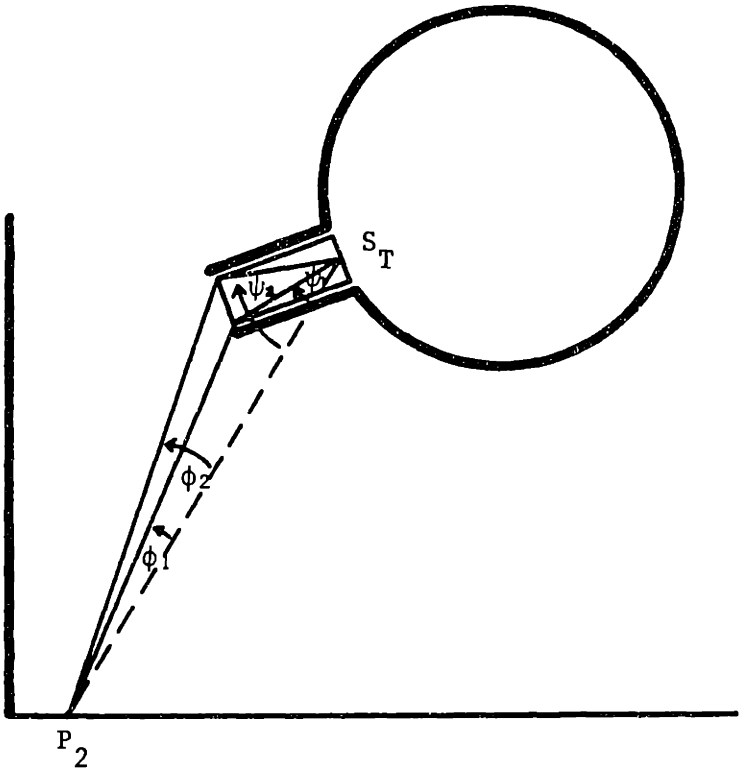

Figure 6.5

Steel Door Scattering Geometry

$r_1 = 9.14 \times 10^2$ cm

$r_2 = 2.82 \times 10^3$ cm

$\phi_1 = 0.140$ radians $\qquad \psi_1 = 0.436$ radians

$\phi_2 = 0.209$ radians $\qquad \psi_2 = 0.768$ radians

The volume of steel in one door was determined from the dimensions and material list in the original reactor housing plans [36] to be 2.01×10^5 cm^3. As in the direct dose, an attenuation of 1 inch of steel was used, attenuation and build up in the air have been neglected, and the factor of 2 in the denominator reflects the forward direction source.

As shown in Table 6.3, the maximum estimated dose due to steel scattering is 3.55×10^{-4} rads.

6.6 Air Scattered Dose

Using the techniques of Chapter 5 the effect of air scattering from the truck lock to the exclusion area was investigated and found to be less than 1×10^{-5} rads. This is primarily due to the limited scattering angles as a result of the concrete side walls along the truck lock.

6.7 Conclusions

The concrete and steel scattering results show that the estimated radiation release from the reactor truck lock during the two-hour period does not add significantly to the total dose at the exclusion area boundary from the other modes of release.

TABLE 6.3

Steel Door Scattering Dose

Gamma Energy E (Mev)	Dose (Rads)
0.10	7.26×10^{-11}
0.15	1.55×10^{-6}
0.20	5.18×10^{-6}
0.30	1.38×10^{-5}
0.40	2.28×10^{-5}
0.50	2.20×10^{-5}
0.60	2.28×10^{-5}
0.80	7.28×10^{-5}
1.0	2.16×10^{-5}
1.5	3.86×10^{-5}
2.0	1.19×10^{-4}
3.0	1.43×10^{-5}
4.0	1.53×10^{-7}
Total	3.55×10^{-4}

CHAPTER 7

SUMMARY, RESULTS AND CONCLUSIONS

7.1 Summary

7.1.1 Introduction

The purpose of this thesis was to determine a conservative estimate of the maximum amount of radiation an individual located at the exclusion area boundary of the MIT reactor would receive during the first two hours of the reactor's Design Basis Accident (DBA).

The DBA for the MITR is postulated to be a coolant flow blockage in one of the flat plate fuel elements resulting in complete melting of four U-Al_x fuel plates. The radiation release from this event has been previously examined in the MIT Reactor Safety Analysis Report (SAR), published in 1970.

The present study offers a significant improvement over the SAR in the following areas:

1) The fission product inventory has been expanded to include other important isotopes, such as those of Tellurium.

2) The release fractions have been updated to more realistic values based on the expected physical processes specific to the MITR.

3) The leakage release has been based on historical meteorological data and includes gamma and beta whole-body doses.

4) The scattering model of gamma radiation, particularly from air, has been greatly improved and is no longer grossly over-conservative.

5) The effect of penetrations have been examined for the first time.

7.1.2 Development of the Containment Source Term

The fission product isotopes of interest include the noble gases, iodine and any less volatile element which can be expected to yield a measurable whole-body or thyroid dose. The fission product inventory in the fuel at the time of the accident is assumed to be equal to the maximum equilibrium value after an essentially indefinite period of irradiation at a power level of 5 MW. The saturation activities of the fission products can be determined using analytical production and decay relationships or numerical results such as those by Blomeke and Todd [8]. Once the total core fission product inventory is known, the fraction released along each portion of the path to the containment must be determined.

Assuming a radial peaking factor of 1.45 the fraction of the core fission product inventory contained in the four melted fuel plates is 1.5%

Assuming typical End-of-Cycle fuel conditions, studies of U-Al melting [6, 12, 13, 14] show that the estimated fractions of the fission products in the melted fuel released to the primary coolant are:

100 % of the noble gases (Kr, Xe)
100 % of the halogens (I, Br)
70% of the Tellurium
30% of the alkali metals (Cs, Rb)
1% of the remaining fission products

Release from the coolant water is dependent on the degree of plateout within the primary system and absorption in the coolant. Recent studies [5, 16, 19] indicate that iodine will be retained in the coolant in the form of CsI to a much greater degree than previously expected, with retention as high as 99.9%. For the present, however, the following conservative (especially with respect to iodine) values will be used:

100% of the noble gases
10% of all other isotopes.

Natural depletion in the containment atmosphere is dependent on deposition velocities. Based on the findings in WASH-1400 [15], the fraction of the released fission products which remain airborne are expected to be:

100% of the noble gases
30% of the halogens
90% of the remaining fission products.

The resulting overall airborne release fractions compare favorably with those of historical accidents, while still being conservative with respect to the latest source term revision estimates [19].

7.1.3 Atmospheric Release

It is anticipated that fission products in the containment atmosphere may leak out of the containment through small cracks and crevices. It is conservatively assumed that this occurs at the maximum leakage rate of 1% of the building volume per psi over-pressure per day and that the containment pressure is at the maximum value of 2 psi over atmospheric.

Once released, the concentration of fission products in the air will be decreased due to atmospheric diffusion, which is modeled based on the Gaussian plume, and the building wake effect [22]. This wake effect reflects the tendency for the released particles to quickly expand to fill a volume of air on the order of the containment volume. The relative magnitude of these two effects depends on the distance downwind from the containment. In the range of the exclusion area, the wake effect is extremely dominant.

The NRC has proposed a conservative concentration equation which takes only partial credit for the wake effect [23]. Using this equation with wind data from Boston's General Logan Airport the estimated whole-body dose due to gamma and beta radiation to a person located at the minumum exclusion area distance of 8 meters is 8.12 rads and the dose to the thyroid is 36.3 rads. At the most populated edge of the exclusion area (a distance of 21 meters) the whole-body dose is 1.23 rads and that to the thyroid is 5.49 rads.

In contrast, the estimated dose taking into account the full wake

effect is 2.66 x 10^{-2} rads whole-body and 1.18 x 10^{-1} rads thyroid at any point on the exclusion area boundary. The actual dose is expected to be somewhere in between these values. Due to the conservative assumptions with respect to the building pressure and leakage rate, plus the wind tunnel effect of adjacent buildings, the lower value is deemed more likely.

7.1.4 Direct Gamma Dose

Those isotopes which do not leak from the containment will constitute a source of gamma radiation. A circular concrete shadow shield 9.6 m high and 0.61 m thick is incorporated into the containment to protect against this hazard. Above the shadow shield the gammas are attenuated only by the 0.95 cm thick steel containment shell.

From any point on the exclusion area boundary some portion of the containment volume is visible above the top of the shadow shield. This volume can be modeled as a spherical volume source shielded by a steel slab. Using available point kernel integration expressions [27] with the Taylor analytical form of the build up factor the dose at 8 meters from the containment is estimated to be 3.49 x 10^{-3} rads while that at a distance of 21 meters is 2.71 x 10^{-2} rads.

That portion of the containment volume located behind the shadow shield can be modeled as a right circular cylinder shielded by a two layer concrete/steel slab. Point kernel results for this shape have been determined by numerical methods [27], and using the build up

factor for concrete, yield an estimated two-hour dose of 4.33×10^{-2} at 8 meters and 2.05×10^{-2} at 21 meters.

The maximum total direct dose occurs beyond the exclusion area at a distance of $\sim$ 38 meters with a value of $\sim 7.2 \times 10^{-2}$ rads.

7.1.5 Scattered Gamma Dose

It is also possible for gamma radiation to reach the exclusion area boundaries by escaping over the top of the shadow shield and scattering back down from interactions with the air or the steel containment dome.

Separate scattering models for air and steel dome scattering were developed based on the Klein-Nishina differential scattering cross-section which take into account the scattering angle restrictions due to the presence of the shadow shield. The volumetric containment source was approximated as four point sources located along the central axis of the containment. Attenuation in the steel shell and photon energy degradation due to scattering were also considered.

The resulting expression was numerically integrated over the range of scattering angles to yield an estimated air scattering dose of 1.14×10^{-1} rads at 8 meters and 1.47×10^{-1} rads at 21 meters. Including double-scattering, the steel dose is expected to be 1.92×10^{-1} rads at 8 meters and 3.73×10^{-1} rads at a distance of

21 meters. The maximum total scattering dose occurs at $\sim$ 23 meters and is believed to be $\sim 5.3 \times 10^{-1}$ rads.

7.1.6 Radiation Penetration through the Truck Lock

The effect of penetrations in the shadow shield was investigated by calculating the dose at the exclusion area due to travel through the largest penetration, the truck airlock. There are three pathways to the exclusion area boundary; direct radiation backscattering from the opposite concrete wall, scattered radiation from the outer steel door, and scattered radiation from the air.

The direct radiation passing through the doors was evaluated using a standard attenuation relation with a steel build up factor. Using an analytical albedo model and for the given geometry the maximum boundary dose is expected to be 8.25×10^{-5} rads.

Steel and air scattering were evaluated using the previously developed scattering model to yield a maximum steel door scattering dose of 3.55×10^{-4} rads and an air scattering dose of less than 1×10^{-5} rads.

7.2 Results

A summary of the estimated doses due to all modes of radiation release plus the resulting total release are shown in Table 7.1 and Fig. 7.1. The "exact" (full wake) values of the leakage doses have

been used since, as previously mentioned, they are believed to be more realistic. In fact, they can be considered conservative with respect to a realistic building pressure and leakage points distributed around the containment.

The conservative assumptions and calculational models used in this investigation give an estimated maximum dose to an individual located at the exclusion area boundary during the first two hours of the MITR design basis accident of 5.95×10^{-1} rads whole-body and 1.18×10^{-1} rads to the thyroid. This dose is the integrated total value during the first two hours following release. Fission product decay and aerosol deposition will greatly reduce the dose rate after the first two hours. This maximum value is estimated to occur at a distance of 21 through 23 meters from the containment wall, corresponding to the exclusion area boundary along Albany St.

7.3 Conclusions

According to 10 CFR 100 [9] the maximum calculated dose at any point along the exclusion area boundary at the end of the first two hours following the onset of fission product release from a design basis accident must be less than 25 rads to the whole-body and 300 rads to the thyroid. Based on the above results it can be concluded that the present containment design and exclusion area dimensions for the MIT Reactor are well within the regulatory standards.

TABLE 7.1

Total Dose Results

Component of the Dose	Dose (Rads) 8m	21m
Whole-body:		
Containment Leakage	2.66×10^{-2}	2.66×10^{-2}
Steel Dome Penetration	3.49×10^{-3}	2.71×10^{-2}
Shadow Shield Penetration	4.33×10^{-2}	2.05×10^{-2}
Air Scattering	1.14×10^{-1}	1.47×10^{-1}
Steel Scattering	1.92×10^{-1}	3.73×10^{-1}
Total	3.79×10^{-1}	5.95×10^{-1}
Thyroid:		
Containment Leakage	1.18×10^{-1}	1.18×10^{-1}

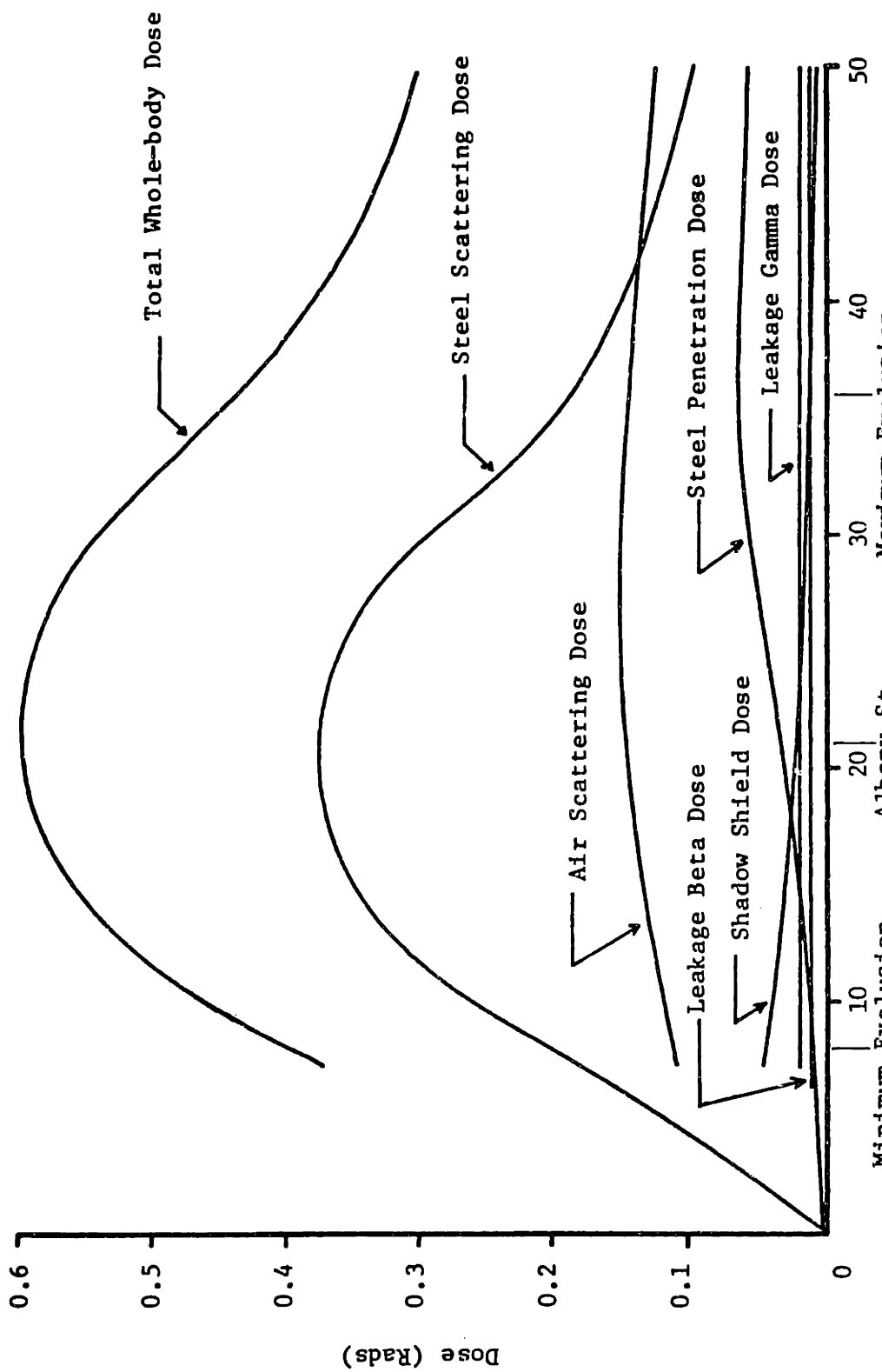

Figure 7.1 Total Two Hour Whole-body Dose Results

7.4 Suggestions for Future Work

There are two ways in which the results of this study could be improved upon with very little modification of the calculational procedure. They are: improved release fractions and additional scattering source points.

During the period in which this report was prepared a number of independent studies were begun by various organizations with the purpose of improving on the various fission product release fractions reported in WASH-1400. It is expected that the results of these studies will show that actual release fractions are significantly lower than those used in this study.

Although the scattering model developed in Chapter 5 has resulted in a lower scattering dose than the SAR, it is still the largest component of the total dose. As shown in Sec. 5.4.2, the location of the gamma point source within the containment has a considerable effect on the magnitude of the dose at the boundary. For simplicity, only four source points were used in this study, with all four located along the central axis of the containment. Obviously, greater accuracy could be obtained by the use of additional source points throughout the containment. In addition this would allow the shielding and scattering angle effects of the reactor to be included.

One area which was not addressed in this thesis, but which would be of interest is the time-dependent dose rate at the exclusion area

boundary. Assuming an instantaneous release of fission products to the containment atmosphere; decay, deposition, and leakage rates could be used to determine a time-dependent containment source term and a time-dependent exclusion area concentration of fission products. These could be combined with the dose models developed in this work to yield time-dependent doses.

NOMENCLATURE

a	Parameter of the direct dose volume V_1
A	Coefficient of the Taylor build up factor expression
A_{JX}	Differential exposure albedo
A_s	Containment surface area (cm^2)
A_t	Atomic weight (g/g-atom)
A_T	Area of the truck lock door (cm^2)
A_W	Area of the concrete albedo wall (cm^2)
A_{xs}	Containment cross-sectional area (m^2)
b	Shield thickness in mean free paths
b_1	Steel dome thickness in mean free paths
b_2	Shadow shield thickness in mean free paths
B	Build up factor
B_r	Breathing rate (m^3/sec)
c	Shape factor
C_D	Flux to dose conversion factor (rads per photon/cm^2-s)
C_o	Initial fission product concentration in containment (Ci/m^3)
$C(t)$	Fission product concentration in containment at time t(Ci/m^3)
C_T	Thyroid dose conversion factor (rads per Ci inhaled)
C_y	Sutton lateral diffusion parameter
C_z	Sutton vertical diffusion parameter

NOMENCLATURE (Cont.)

C_1	Albedo constant
C_2	Albedo constant
C_γ	Photon dose conversion factor (rads per Ci-sec/m^3)
d	Parameter of the direct dose volume V_1
d'	Parameter of the angle ω (cm)
D	Dose (rads)
D_o	Albedo incident dose (rads)
$_TD$	Thyroid dose (rads)
$_\beta D$	Beta dose (rads)
$_\beta D'$	Beta dose rate (rads/sec)
$_\gamma D$	Gamma dose (rads)
$_\gamma D'$	Gamma dose rate (rads/sec)
e	Parameter of the direct dose volume V_1
E	Photon energy (Mev)
E'	Scattered photon energy (Mev)
E_1	Special exponential integral function
$\bar{E}_\beta$	Average beta energy per disintegration (Mev/dis)
$\bar{E}_\gamma$	Average gamma energy per disintegration (Mev/dis)
F_c	Fraction of fission products released from the primary system remaining airborne in the containment atmosphere
F_f	Fraction of fission products released from the melted fuel
F_p	Fraction of fission products released from the primary system

NOMENCLATURE (Cont.)

F_R	Overall fraction of the total core fission product inventory remaining airborne in the containment atmosphere
F_s	Fraction of the total saturated core fission product inventory present in the melted fuel.
G	Cylindrical source geometry attenuation function
h	Height (cm)
h'	Parameter of the angle ω (cm)
H	Dimension of the steel dome (cm)
i	Isotope i
k	Parameter of the G function
ℓ	Dome segment length (cm)
L	Dome curvature (cm)
M	Meander correction factor
n	Sutton parameter associated with stability
N	Electron density in air (elec/cm^3)
N_i	Number of nuclei of isotope i
N_{25}°	Initial number of U^{235} atoms in fuel
N_s	Saturation number of nuclei
N_{ST}	Electron density in steel (elec/cm^3)

NOMENCLATURE (Cont.)

p	Parameter of the G function
P	Reactor power (Mw)
Q	Fission product release rate from the containment (Ci/sec)
$Q_c(t)$	Activity in the containment at time t (Ci)
Q_{c_T}	Total decay emissions in the containment (dis)
Q_s	Fission product saturation activity (Ci)
Q(t)	Fission product release rate at time t (Ci/sec)
Q_T	Total fission product release (Ci)
$Q_T(x)$	Total fission product release at distance x (Ci)
r	Distance (cm)
r_e	Classical radius of the electron (cm)
R	Radius (cm)
R'	Parameter of the angle ω (cm)
R_d	Radius of the steel dome (cm)
R_1	Radius associated with V_1 (cm)
R_2	Radius associated with V_2 (cm)
s	Shadow shield penetration distance parameter (m)
S	Gamma point source strength (photons/sec)
S_A	Surface source strength (photons/cm^2-sec)
S_c	Containment total source strength (photons/sec)
S_ℓ	Lower containment source strength (photons/sec)

NOMENCLATURE (Cont.)

S_T	Truck lock source strength (photons/sec)
S_u	Upper containment source strength (photons/sec)
S_v	Volume source strength (photons/cm^3-sec)
t	Time (sec)
$t_{\frac{1}{2}}$	Half-life
T	Shield thickness (cm)
T_c	Concrete thickness (cm)
T_{ST}	Steel thickness (cm)
u	Windspeed
v_d	Deposition velocity (cm/sec)
V	Containment volume (cm^3)
V_f	Volume of the fuel (cm^3)
V_ℓ	Lower containment volume (cm^3)
V_{ST}	Steel volume (cm^3)
V'_{ST}	Volume of steel subject to second scattering (cm^3)
V_T	Total scattering volume (cm^3)
V_u	Upper containment volume (cm^3)
V_1	Direct dose steel penetration volume (cm^3)
V_2	Direct dose shadow shield penetration volume (cm^3)
x	Distance (cm)
X	Sector distance (m)

NOMENCLATURE (Cont.)

y	Dome side panel height (cm)
Y	Fission product yield (%)
z	Self-absorption distance (cm)
Z	Atomic number
α_1	Coefficient of the Taylor build up factor expression
α_2	Coefficient of the Taylor build up factor expression
δ	Parameter used in determination of the difference between two values of the E_1 function.
θ	Compton scattering angle (radians)
θ'	Steel second scattering angle (radians)
θ_d	Dome segment angle (radians)
θ_o	Albedo incident angle (radians)
θ_r	Albedo angle of reflection (radians)
θ_1	Steel penetration disk source angle (radians)
λ	Radiological decay constant (sec^{-1})
λ_L	Containment leakage rate (V/sec)
λ_R	Containment removal rate (sec^{-1})
μ	Linear attenuation coefficient (cm^{-1})

NOMENCLATURE (Cont.)

μ_a	True energy absorption coefficient in air (cm^2/g)
$\bar{\mu}_a$	Maximum air absorption coefficient in the range E to E'_{min} (cm^2/g)
μ_c	Linear attenuation coefficient for concrete (cm^{-1})
μ_s	Linear attenuation coefficient for the source medium (cm^{-1})
μ_{ST}	Linear attenuation coefficient for steel (cm^{-1})
ρ	Density (g/cm^3)
Σ_f	Macroscopic fission cross-section (cm^{-1})
σ_f	Microscopic fission cross-section (cm^2)
σ_y	Lateral Pasquill plume dispersion coefficient (m)
σ_z	Vertical Pasquill plume dispersion coefficient (m)
$\frac{d\sigma}{d\Omega}$	Klein-Nishina differential collision cross-section (cm^2/steradian)
$\frac{d\sigma_s}{d\Omega}$	Klein-Nishina differential scattering cross-section (cm^2/steradian)
ϕ	Scattering angle with respect to the detector (radians)
ϕ_0	Initial value of ϕ (air scattering) (radians)
ϕ_T	Thermal neutron flux (neutrons/cm^2-sec)
ϕ_1	Lower limit of ϕ (steel scattering) (radians)
ϕ_2	Upper limit of ϕ (steel scattering) (radians)
ϕ_γ	Photon flux (photons/cm^2-sec)

NOMENCLATURE (Cont.)

φ	Parameter of the angle ω (radians)
χ	Fission product concentration in air (Ci/m^3)
χ/Q	Relative concentration (sec/m^3)
ψ	Scattering angle with respect to the source (radians)
ψ_0	Initial value of ψ (air scattering) (radians)
ψ_1	Lower limit of ψ (steel scattering) (radians)
ψ_2	Upper limit of ψ (steel scattering) (radians)
ω	Azimuthal scattering angle (radians)

REFERENCES

1. MIT Nuclear Reactor Laboratory Staff, "Reactor Systems Manual," MITNRL-004 (Revision One), January 1982.

2. Thompson, T.J., et. al., "Final Hazards Summary Report to the Advisory Comittee on Reactor Safeguards on a Research Reactor for the Massachusetts Institute of Technology," MIT-5007, January 1956; plus Addendum, Appendices B and C, December 1957.

3. "Safety Analysis Report for the MIT Research Reactor (MITR-II)," MITNE-115, October 1970.

4. DiNunno, J.J., et al., "Calculation of Distance Factors for Power and Test Reactor Sites," TID-14844, March 1962.

5. McCauley, J.J., "A Review of the MITR-II Design Basis Accident," B.S. Thesis, Dept. of Nucl. Eng., M.I.T., May 1982.

6. Thompson, T.J. and Beckerley, J.G., (eds.), The Technology of Nuclear Reactor Safety, Vol. 2, "Reactor Materials and Engineering," MIT Press, 1973.

7. "Reactor Safety Study," WASH-1400, App. VI, "Calculations of Reactor Accident Consequences," October 1975.

8. Blomeke, J.O. and Todd, M.F., "Uranium-235 Fission-Product Production as a Function of Thermal Neutron Flux, Irradiation Time, and Decay Time," Part I, Vol. I, ORNL-2127, August 1957.

9. Code of Federal Regulations, Title 10 (Energy), Part 100,"Reactor Site Criteria," revised, January 1982.

10. USAEC Regulatory Guide 1.3, "Assumptions used for Evaluating the Potential Radiological Consequences of a Loss of Coolant Accident for Boiling Water Reactors," June 1974.

11. USAEC Regulatory Guide 1.4, "Assumptions Used for Evaluating the Potential Radiological Consequences of a Loss of Coolant Accident for Pressurized Water Reactors," June 1974.

12. Cottrell, W.B. and Savokainen, A.W., "U.S. Reactor Containment Technology," ORNL-NSIC-5, Vol. I, August 1965.

13. "Nuclear Safety Program Semiannual Progress Report for Period Ending June 30, 1963," ORNL-3483, September 1963.

14. "Nuclear Safety Program Semiannual Progress Report for Period Ending December 31, 1963," ORNL-3547, March 1964.

REFERENCES (Cont.)

15. "Reactor Safety Study," WASH-1400, App. VII, "Release of Radioactivity in Reactor Accidents," October 1975.

16. "Technical Bases for Estimating Fission Product Behavior During LWR Accidents," NUREG-0772, June 1981.

17. Cottrell, W.B. and Savokainen, A.W., "U.S. Reactor Containment Technology," ORNL-NSIC-5, Vol II, App. G, August 1965.

18. "Regulatory Impact of Nuclear Reactor Accident Source Term Assumptions," NUREG-0771, June 1981.

19. Warman, E.A., "Assessment of the Radiological Consequences of Postulated Reactor Accidents," Stone and Webster Engineering Corporation Paper, November 1982.

20. Thompson, T.J. and Beckerley, J.G. (eds.), The Technology of Nuclear Reactor Safety, Vol. 1, "Reactor Physics and Control," MIT Press, 1973.

21. Keller, R.F., "Fuel Element Flow Blockage in the Engineering Test Reactor," IDO-16780, May 1962.

22. Slade, D.H. (ed.), "Meteorology and Atomic Energy 1968," TID-24190, July 1968.

23. U.S. NRC Regulatory Guide 1.145, "Atmospheric Dispersion Models for Potential Accident Consequence Assessments at Nuclear Power Plants," August 1979.

24. MIT Physical Plant Blueprint #NW12 G01.05, "Nuclear Reactor Site Plan," November 1956.

25. U.S. Weather Bureau, "Meteorology and Atomic Energy," July 1955.

26. International Commission on Radiation Protection, "Report of Committee II on Permissible Dose for Internal Radiation (1959)," ICRP Publication 2, Pergamon Press, 1960.

27. Jaeger, R.G. (ed.), Engineering Compendium on Radiation Shielding, Vol. I, "Shielding Fundamentals and Methods," Springer-Verlag, 1968.

28. Blizzard, E.P. (ed.), Reactor Handbook, 2nd Ed., Vol. IIIB, "Shielding," Interscience Publishers, 1962.

29. Rockwell, T. (ed.), "Reactor Shielding Design Manual," TID-7004, 1956.

30. Wood, J., Computational Methods in Reactor Shielding, Pergamon Press, 1982.

REFERENCES (Cont.)

31. Stephenson, R., Introduction to Nuclear Engineering, 2nd Ed., McGraw-Hill, 1958.

32. Evans, R., The Atomic Nucleus, McGraw-Hill, 1955.

33 Borak, T.B., "A Simple Approach to Calculating Gamma Ray Skyshine for Reduced Shielding Applications," Health Physics, 29: 423-425, 1975.

34. Trubey, D.K., "The Single-Scattering Approximation to the Gamma Ray Air Scattering Problem," ORNL-2998, February 1961.

35. Lynch, R.E., et al., "A Monte Carlo Calculation of Air-Scattered Gamma Rays," ORNL-2282, Vol. I, October 1958.

36. Drawing #8 of the original reactor containment plans on file in the drafting room of the Reactor Operations Office, Building NW-12.

37. National Weather Service Forecast Office, General Logan International Airport, "Local Climatological Data - Monthly Summary," National Climatic Center, Ashville, N.C., January through December 1981.

38. Lederer, C.M., Hollander, J.M. and Perlman, I., Table of Isotopes, 6th Ed., John Wiley and Sons, 1967.

39. Lederer, C.M. and Shirley, V.S. (ed.), Table of Isotopes, 7th Ed., John Wiley and Sons, 1978.

40. Goldstein, H. and Wilkins, J.E. Jr., "Calculations of the Penetrations of Gamma Rays," NYO-3075, 1954.

41. Kruger, F.W., "Aufbaufaktoren für γ-Strahlung mit Niedrigen Quantenenergien, " (in German), Kernenergie, 10: 194-195, 1967.

42. Shure, K. and Wallace, O.J., "Taylor Coefficients for Eisenhauer-Simmons Gamma Ray Buildup Factors in Ordinary Concrete," Nucl Sci Eng, 62: 746-738, 1977.

43. Trubey, D.K., "A Survey of Empirical Functions Used to fit Gamma Ray Buildup Factors," ORNL-RSIC-10, February 1966.

APPENDIX A

DATA TABLES

TABLE A.1

Values of N_s^i/N_{25}° for Neutron-Capture Influenced Isotopes at $\phi_T = 4 \times 10^{13}$ [8]

Isotope	N_s^i/N_{25}°
Xe 135	1.05×10^{-5}
Cs 134	1.4×10^{-1}
Cs 136	3.6×10^{-4}
Cs 137	1.5×10^{0}
Rb 86	8.0×10^{-4}

TABLE A.2

Frequency of Wind Speed and Direction in Boston, Year 1981 [37]

Direction (Blowing from)	Windspeed (KPH)																										Total Frequency
	0	1	2	3	4	5	6	7	8	9	10	11	12	13	14	15	16	17	18	19	20	21	22	23	24	25+	
N			2	1	13	11	16	18	23	22	19	9	6	10	13	6	4	4	1		2				1		181
NNE			4	1	7	5	4	8	6	3	4	3	6	7	5	4	3		2		2					1	75
NE			2	2	6	7	6	11	3	8	9	7	4	10	5	4	3	3	1	2	1	1				1	96
ENE				3	5	1	8	7	16	9	12	10	8	7	9	3	2	1									101
E		1		1	3	12	14	17	21	12	20	9	9	11	6	5	1	3	1		3						149
ESE				3	4	4	12	15	13	12	22	13	15	6	13	6	7	1	3	1	1				1		152
SE			1	5	6	8	21	13	15	11	12	4	5	1	2	2		1									107
SSE			1		4	7	6	11	7	7	8	4	2		2		1					1					61
S			3	4	7	9	21	20	17	16	19	14	13	11	7	10	1	2	1	3	5			1		5	189
SSW			1	2		4	10	18	9	11	18	12	14	10	13	6	9	4	5	5		3	4	2		1	161
SW				1	3	3	9	16	20	24	29	18	17	13	19	6	5	7	5	1	2		1				199
WSW				3	3	3	14	17	25	18	23	19	16	14	13	12	6	8	4	2				1			201
W				2	7	14	16	25	32	27	29	43	35	37	43	25	13	9	10	3	13	4	4	2	1	2	396
WNW				2	7	9	10	33	26	27	35	38	39	32	28	25	19	14	11	9	7	4	2	4	1	2	384
NW				1	6	5	9	21	26	24	33	28	27	31	25	14	12	11	4	5	7	1	5	1	1		297
NNW				1	3	7	5	21	22	12	22	18	15	10	8	9	7	4	3		1						168
Calm	3																										3

TABLE A.3

Relative Frequency of Stability Conditions,
Blue Hills, MA, 1888-1889 [2]

Stability Condition	Pasquill Category	Relative Frequency
Unstable	A,B,C	30.5
Neutral	D	24.5
Stable	E	39.5
Stable	F	5.0
Stable	G	0.5

TABLE A.4

Leakage Dose Parameters by Isotope

Isotope	Total Release Q_T (Ci)	Average Beta Energy $\overline{E}_\beta$ (Mev/dis) [38,39]	Average Gamma Energy $\overline{E}_\gamma$ (Mev/dis) [38,39]	Gamma Conversion Factor C_γ Rads per Ci-sec/m^3 [7]	Thyroid Conversion Factor C_T Rads per Ci inhaled [7]
Kr 85m	1.39×10^{0}	2.7×10^{-1}	-	3.64×10^{-2}	2.0×10^{-1}
87	1.80×10^{0}	1.3×10^{0}	-	1.81×10^{-1}	9.7×10^{-1}
88	3.14×10^{0}	9.3×10^{-1}	-	4.67×10^{-1}	2.0×10^{0}
Xe 131m	3.24×10^{-2}	-	1.64×10^{-1}	-	-
133m	1.71×10^{-1}	-	2.33×10^{-1}	-	-
133	6.98×10^{0}	1.15×10^{-1}	-	9.06×10^{-3}	3.9×10^{-1}
135m	3.63×10^{-1}	-	5.27×10^{-1}	-	-
135	9.51×10^{-1}	3.1×10^{-1}	-	5.67×10^{-2}	9.1×10^{-1}
138	1.21×10^{-1}	8.0×10^{-1}	9.4×10^{-1}	-	-
I 131	9.33×10^{-2}	1.9×10^{-1}	-	8.72×10^{-2}	1.3×10^{5}
132	1.08×10^{-1}	7.07×10^{-1}	-	5.11×10^{-1}	6.6×10^{3}
133	2.04×10^{-1}	4.23×10^{-1}	-	1.54×10^{-1}	1.2×10^{5}
134	1.24×10^{-1}	8.10×10^{-1}	-	5.33×10^{-1}	1.1×10^{3}
135	1.73×10^{-1}	4.7×10^{-1}	-	4.19×10^{-1}	4.3×10^{4}

TABLE A.4 (Cont.)

Isotope	Total Release	Average Beta Energy	Average Gamma Energy	Gamma Conversion Factor	Thyroid Conversion Factor
Br 83	1.18×10^{-2}	3.1×10^{-1}	5.30×10^{-1}	-	-
84	1.21×10^{-2}	1.56×10^{0}	1.52×10^{0}	-	-
Cs 134	1.93×10^{-1}	2.21×10^{-1}	-	3.50×10^{-1}	5.8×10^{2}
136	2.79×10^{-2}	1.14×10^{-1}	-	4.78×10^{-1}	6.9×10^{2}
137	1.56×10^{-1}	1.71×10^{-1}	-	1.22×10^{-1}	3.6×10^{2}
Rb 86	4.13×10^{-2}	5.93×10^{-1}	-	2.07×10^{-2}	5.0×10^{2}
Te 127m	3.81×10^{-3}	2.43×10^{-1}	-	1.10×10^{-3}	1.6×10^{-1}
127	1.58×10^{-2}	2.33×10^{-1}	-	9.36×10^{-4}	2.9×10^{0}
129m	2.31×10^{-2}	5.33×10^{-1}	-	7.83×10^{-3}	4.3×10^{1}
129	4.04×10^{-2}	4.83×10^{-1}	-	1.47×10^{-2}	8.1×10^{-1}
131m	2.39×10^{-2}	3.0×10^{-1}	-	3.14×10^{-1}	4.5×10^{3}
131	5.66×10^{-2}	7.13×10^{-1}	3.4×10^{-1}	-	-
132	2.96×10^{-1}	7.3×10^{-2}	-	4.75×10^{-2}	4.8×10^{4}
133m	1.74×10^{-1}	8.0×10^{-1}	6.5×10^{-1}	-	-
Sr 91	5.34×10^{-3}	8.9×10^{-1}	-	1.69×10^{-1}	1.3×10^{2}
Ba 140	6.10×10^{-3}	3.4×10^{-1}	-	4.44×10^{-2}	2.2×10^{2}

TABLE A.4 (Cont.)

Isotope	Total Release	Average Beta Energy	Average Gamma Energy	Gamma Conversion Factor	Thyroid Conversion Factor
Ru 103	2.81×10^{-3}	7.0×10^{-2}	-	1.11×10^{-1}	5.2×10^{1}
105	7.53×10^{-4}	3.88×10^{-1}	-	1.79×10^{-1}	1.4×10^{1}
106	3.69×10^{-4}	1.3×10^{-2}	-	4.31×10^{-2}	4.8×10^{1}
Rh 105	8.58×10^{-4}	1.89×10^{-1}	-	1.82×10^{-2}	6.4×10^{0}
Tc 99m	5.20×10^{-4}	-	-	3.06×10^{-2}	4.6×10^{1}
Mo 99	5.87×10^{-3}	4.1×10^{-1}	-	3.64×10^{-2}	9.4×10^{1}
Sb 127	2.41×10^{-4}	5.0×10^{-1}	-	1.51×10^{-1}	1.0×10^{2}
129	8.35×10^{-4}	6.23×10^{-1}	-	2.68×10^{-1}	3.7×10^{1}
Nd 147	2.51×10^{-3}	2.7×10^{-1}	-	3.14×10^{-2}	1.2×10^{1}
La 140	6.01×10^{-3}	4.53×10^{-1}	-	5.67×10^{-1}	1.5×10^{2}
Ce 141	5.82×10^{-3}	1.94×10^{-1}	-	1.38×10^{-2}	6.0×10^{0}
143	5.90×10^{-3}	4.63×10^{-1}	-	6.81×10^{-2}	1.8×10^{1}
144	5.93×10^{-3}	1.03×10^{-1}	-	4.31×10^{-3}	5.1×10^{0}
Zr 95	6.22×10^{-3}	1.32×10^{-1}	-	1.62×10^{-1}	7.9×10^{1}
97	5.79×10^{-3}	6.37×10^{-1}	-	4.22×10^{-2}	7.7×10^{1}
Nb 95	6.22×10^{-3}	5.33×10^{-1}	-	1.66×10^{-1}	8.1×10^{1}

TABLE A.5

Gamma Emission Energies by Isotope

Isotope	Total Decay Emissions $Q^i_{c_T}$ (Dis)	Photon Energy (Mev) and Distribution (%) [38,39]
Kr 85m	2.22×10^{17}	0.15 (78), 0.3 (14)
87	2.87×10^{17}	0.4 (50), 0.8 (8), 3.0 (14)
88	5.03×10^{17}	0.03 (2), 0.15 (7), 0.2 (35), 0.4 (5), 0.8 (23), 1.5 (14), 2.0 (53)
Xe 131m	5.18×10^{15}	0.15 (2)
133m	2.73×10^{16}	0.2 (10)
133	1.12×10^{18}	0.08 (37)
135m	5.80×10^{16}	0.5 (81)
135	1.53×10^{17}	0.3 (91), 0.6 (3)
138	1.93×10^{17}	0.15 (10), 0.3 (30), 0.4 (12), 0.5 (3), 2.0 (37)
I 131	4.97×10^{16}	0.08 (3), 0.3 (5), 0.4 (82), 0.6 (7), 0.8 (2)
132	5.76×10^{16}	0.5 (20), 0.6 (99), 0.8 (85), 1.0 (22), 1.5 (8), 2.0 (2)
133	1.09×10^{17}	0.5 (86)
134	6.59×10^{16}	0.15 (3), 0.4 (8), 0.5 (8), 0.6 (18), 0.8 (160), 1.0 (11), 1.5 (9), 2.0 (5)
135	9.19×10^{16}	0.4 (6), 0.8 (8), 1.0 (38), 1.5 (46), 2.0 (10)
Br 83	6.31×10^{15}	0.5 (1.4)
84	6.43×10^{15}	0.6 (1), 0.8 (48), 1.0 (8), 2.0 (25), 4.0 (7)
Cs 134	3.43×10^{16}	0.5 (1), 0.6 (121), 0.8 (95), 1.0 (3), 1.5 (3)

TABLE A.5 (Cont.)

Isotope	Total Decay Emissions	Photon Energy and Distribution
Cs 136	4.95×10^{15}	0.06 (11), 0.08 (6), 0.15 (36), 0.3 (71), 0.8 (100), 1.0 (82), 1.5 (20)
137	2.77×10^{16}	0.6 (85)
Rb 86	7.32×10^{15}	1.0 (9)
Te 127m	6.76×10^{14}	0.06 (1)
127	6.14×10^{11}	0.4 (1)
129m	4.10×10^{15}	0.6 (3)
129	7.17×10^{15}	0.03 (17), 0.5 (7), 1.0 (1)
131m	4.25×10^{15}	0.08 (2), 0.10 (5), 0.2 (16), 0.3 (9), 0.8 (91), 1.0 (24), 1.5 (3), 2.0 (3)
131	1.01×10^{16}	0.15 (68), 0.5 (21), 0.6 (4), 1.0 (13)
132	5.26×10^{16}	0.05 (14), 0.2 (88)
133m	3.09×10^{16}	0.3 (11), 0.4 (1), 0.6 (23), 0.8 (8), 1.0 (89)
134	3.64×10^{16}	0.08 (21), 0.2 (48), 0.3 (21), 0.4 (19), 0.5 (35), 0.8 (45)
Sr 91	9.49×10^{14}	0.6 (15), 0.8 (27), 1.0 (33), 1.5 (5)
Ba 140	1.08×10^{15}	0.03 (11), 0.15 (6), 0.3 (6), 0.4 (5), 0.5 (34)
Ru 103	4.99×10^{14}	0.5 (88), 0.6 (6)
105	1.34×10^{14}	0.3 (17), 0.4 (6), 0.5 (20), 0.6 (16), 0.8 (48)
106	6.55×10^{13}	No Gamma Decay
Rh 105	1.52×10^{14}	0.3 (24)
Tc 99m	9.24×10^{13}	0.15 (90)
Mo 99	1.04×10^{15}	0.04 (2), 0.2 (7), 0.4 (1), 0.8 (16)

TABLE A.5 (Cont.)

Isotope	Total Decay Emissions	Photon Energy and Distribution
Sb 127	4.28×10^{13}	0.06 (1), 0.3 (3), 0.4 (9), 0.5 (29) 0.6 (45), 0.8 (17)
129	1.48×10^{14}	0.4 (5), 0.5 (21), 0.6 (12), 0.8 (58), 1.0 (46)
Nd 147	4.46×10^{14}	0.10 (28), 0.3 (3), 0.4 (4), 0.5 (13)
La 140	1.07×10^{15}	0.3 (20), 0.5 (40), 0.8 (19), 1.0 (10), 1.5 (96), 3.0 (3)
Ce 141	1.03×10^{15}	0.15 (48)
143	1.05×10^{15}	0.06 (11), 0.3 (46), 0.5 (3), 0.6 (7), 0.8 (10), 1.0 (1)
144	1.05×10^{15}	0.08 (2), 0.15 (11)
Zr 95	1.11×10^{15}	0.8 (98)
97	1.03×10^{15}	0.6 (92)
Nb 95	1.11×10^{15}	0.6 (100)

TABLE A.6

Attenuation and Absorption Coefficients [27,28]

Gamma Energy E (Mev)	Linear Attenuation Coefficients: Concrete μ_c (cm^{-1})	Linear Attenuation Coefficients: Steel μ_{ST} (cm^{-1})	True Energy Absorption Coefficient in Air μ_a (cm^2/g)	E'_{min} (Mev)	Maximum Absorption Coefficient $\bar{\mu}_a$ (cm^2/g)
0.03	2.63	59.9	0.148	0.027	0.148
0.04	1.31	26.3	0.0668	0.035	0.0668
0.05	0.848	14.0	0.0406	0.042	0.0668
0.06	0.642	8.60	0.0305	0.049	0.0406
0.08	0.470	4.19	0.0243	0.061	0.0305
0.10	0.402	2.61	0.0234	0.072	0.0243
0.15	0.329	1.41	0.0250	0.095	0.0250
0.20	0.294	1.07	0.0268	0.112	0.0268
0.30	0.251	0.821	0.0287	0.138	0.0287
0.40	0.225	0.707	0.0295	0.156	0.0295
0.50	0.205	0.636	0.0297	0.169	0.0297
0.60	0.190	0.584	0.0296	0.179	0.0297
0.80	0.166	0.510	0.0289	0.194	0.0297
1.0	0.150	0.460	0.0280	0.204	0.0297
1.5	0.123	0.373	0.0256	0.218	0.0297
2.0	0.105	0.326	0.0237	0.227	0.0297
3.0	0.0858	0.276	0.0211	0.235	0.0297
4.0	0.0750	0.254	0.0195	0.240	0.0297

TABLE A.7

Shield Thicknesses in Mean Free Paths

Gamma Energy E (Mev)	μT (b)		
	Concrete	Steel (b_1)	Total (b_2)
0.03	160.4	56.9	217.3
0.04	79.9	25.0	104.9
0.05	51.7	13.3	65.0
0.06	39.2	8.17	47.4
0.08	28.7	3.98	32.7
0.10	24.5	2.48	27.0
0.15	20.1	1.34	21.4
0.20	17.9	1.02	18.9
0.30	15.3	0.780	16.1
0.40	13.7	0.672	14.4
0.50	12.5	0.604	13.1
0.60	11.6	0.555	12.2
0.80	10.1	0.485	10.6
1.0	9.15	0.437	9.57
1.5	7.50	0.354	7.85
2.0	6.41	0.310	6.72
3.0	5.23	0.262	5.49
4.0	4.58	0.241	4.82

TABLE A.8

Point Isotropic Source Exposure Build-up Factors for Iron (Steel) [40,41]

E (Mev)	b (μT) 1	2	3
0.10	1.5	2.2	3.1
0.15	1.75	2.65	4.2
0.20	2.0	3.1	5.3
0.30	2.05	3.15	5.8
0.40	2.1	3.3	6.0
0.50	1.98	3.09	5.98
0.60	1.96	3.02	5.90
0.80	1.91	2.95	5.62
1.0	1.87	2.89	5.39
1.5	1.82	2.66	4.76
2.0	1.76	2.43	4.13
3.0	1.55	2.15	3.51
4.0	1.45	1.94	3.03

TABLE A.9

Coefficients of the Taylor Exposure Build-up Factor Formula

E	Concrete [42]			Steel [43]		
(Mev)	A	α_1	α_2	A	α_1	α_2
0.10	139.5813	-0.04127	-0.02927			
0.15	97.7220	-0.08301	-0.06400			
0.20	87.8408	-0.10004	-0.07912		Not Available	
0.30	80.5000	-0.10500	-0.08400			
0.40	46.6038	-0.10489	-0.07132			
0.50	67.3716	-0.09198	-0.07061	31.379	-0.06842	-0.03742
0.60	70.0000	-0.08400	-0.06500	30.095	-0.06694	-0.03486
0.80	65.7882	-0.07061	-0.05247	27.526	-0.06390	-0.02975
1.0	77.7911	-0.05818	-0.04420	24.957	-0.06086	-0.02463
1.5	15.1893	-0.06012	0.00252	21.290	-0.05357	-0.01495
2.0	17.1222	-0.04488	0.00448	17.622	-0.04627	-0.00526
3.0	13.7579	-0.02849	0.02761	13.218	-0.04431	-0.00087
4.0	14.2241	-0.02223	0.02316	9.624	-0.04698	0.00175

TABLE A.10

Values of the Functions $G(1,p,0,b_2')$ and $G(1,p,0,b_2'')$ [27]

E (Mev)	b_2'	b_2''	p = 1.75		p = 2.90	
			$G(b_2')$	$G(b_2'')$	$G(b_2')$	$G(b_2'')$
0.10	25.9	26.2	5.4×10^{-13}	3.85×10^{-13}	4.5×10^{-13}	3.6×10^{-13}
0.15	19.6	20.0	3.9×10^{-10}	2.62×10^{-10}	3.05×10^{-10}	2.07×10^{-10}
0.20	17.0	17.4	6.0×10^{-9}	3.9×10^{-9}	4.6×10^{-9}	3.0×10^{-9}
0.30	14.4	14.7	9.4×10^{-8}	6.8×10^{-8}	6.9×10^{-8}	5.0×10^{-8}
0.40	12.9	13.4	4.4×10^{-7}	2.6×10^{-7}	3.2×10^{-7}	1.9×10^{-7}
0.50	11.9	12.2	1.25×10^{-6}	9.2×10^{-6}	8.8×10^{-6}	6.4×10^{-6}
0.60	11.2	11.4	2.7×10^{-6}	2.2×10^{-6}	1.8×10^{-6}	1.5×10^{-6}
0.80	9.85	10.0	1.15×10^{-5}	9.84×10^{-6}	7.4×10^{-6}	6.23×10^{-6}
1.0	9.03	9.17	2.8×10^{-5}	2.4×10^{-5}	1.7×10^{-5}	1.55×10^{-5}
1.5	7.38	7.87	1.7×10^{-4}	9.6×10^{-5}	9.2×10^{-5}	5.6×10^{-5}
2.0	6.42	6.75	4.5×10^{-4}	3.2×10^{-4}	2.45×10^{-4}	1.8×10^{-4}
3.0	5.33	5.64	1.55×10^{-3}	1.05×10^{-3}	7.8×10^{-4}	5.6×10^{-4}
4.0	4.74	4.93	2.95×10^{-3}	2.45×10^{-3}	1.45×10^{-3}	1.15×10^{-3}

TABLE A.11

Air Scattering Input Parameters

Source Point	ψ_o (Radians)	ϕ_o (Radians)	φ (Radians)	x (cm)	h' (m)	R' (m)
8m:						
Upper	0.349	0.314	-	2.27×10^3	-	-
Point 1	0.544	0.486	0.395	2.08×10^3	1.60	10.8
Point 2	0.668	0.636	0.245	1.98×10^3	4.80	11.7
Point 3	0.730	0.794	0.086	1.93×10^3	8.00	13.3
21m:						
Upper	0.138	0.070	-	3.43×10^3	-	-
Point 1	0.399	0.184	0.250	3.30×10^3	1.60	10.8
Point 2	0.572	0.285	0.149	3.24×10^3	4.80	11.7
Point 3	0.694	0.384	0.050	3.20×10^3	8.00	13.3

TABLE A.12

Steel Scattering Input Parameters

Source Point	ψ_1 (Radians)	ψ_2 (Radians)	ϕ_1 (Radians)	ϕ_2 (Radians)	r_1 (cm)	r_2 (cm)
8m:						
Upper	0.349	0.679	0.314	0.390	1.13×10^3	1.61×10^3
Point 1	0.544	0.950	0.486	0.563	1.19×10^3	1.70×10^3
Point 2	0.668	1.035	0.636	0.713	1.34×10^3	1.71×10^3
Point 3	0.730	1.066	0.794	0.872	1.51×10^3	1.74×10^3
21m:						
Upper	0.138	1.941	0.070	0.132	7.00×10^2	3.60×10^3
Point 1	0.399	1.821	0.184	0.248	9.70×10^2	3.60×10^3
Point 2	0.572	1.720	0.285	0.349	1.23×10^3	3.60×10^3
Point 3	0.694	1.621	0.384	0.448	1.46×10^3	3.60×10^3

APPENDIX B

CONTAINMENT DIMENSIONS AND PARAMETERS

A cross-sectional view of the containment with its dimensions is shown in Fig. B.1. The effect of smaller equipment located within the containment on the volume and surface area will be neglected. Only the reactor vessel and its shielding are taken into account.

B.1 Containment Volume

For convienience the containment can be considered as the three sections shown in Fig. B.2. Only the volume above grade is considered. This is conservative as it results in a higher fission product concentration and increased source strength. During an actual release some fission products will travel into the basement.

For the dome, the volume is

$$V = \frac{1}{6} \pi h_4 (3r_1^2 + h_4^2)$$

For the center slice,

$$V = \pi r_1^2 h_3$$

and for the lower section,

$$V = \pi r_2^2 h_2 - \pi r_3^2 h_1$$

Substituting values from Fig. B.1, the total volume is

$$V = 1.67 \times 10^5 \text{ ft}^3 \ (\ 4.73 \times 10^3 \text{ m}^3 \ )$$

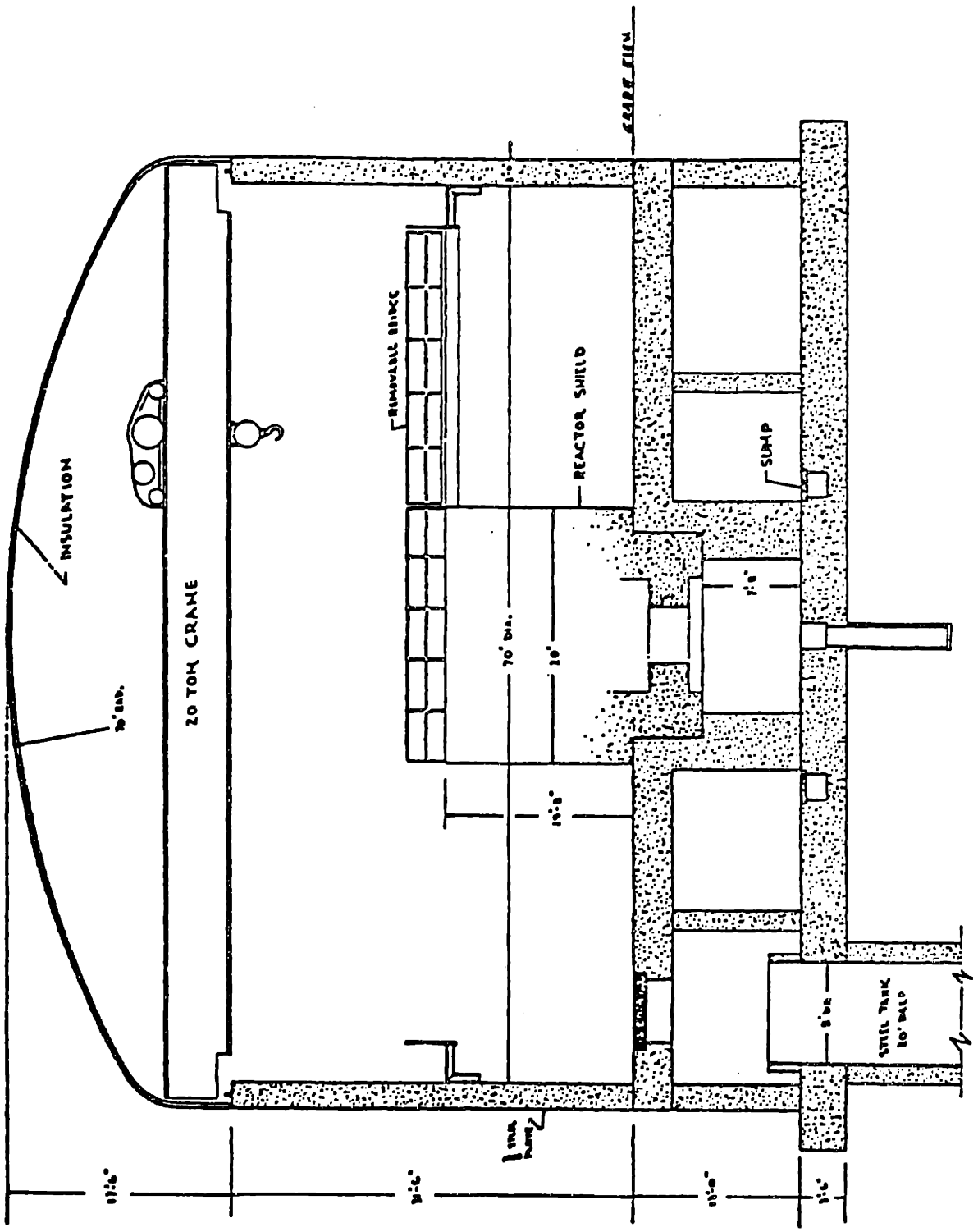

Figure B.1 Cross Section of Reactor Building [1]

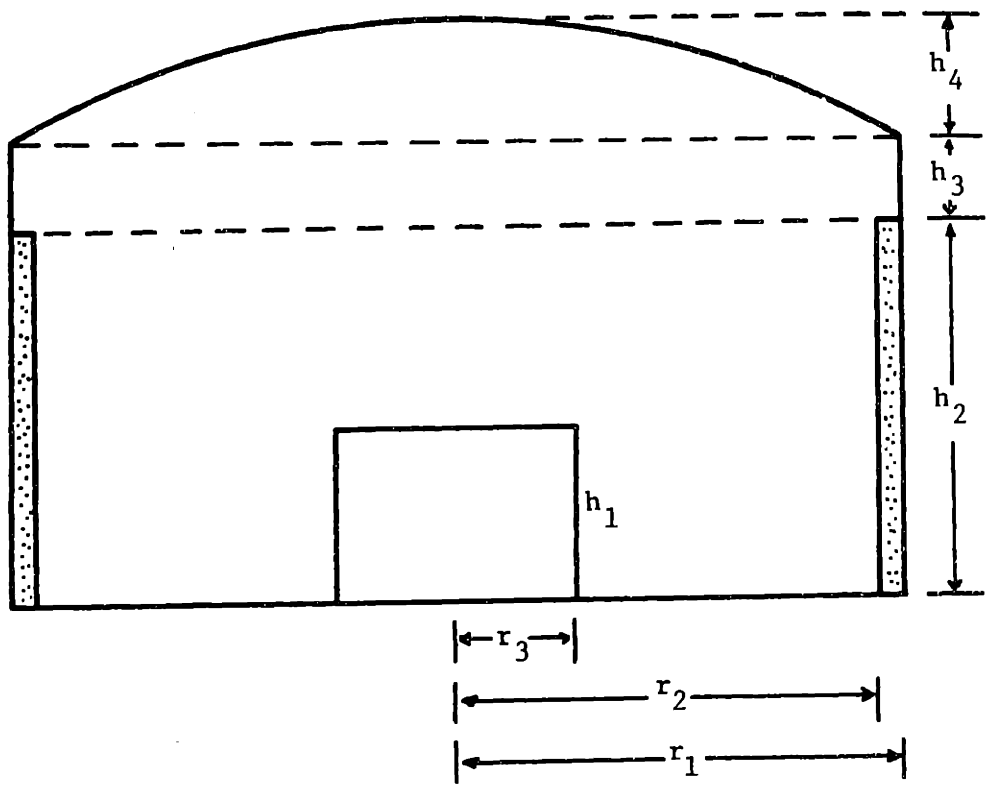

Figure B.2

Parameters for Containment Derivations

B.2 Containment Surface Area

For the dome the area is

$$A = 2 \pi h_4 L$$

where L = Radius of dome curvature = 70 ft.

The area of the sides is equal to

$$A = 2 \pi r_1 (h_2 + h_3)$$

The area due to the floor, reactor and shadow shield top is

$$A = \pi r_1^2 + 2 \pi r_3 h_1$$

with the resulting total inner surface area of

$$A_s = 1.91 \times 10^4 \text{ ft}^2 \quad (1.78 \times 10^3 \text{ m}^3)$$

B.3 Containment Cross-Sectional Area

For the dome the cross-sectional area is

$$A = R^2 \cos^{-1}\left(\frac{R - h_4}{R}\right) - (R - h_4) (2 R h_4 - h_4^2)^{1/2}$$

For the sides the area is simply

$$A = 2 r_1 (h_2 + h_3)$$

The total sross-sectional area is then

$$A_{xs} = 3.38 \times 10^3 \text{ ft}^3 \quad (3.14 \times 10^2 \text{ m}^2)$$

APPENDIX C

DERIVATION OF THE DISK-SOURCE FLUX EQUATION (Eq. 4.9) [27,29]

For a point source of strength S photons/sec shielded by a slab b mean free paths thick the flux reaching point P (see Fig. C.1) at a distance of x cm is:

$$\phi_\gamma = \frac{B\ S}{4\pi x^2}\ e^{-b} \qquad \text{photons/cm}^2\text{-sec}$$

where B = Point isotropic build-up factor
(a function of shield material, b and E)

Therefore for a disk of source strength S_A photons/cm^2-sec the flux at P from the differential ring between r and r + dr is:

$$d\phi_\gamma = \frac{B\ S_A\ (2\pi r dr)}{4\pi \rho^2}\ e^{-b\sec\theta''}$$

But $\rho^2 = r^2 + x^2$

therefore $\rho d\rho = r dr$

Also $\sec\theta'' = \frac{\rho}{x}$

therefore

$$d\phi_\gamma = \frac{BS_A}{2}\ \frac{d\rho}{\rho}\ e^{-b\ \frac{\rho}{x}}$$

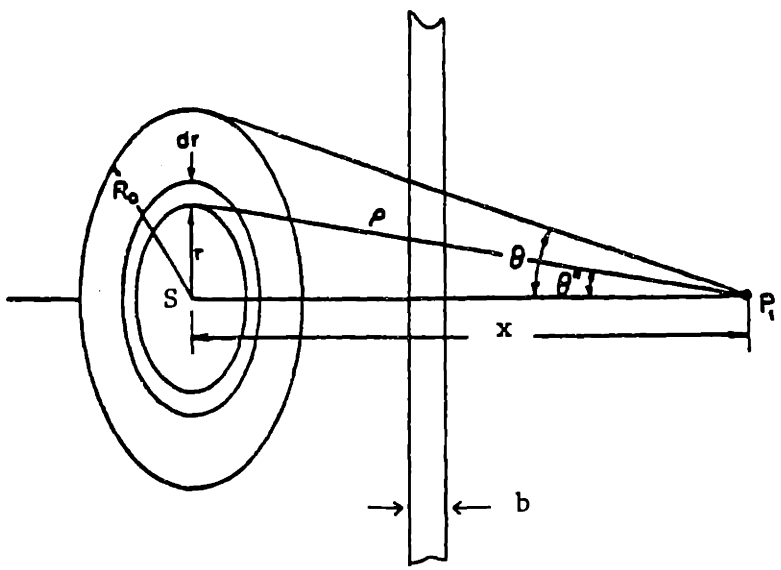

Figure C.1

Geometry for Disk Source Flux Derivation [31]

Substituting $\frac{b\rho}{x} \equiv t$ and integrating over the disk,

$$\phi_\gamma = \frac{BS_A}{2} \int_b^{b\sec\theta} \frac{e^{-t}}{t}\, dt$$

Since, by definition,

$$E_1(x) \equiv \int_x^\infty \frac{e^{-t}}{t}\, dt$$

the flux can be expressed as

$$\phi_\gamma = \frac{BS_A}{2} [E_1(b) - E_1(b\sec\theta)] \quad \text{photons/cm}^2\text{-sec}$$

APPENDIX D

DERIVATION OF THE CYLINDRICAL VOLUME SOURCE FLUX EQUATION (Eq. 4.19) [27]

For the self-absorbing cylindrical volume source shown in Fig. D.1 the uncollided flux at point P is:

$$\phi_\gamma = \frac{BS_v}{4\pi} \int_V \frac{e^{-\mu_s x} e^{-\mu y}}{r^2} dV$$

where x = Distance from dV to the cylinder surface (the self-absorption distance)

y = Attenuation path length in the shield

r = Distance from dV to P

μ_s = Linear attenuation coefficient in the source

μ = Linear attenuation coefficient in the shield

For the cylindrical coordinate system z, ρ, φ

$$dV = dz d\rho d\varphi$$

and

$$\phi_\gamma = \frac{BS_v}{2\pi} \int_0^h dz \int_0^R \rho d\rho \int_0^\pi \frac{e^{-\mu_s x} e^{-\mu y} d\varphi}{\rho^2 + s^2 + z^2 - 2s\rho\cos\varphi}$$

It can be seen from Fig. D.1 that

$$x = (PB - PC) \sec\psi$$

where

$$\sec\psi = \frac{PD}{PB} = \frac{(z^2 + \rho^2 + s^2 - 2s\rho\cos\varphi)^{1/2}}{(\rho^2 + s^2 - 2s\rho\cos\varphi)^{1/2}}$$

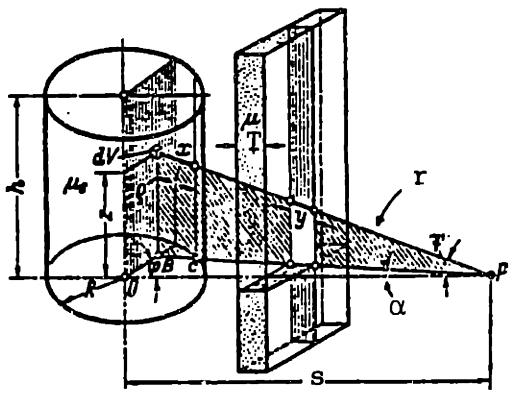

Geometry for self-absorbing cylindrical volume source with slab shield at side.

Figure D.1 [27]

From the triangle POC ,

$$PC = s\cos\alpha - (\rho^2 + s^2 - 2s\rho\cos\varphi)^{1/2}$$

Also,

$$\cos\alpha = \frac{s - \rho\cos\varphi}{(s^2 + \rho^2 - 2s\rho\cos\varphi)^{1/2}}$$

Substituting, x becomes

$$x = \frac{\rho^2 - s\rho\cos\varphi + [(\rho^2 + s^2 - 2s\rho\cos\varphi)R^2 - s^2\rho^2\sin^2\varphi]^{1/2}}{\rho^2 + s^2 - 2s\rho\cos\varphi} \cdot$$

$$\cdot (z^2 + \rho^2 + s^2 - 2s\rho\cos\varphi)^{1/2}$$

In addition,

$$y = t\sec\alpha\sec\psi$$

or

$$y = \frac{t(z^2 + \rho^2 + s^2 - 2s\rho\cos\varphi)^{1/2}}{s - \rho\cos\varphi}$$

Introducing the dimensionless variables

$$m = \frac{\rho}{R} \quad , \quad n = \frac{z}{R} \quad , \quad k = \frac{h}{R} \quad , \quad p = \frac{s}{R} \geq 1.25$$

the flux is

$$\phi_\gamma = \frac{BS_v R}{2\pi} G (k,p,\mu_s R,b_2)$$

where $b_2 = \mu T$

and

$$G\left(k,p,\mu_s R,b_2\right) = \int_0^k dn \int_0^1 m\,dm \int_0^{\pi} \frac{b_2}{n^2+m^2+p^2-2mp\cos\varphi} \cdot$$

$$\cdot \exp\left\{ -\left(n^2+m^2+p^2-2mp\cos\varphi\right)^{1/2} \cdot \right.$$

$$\cdot \left[\mu_s R \, \frac{m^2 - mp\cos\varphi + \left(m^2+p^2-2mp\cos\varphi - m^2p^2\sin^2\varphi\right)^{1/2}}{m^2+p^2-2mp\cos\varphi} + \right.$$

$$\left. \left. + \frac{b_2}{p - m\cos\varphi} \right] \right\}$$

The function $G\left(k,p,\mu_s R,b_2\right)$ has been numerically evaluated and listed for selected values of k, p, $\mu_s R$, and b_2 in [27]. Note that for no self-absorption $\mu_s R = 0$. The values of the G function listed in Table A.10 were obtained by graphing the function as listed in [27] and interpolating to the required values of b_2' and b_2''.